



저작자표시-비영리-변경금지 2.0 대한민국

이용자는 아래의 조건을 따르는 경우에 한하여 자유롭게

- 이 저작물을 복제, 배포, 전송, 전시, 공연 및 방송할 수 있습니다.

다음과 같은 조건을 따라야 합니다:



저작자표시. 귀하는 원저작자를 표시하여야 합니다.



비영리. 귀하는 이 저작물을 영리 목적으로 이용할 수 없습니다.



변경금지. 귀하는 이 저작물을 개작, 변형 또는 가공할 수 없습니다.

- 귀하는, 이 저작물의 재이용이나 배포의 경우, 이 저작물에 적용된 이용허락조건을 명확하게 나타내어야 합니다.
- 저작권자로부터 별도의 허가를 받으면 이러한 조건들은 적용되지 않습니다.

저작권법에 따른 이용자의 권리는 위의 내용에 의하여 영향을 받지 않습니다.

이것은 [이용허락규약\(Legal Code\)](#)을 이해하기 쉽게 요약한 것입니다.

[Disclaimer](#)

공학박사학위논문

근접장 광학 기법을 통한  
CVD 그래핀의 굴절률 분석

Refractive Index Characterization of CVD  
Graphene Using Near-Field Optical Techniques

2015년 8월

서울대학교 대학원

기계항공공학부

천 소 산



# **Refractive Index Characterization of CVD Graphene Using Near-Field Optical Techniques**

Sosan Cheon

WCU Multiscale Mechanical Design

School of Mechanical and Aerospace Engineering

Seoul National University

## **Abstract**

Graphene, the single atomic layer of carbons, presents unprecedented physical properties not only in terms of its electronic structure and optical transparency, but also of its high thermal conductivity and mechanical strength. For both the fundamental research and the practical applications of this unique material with sub-nm to few-nm thickness, the simple, reliable, and robust characterization tools are required. In this thesis, new optical characterization methods for imaging, layer counting, and refractive index (RI) measurements of graphene are developed. To achieve these, multiple near-field optical phenomena and techniques such as surface plasmon resonance (SPR), attenuated total internal reflection (ATR), and spectroscopic ellipsometry (SE) are used, all of which don't involve the scanning probe tips.

To reliably count the CVD graphene layers, the SPR reflectance from the graphene layer on a 48-nm thick gold layer is observed. Being one of the most sensitive RI

detection methods, it turns out that the SPR reflectance can reliably discriminate the 1-, 3-, and 5-layer CVD graphene layers. Not only the reflectance curve shapes of the SPR,  $R(\theta)$ , but the measured SPR angles, i.e. the incident angles for the minimum reflection, match the calculation results from the Fresnel's equations. Although graphene is atomically thin, accurate and reliable detection of the graphene layer number is possible due to the near-field sensitivity of SPR measurement scheme specifically designed for the graphene layer counting. This is in contrast to the recent studies for the identification and counting of the graphene layers based on Raman spectroscopy, atomic force microscopy (AFM), or reflection spectroscopy, all having limitations in accuracy, reliability, and capability of the graphene layer counting. These limitations are prominent when counting chemical vapor deposition (CVD) graphene, because of their large area, irregular profile, randomly oriented grains, and residues from transfer processes.

The new method to measure the complex RI of graphene is developed by the tandem use of the SPR and the ATR reflectance. Unlike previous works on the graphene RI measurements, this novel method tackles the problem fundamentally by using the concept of “2 results from 2 observables”, not “2 results from 1 observable with fitting”. Furthermore, the two observables are from the near-field interaction of the graphene and light for the enhanced RI sensitivity, as shown quantitatively by the theoretical analyses on the sensitivity and uncertainty. The measured 1-, 3-, and 5-layer graphene RI values at 634 nm wavelength lie in the middle of the previously reported data while the variations are within  $\pm 3\%$ , and match well with the density functional theory (DFT) calculation result by current work. The accurate measurements of optical properties of graphene are necessary in various research and application fields such as the thermal conductivity measurements of graphene by opto-thermal Raman spectroscopy, prediction of the absorption and reflection from the transparent graphene electrodes and color shifts in

flexible displays, to name a few.

Finally, the complex RI measurements for the N-doped graphene layers are conducted by spectroscopic ellipsometry. Because the DFT calculation predicts that the N-doping on graphene will result in the significant change of RI at specific wavelengths, measurements at several wavelengths or ultimately, spectroscopic measurements are desirable for the comparison with the pristine graphene's RI. Unfortunately, the tandem use of SPR and ATR is optimized for single-wavelength measurements, so the spectroscopic ellipsometry is used for the multi-wavelength measurements. The results show that the N-doping can lower both the real and imaginary parts of graphene's RI, which is due to the increased defect level and consequently the lowered carrier mobility. Further research with refined synthesis, transfer, and measurements methods will be able to unveil the inherent effects by nitrogen doping on graphene in the future.

**Keywords:** Graphene, layer counting, complex refractive index (RI), near-field optics, surface plasmon resonance (SPR), attenuated total internal reflection (ATR)

**Student Number:** 2009-20727

<b>Abstract</b>	i
<b>Contents</b>	iv
<b>List of Tables</b>	vii
<b>List of Figures</b>	viii
<b>Nomenclature</b>	xi

## **Chapter 1. Introduction**

1.1 Background	1
1.2 Previous studies on optical characterization of graphene	3
1.3 Objectives of present study	4

## **Chapter 2. Near-field optics for sub-nm-thin materials**

2.1 Refractive index (RI) of a sub-nm layer	11
2.1.1 Graphene modeled as a surface current without thickness	11
2.1.2 Effects of birefringence of a sub-nm layer	13
2.2 Surface plasmon resonance (SPR)	14
2.2.1 Principles of SPR	14
2.2.2 SPR microscopy (SPRM)	16
2.2.3 SPRM images of graphene layers	17
2.3 Attenuated total internal reflection (ATR)	19
2.3.1 Principles of ATR	19

2.3.2 ATR images of graphene layers	20
-------------------------------------	----

## **Chapter 3. Graphene layer counting by SPR**

3.1 Previous methods for graphene layer counting	31
3.1.1 Raman spectroscopy	31
3.1.2 Atomic force microscopy	31
3.1.3 Reflection or transmission contrast	32
3.2 Theoretical analyses for graphene on SPRM	32
3.2.1 Reflectance calculations for multi-layer systems	32
3.2.2 Configuration to enhance the SPRM sensitivity	33
3.3 Experimental results	34
3.3.1 SPRM images of 1, 3, and 5-layer graphene	35
3.3.2 SPR curves and SPR angles	35
3.3.3 Data analysis and discussions	36

## **Chapter 4. Complex RI of pristine CVD graphene**

4.1 Previous methods for graphene's RI measurements	44
4.1.1 Non-spectroscopic methods	44
4.1.2 Spectroscopic methods	45
4.2 Tandem use of SPR and ATR for complex RI measurements	45
4.2.1 Fundamental limitations of using a single measurement technique	45
4.2.2 New method: simultaneously using both SPR and ATR	46

4.3 Results and analyses	47
4.3.1 3-D contour plots of two observables vs. complex RI of graphene	47
4.3.2 ATR reflectance of a single layer graphene	48
4.3.3 Results, data analysis and discussions	49

## **Chapter 5. Complex RI of N-doped CVD graphene**

5.1 Background of N-doped graphene (NdG) study	68
5.1.1 Synthesis and transfer of NdG	68
5.1.2 Density functional theory (DFT) for complex RI of NdG	69
5.1.3 Limitations of SPR for RI measurements of NdG	70
5.2 Spectroscopic ellipsometry (SE) for accurate NdG measurements	71
5.2.1 Choice of a substrate	72
5.2.2 Method to extract complex RI from raw SE data	73
5.3 Results and analyses	74
5.3.1 Optical properties of NdG and pristine graphene: DFT study	74
5.3.2 Preliminary experiments with pristine CVD graphene	74
5.3.3 Data analysis and discussions	75

## **Chapter 6. Summary and Conclusion**

## List of Tables

Table 3.1 (Also in S. Cheon et al., 2012) Measured SPR angles of graphene samples and calculated values with three different dielectric constants from M. Klintenberg et al., 2009, X. Wang et al, 2008, and Z. H. Ni et al., 2009.

Table 4.1 (Also in S. Cheon et al., 2014) Measured and calculated complex RI values of various graphene and graphite samples reported in previous articles. Note that the superscript numbers in the “Reference” column coincide with those in Figure 4.6.

## List of Figures

Figure 1.1 The number of appearance of the word “graphene” in the scholar google search (<http://scholar.google.com>), which includes scientific journals, proceedings, books, and patents.

Figure 1.2 (From L. Zhao et al., 2011) STM imaging of nitrogen dopants and doping in NdG.

Figure 1.3 (From A. C. Ferrari, 2006) (a) Comparison of Raman spectra at 514 nm for bulk graphite and graphene of different layer numbers.

Figure 1.4 (From P. E. Gaskell et al., 2009) Left: Measured contrast ratios for 41 unique graphitic flakes.

Figure 2.1 Attenuated internal reflection calculation results (Finite thickness vs. no thickness with surface current) for the graphene on a BK7 prism where the light is coming from the lower side of the prism.

Figure 2.2 Attenuated internal reflection calculation results (Isotropic vs. anisotropic graphene) for the graphene on a BK7 prism where the light is coming from the lower side of the prism.

Figure 2.3 (Also in K. D. Kihm et al., 2012) Kretschmann’s configuration of a three-layered SPR system consisting of (1) prism, (2) metal film, and (3) medium.

Figure 2.4 The SPRM for graphene characterizations.

Figure 2.5 The evaporation of a water droplet imaged by the SPRM system developed in current work, which is shown in Figure 2.4-b.

Figure 2.6 The SPRM images of 3-layer graphene and the reflectance vs. incident angle data.

Figure 2.7 Calculation results of the ATR from the 1, 2, and 3-layer graphene for p-polarized (a) and s-polarized (b) light.

Figure 2.8 ATR images of  $2L$  graphene for (a) p-polarized and (s) polarized light.

Figure 3.1 Calculation results for the SPR reflectance from graphene layers on SPRM for air (a) and water (b) on top of graphene.

Figure 3.2 Graphene samples prepared on the SPRM substrates, i.e. 48-nm Au-coated slide glass.

Figure 3.3 Raman spectra of 1, 3, and 5-layer graphene layers on gold film.

Figure 3.4 SPRM images of graphene samples.

Figure 3.5 (Also in S. Cheon et al., 2012) Measured and calculated (equations (2.3), (2.4) and (2.5)) SPR reflectance variations with the incident angle for 1L, 3L, and 5L graphene on a 48 nm gold film.

Figure 4.1 (Also in S. Cheon et al., 2014) Experimental layout, a graphene sample's photo, and two relevant observables for the complex RI measurements of graphene.

Figure 4.2 (Also in S. Cheon et al., 2014) Method for the determination of the complex RI of graphene by the two observables.

Figure 4.3 Graphical presentation of the new graphene RI measurement method by the 3-D contour plots. The concept is exactly the same as that of Figure 4.2.

Figure 4.4 (Also in S. Cheon et al., 2014) The measured ATR  $R_p/R_s$  as changing the incident angle with the fitting curves calculated with three different RI values of graphene.

Figure 4.5 (Also in S. Cheon et al., 2014) Uncertainties associated with the single constraint of  $\theta_{\text{SPR}}$  data.

Figure 4.6 (Also in S. Cheon et al., 2014) Measured and predicted  $\text{RI}_G$  in comparison with other published results.

Figure 4.7 (Also in S. Cheon et al., 2014) Measurement sensitivity of  $\theta_{\text{SPR}}$  vs. the uncertainties of  $(n_G, k_G)$ .

Figure 4.8 (Also in S. Cheon et al., 2014) Orthogonality of the two independent observables,  $\theta_{\text{SPR}}$  and  $R_p/R_s^*$ .

Figure 4.9 Dependencies of the SPR reflectance curves onto different systematic uncertainties, wavelength dispersion of 40 nm, polarizer's offset of 3 °, and the Gaussian distribution of the incident angle, calculated based on the formula in Section 3.2.1.

Figure 4.10 (Also in S. Cheon et al., 2014) Ab-initio calculation results for the complex dielectric function of graphene.

Figure 5.1 (P. Nath et al., 2014) Calculated reflectivity functions of pristine and doped graphene layers.

Figure 5.2 (P. Nath et al., 2014) Calculated EELS functions of pristine graphene for both the pristine graphene and the NdG.

Figure 5.3 (P. Rani et al., 2014) The imaginary part of dielectric function for pure graphene as compared with graphene sheet doped with different concentrations of nitrogen, 3.125%, 6.25%, 9.375% and 18.75%.

Figure 5.4 Calculated SPR reflectance curves for three different incident wavelengths, with the quartz prism and the water medium.

Figure 5.5 SPR angles ( $\theta_{\text{SPR}}$ ) calculated as functions of the ( $n_G, k_G$ ) of the 3L graphene layers for the 48 nm Au film on 2 nm Ti layer for the adhesion to the quartz substrate, and the medium is water.

Figure 5.6 Orthogonality between the two observables,  $\theta_{\text{SPR}}$  and  $R_p/R_s^*$  by using the method in Section 4.3.3, for wavelengths of 650 nm and 450 nm, for the 48 nm Au film.

Figure 5.7 SPR angles ( $\theta_{\text{SPR}}$ ) calculated as functions of the ( $n_G, k_G$ ) of the 3L graphene layers for the 20 nm Au film on 2 nm Ti layer for the adhesion to the quartz substrate, and the medium is water.

Figure 5.8 Orthogonality between the two observables,  $\theta_{\text{SPR}}$  and  $R_p/R_s^*$  by using the method in Section 4.3.3, for wavelengths of 650 nm and 450 nm, for the 20 nm Au film.

Figure 5.9 RI of pristine graphene on a PDMS substrate measured by spectroscopic ellipsometry in present work and previous articles.

Figure 5.10 SE data fitting from a silicon substrate.

Figure 5.11 DFT calculation results for pristine and graphitic N-doped graphene for two atomic concentrations.

Figure 5.12 The 6 RI functions of pristine graphene by SE (curves) having the same data fitting errors.

Figure 5.13 XPS data (black) from pristine graphene sample.

Figure 5.14 (a) C peaks from the XPS data and (b) N 1s peak from N-doped graphene sample.

Figure 5.15 SE data fitting results for the N-doped graphene sample.

# Nomenclature

## Roman symbols

$2D$	Raman shift peak of graphene at $\sim 2580 \text{ cm}^{-1}$
$d$	Thickness of a layer
$G$	Raman shift peak of graphene at $\sim 1590 \text{ cm}^{-1}$
$I$	Electric current
$i$	Imaginary unit, $i^2 = -1$
$k$	Imaginary part of the refractive index or the wavenumber of the light
$L$	Number of atomic layers
$n$	Real part of the refractive index
$R$	Reflectance
$r$	Fresnel's reflection coefficient at an interface
$V$	Electric voltage
$Z_0$	Free-space impedance

## Greek symbols

$\alpha$	Fine structure constant or the angle between the two measurement observables
$\varepsilon$	Dielectric constant or dielectric function
$\theta$	Incident angle of the light, in the glass substrate (or prism)
$\lambda$	Wavelength
$\sigma_0$	Universal optical conductivity of graphene in R. R. Nair. Et al., 2008

## Subscripts

ATR	Attenuated total internal reflection
$G$	Graphene, pristine or NdG according to the context
$g$	Graphene, in P. E. Gaskell et al., 2009
NdG	N-doped graphene
$p$	p-polarized incidence
$s$	s-polarized incidence
$s$	Substrate
SPR	Surface plasmon resonance
$xx$ or $x$	Properties along $x$ direction as a response from the external field in $x$ direction For graphene, the field is parallel to the sheet.
$zz$ or $z$	Properties along $z$ direction as a response from the external field in $z$ direction For graphene, the field is perpendicular to the sheet.

## Abbreviations

AFM	Atomic force microscopy
ATR	Attenuated total internal reflection
CVD	Chemical vapor deposition
DICM	Differential interference contrast microscopy
DFT	Density functional theory
EDS	X-ray energy dispersive spectrometer
EELS	Electron energy loss spectra (or spectroscopy)
EM	Electromagnetic
EMCCD	Electron-multiplied charge-coupled device

FLG	Few layer graphene
FWHM	Full width at half maximum
HOPG	Highly oriented pyrolytic graphite
LED	Light emitting diode
MLG	Multi-layer graphene
NdG	N-doped graphene
p-pol.	p-polarized (light)
PCM	Phase-contrast microscopy
PMMA	Poly-methyl methacrylate
rGO	Reduced graphene oxide
RI	Refractive index
s-pol.	s-polarized (light)
SE	Spectroscopic ellipsometry
SEM	Scanning electron microscopy
SLG	Single layer graphene
SPP	Surface plasmon polariton
SPR	Surface plasmon resonance
SPRM	Surface plasmon resonance microscopy
TEM	Transmission electron microscopy
TIR	Total internal reflection
UV	Ultraviolet
VASP	Vienna ab-initio simulation package (for DFT calculations)
XPS	X-ray photoelectron spectroscopy

# Chapter 1

## Introduction

### 1.1 Background

Graphene, a true two-dimensional, single-atomic layer of honeycomb structure of carbon, has been studied with rapidly increasing interest in various research fields (Figure 1.1), because of its novel electrical, thermal, mechanical, and surface properties (A. K. Geim and K. S. Novoselov, 2007; A. K. Geim, 2009; C. Lee et al., 2008; K. S. Kim et al., 2009; Y. –M. Lin et al., 2008; J. S. Park et al., 2014). While ideal single-layer graphene (SLG, or 1L graphene) provides a genuine 2-D structure with exotic physical properties, studying and producing the multilayer graphene (MLG) is also of great importance, for better extensive properties than SLG (Y. Sui and J. Appenzeller, 2009; P. Gava et al., 2009). Therefore, the reliable counting of graphene layers is essential.

Up to now, several graphene counting methods have been attempted; however, none has proven to be robust and reliable. The new graphene counting method by the surface plasmon resonance (SPR) angle shifts, developed in present work, has turned out to be not only highly repeatable but also accurate, overcoming the limitations of these previous attempts to count graphene layers. This characterization is the starting point of all the other graphene characterizations and measurements, because it defines the existence and identifies the layer number of the 2-D graphene samples.

The relatively significant light absorption of 2 ~ 3% of SLG (R. R. Nair et al., 2008) of mere 0.335 nm implies that the RI of graphene must be complex with a large imaginary component. Notable efforts have been made to determine the complex graphene RI using diverse experimental and theoretical approaches (Z. H. Ni et al., 2007;

M. Bruna and S. Borini, 2009; V. G. Kravets et al., 2010; A. Matkovic et al., 2012; U. Wurstbauer et al., 2010; F. J. Nelson et al., 2010; J. W. Weber et al., 2010; X. Wang et al., 2008; Q. Ye et al., 2013), yet the available data show substantial scattering for both their real and imaginary components. This means that there has not been a reliable method to accurately measure the complex RI of graphene, and the fundamental reasons for this will be discussed later in Chapter 4.

Recently, a large variety of graphene derivatives, such as graphene nano ribbons (GNR) (Y. -W. Son et al., 2006), doped and disordered graphene layers (D. Wei, et al., 2009; M. Y. Han, et al., 2010) are in active research. These manipulations are intended to the electronic band structure engineering of graphene, primarily because they can give graphene a band gap. Consequently, the optical properties of these new categories of materials will also be different from the pristine graphene, because of the changes in the electronic response to the electromagnetic (EM) wave, i.e. light.

Among these graphene derivatives, the nitrogen-doped graphene (NdG) by strong covalent bonding of nitrogen and carbon atoms is one of the most robust materials that can be readily made from CVD, and show clear distinction from graphene: the elevation of the Fermi level (Figure 1.2 from L. Zhao et al., 2011). However, there is no report on the measurement of the optical properties of NdG, and only preliminary studies on the theoretical prediction are present (P. Nath et al., 2014; P. Rani et al., 2014). Thus, the complex RI measurements result for NdG layers in this work is the first report on the effect of atomic doping on the optical properties of graphene. This will suggest the future directions for the design of the optical measurement methods for atomically thin layers such as MoS<sub>2</sub> (B. Radisavljevic et al., 2011), WSe<sub>2</sub> (C. Chiritescu et al., 2007), and Phosphorene (H. Liu et al., 2014).

## 1.2 Previous studies on optical characterization of graphene

Raman spectroscopy, which measures the strong  $G$  and  $2D$  Raman shift peaks of graphene (A. C. Ferrari et al., 2006), has been one of the most widespread tools for easy and fast identification and characterization of graphene layers. This method is used to determine the existence of graphene and to count the layer number of graphene samples, by inspection of either the relative intensities of the  $G$  and  $2D$  peaks or the width and shape of the  $2D$  peak, as presented in Figure 1.3 taken from A. F. Ferrari's work in 2006.

However, it is impossible to accurately count the layer number of the CVD graphene by Raman spectroscopy, since the distinctions of the signals from SLG and those from MLG only comes from the ordered stacking of each graphene layer (L. M. Malard et al., 2009). The individual layers constituting the MLG made from CVD are not stacked in a regular manner, because of the relatively small grain sizes and the manual stacking processes of SLGs. Therefore, the Raman signals will not consistently depend on the layer number of CVD graphene, which means the Raman spectroscopy cannot count the CVD graphene layers properly.

Optical reflection or transmission from graphene layers is also used to characterize the graphene layers (P. Blake et al., 2007; P. E. Gaskell et al., 2009). Because graphene absorbs only 2-3% of the incident light per layer and each layer can absorb different amount of light due to the defects and residues on the layers, the stepwise determination of the graphene layer number is tricky as seen in Figure 1.4 from P. E. Gaskell et al., 2009. This difficulty is not overcome even with a specific substrate which is designed for the maximum sensitivity of graphene by using the constructive interference of the multiple reflections.

### 1.3 Objectives of present study

As presented briefly in the previous sections, the reliable characterization of graphene layers is not straightforward due to the thinness and the sample to sample variations of graphene. For the examination of large areas of CVD graphene layers in relatively short time, the optical methods are appropriate, not using the scanning probe techniques. In this thesis, three major topics are studied: 1. Reliable counting of graphene layers by SPR reflectance, 2. Development of measurement method of graphene's complex RI by the simultaneous use of SPR and ATR, and 3. Experimental measurements of complex RI of NdG made from CVD. Before all of these, fundamentals of near-field optics are summarized to explain the basis of experimental methods used in current study.

In Chapter 2, the theory on near-field optics is covered that is necessary to describe the measurement methods in the subsequent chapters. The concepts in this chapter are general, so they are applicable not only to the graphene layers, but also to all the other 2-D materials thinner than the near-field regime,  $\sim 200$  nm. At first, the theoretical framework for the atomically thin layers is introduced, because it is not as simple as that for the far-field, geometric optics where all the layers and structures have dimensions much larger than the wavelength of light. This argument makes the starting point of the definition of the optical properties of 2-D materials, such as the complex RI (or equivalently dielectric function or optical conductivity). The following sections explain the principles and formulas involved in the near-field phenomena that are integral to understand the measurements methods and analyze the results in this work, i.e. SPR, ATR, and SE.

In Chapter 3, the new graphene layer counting method by SPR is covered. At first, the previous methods for graphene layer counting are presented, listing the limitations of

each technique. Next, the detailed theoretical analyses are covered, for the reflection calculations of the graphene on surface plasmon resonance microscopy (SPRM) and for the enhancement of the SPRM sensitivity to the graphene layers. Finally, experimental results are presented for the 1, 3, and 5L graphene samples. The obtained results are compared with the calculation results to validate the new graphene counting method.

In Chapter 4, the new method to accurately measure the complex RI of graphene is presented, by the tandem use of SPR and ATR. In the first section, the previous methods for the graphene's RI measurements are presented, with the comprehensive comparison of the reported results so far. In the second section, the fundamental reasons for development of this new method are presented, with the fundamental limitations of the conventional methods. In the last section, the results of the complex RI measurements are shown from the 1, 3, and 5L graphene samples' data. The results are compared with previous results of various groups by various methods, as well as with the DFT calculation result conducted by current work.

In Chapter 5, theoretical and experimental work for complex RI of NdG is delivered. First of all, the background of the NdG study is introduced, focusing on the methods for the sample fabrication, prediction of the optical properties of NdG compared with the pristine graphene, and the limitations of the method in the previous chapter when applied to the NdG measurements. Then, the experimental scheme of SE is presented for the better sensitivity of RI and data fitting method to measure the complex RI of NdG. Finally, the measurement results with the SE are given for pristine graphene and NdG, followed by the analysis by comparing them with the DFT calculation results.

Finally, summary and conclusion are given in Chapter 6.

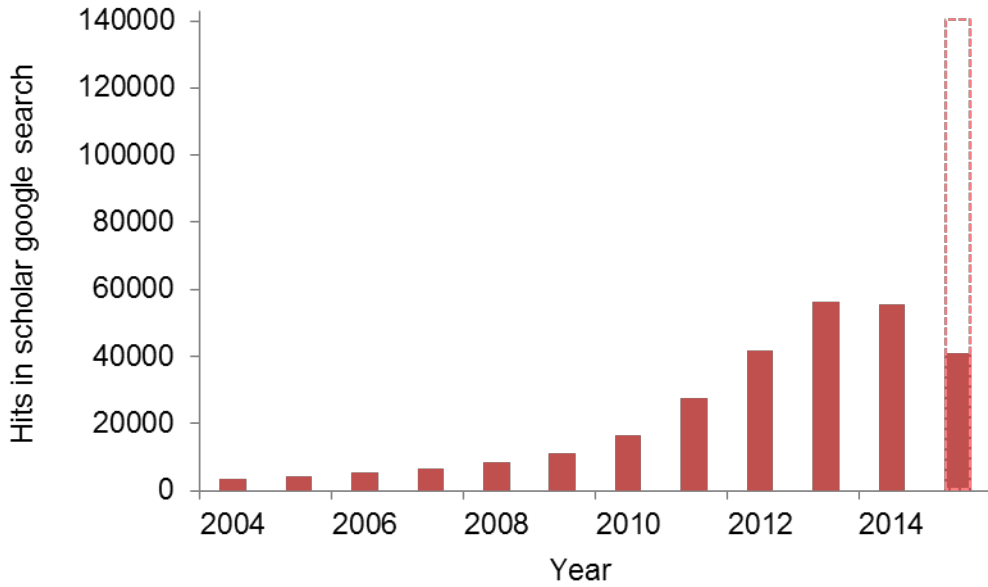


Figure 1.1 The number of appearance of the word “graphene” in the scholar google search (<http://scholar.google.com>), which includes scientific journals, proceedings, books, and patents. The last bar is for this year, already 41000 hits on 14<sup>th</sup> April, so expected to be around 140000 at the end of the year.

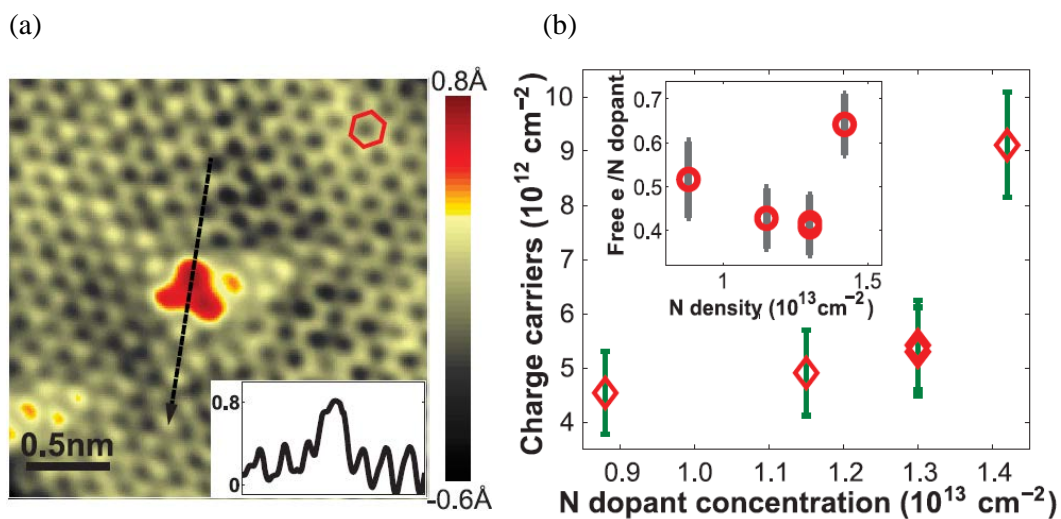


Figure 1.2 (From L. Zhao et al., 2011) STM imaging of nitrogen dopants and doping in NdG. (a) STM image of the most common doping form observed on N-doped graphene on copper foil, corresponding to a single graphitic N dopant. (Inset) Line profile across the dopant shows atomic corrugation and apparent height of the dopant ( $V_{bias} = 0.8 \text{ V}$ ,  $I_{set} = 0.8 \text{ nA}$ ). (b) Spatially averaged graphene charge-carrier concentration as a function of average nitrogen concentration level for five different samples measured on N-doped graphene on copper foil. (Inset) Free charge carriers per nitrogen atom for each of these samples.

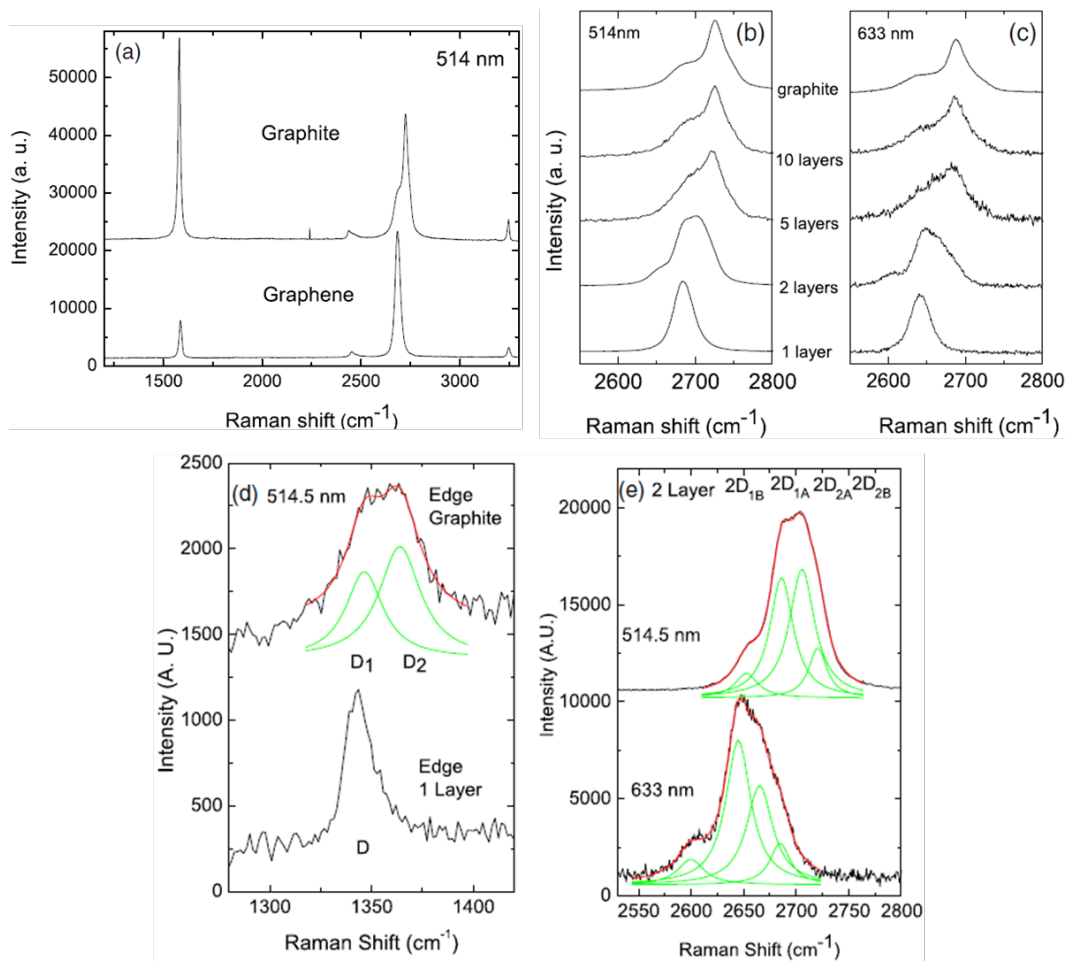


Figure 1.3 (From A. C. Ferrari, 2006) (a) Comparison of Raman spectra at 514 nm for bulk graphite and graphene of different layer numbers. They are scaled to have similar height of the  $2D$  peak at  $\sim 2700 \text{ cm}^{-1}$ . (b) Evolution of the spectra at 514 nm with the number of layers. (c) Evolution of the Raman spectra at 633 nm with the number of layers. (d) Comparison of the  $D$  band at 514 nm at the edge of bulk graphite and single layer graphene. The fit of the  $D_1$  and  $D_2$  components of the  $D$  band of bulk graphite is shown. (e) The four components of the  $2D$  band in 2 layer graphene at 514 and 633 nm.

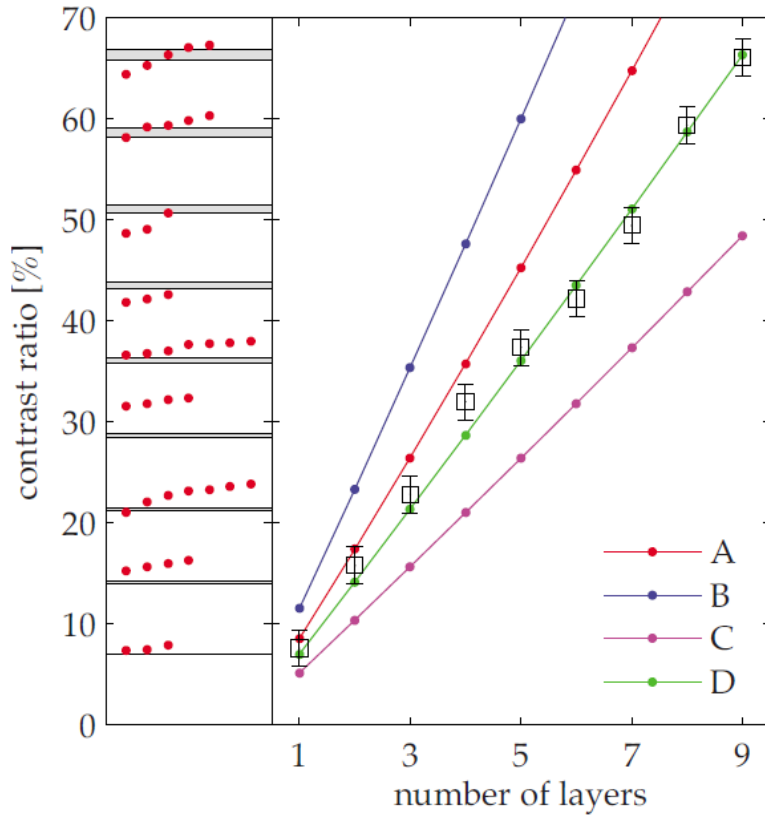


Figure 1.4 (From P. E. Gaskell et al., 2009) Left: Measured contrast ratios for 41 unique graphitic flakes. Theoretical contrast ratios based on Fresnel theory with  $m$ -layer graphene conductance  $Z_0 G = m\pi\alpha$  are plotted as bands for a substrate refractive index  $n_s = 1.522 \pm 0.004$ . Right: Contrast ratios for each layer, including error due to camera nonlinearity and lamp power fluctuation, compared against Fresnel theory with reported graphite indices (A)  $RI_g = 2.675 + 1.35i$  (E. D. Palik, 1998), (B)  $RI_g = 2.52 + 1.94i$  (G. E. Jellison et al., 2007), a reported graphene index (C)  $RI_g = 2.0 + 1.1i$  (Ni et al., 2007), and universal conductance (D) (R. R. Nair et al., 2008). Note that in original paper of P. E. Gaskell et al., the imaginary parts of the RI of graphite and graphene are negative, because

they used the opposite convention for the time dependence of the electromagnetic field oscillation.

## Chapter 2

### Near-field optics for sub-nm-thin materials

#### 2.1 Refractive index (RI) of a sub-nm layer

In principle, the refractive index (RI) is defined for the materials composed of a number of atoms that can generate the collective response to the external EM waves (J. D. Jackson, 1999). Therefore, this classical concept of the RI cannot be directly applied for the 2-D materials with sub-nm thicknesses. Because the RI and the thickness of a layer can determine all the optical response of it in principle, namely reflection, transmission, and absorption of light, reconciliation of this problem is essential to characterize the optical properties of sub-nm layers such as graphene and other 2-D materials. In this section, the theoretical framework to deal with these atomically thin films in this work is presented.

##### **2.1.1 Graphene modeled as a surface current without thickness**

In the early stage of graphene research, the common method to deal with the graphene in optical calculations was to regard it as a surface current without thickness (R. R. Nair et al., 2008). However, some articles considered graphene as a thin film having the finite thickness of  $\sim 0.335$  nm (Z. H. Ni et al., 2007; M. Bruna and S. Borini, 2009; V. G. Kravets et al., 2010; A. Matković et al., 2012; U. Wurstbauer et al., 2010; X. Wang et al., 2008; Q. Ye et al., 2013), which is only the nominal thickness defined from the interlayer distance between layers in highly ordered pyrolytic graphite (HOPG). In one side, the first approach is legitimate that the physical thickness of the single-atom layer can be neglected compared with the wavelengths of light,  $\sim 500$  nm. On the other hand,

the second view can be more apposite in near-field regimes, where the thickness matters because of the effects of reflection interferences from the finite thickness of the layer.

To determine whether the surface current modeling and the finite thickness modeling result in discernable difference, calculations are done for the two schemes. The physical system for this test is the ATR signals from the interface composed of prism (BK7, RI=1.515), graphene, and air. In the calculation for the finite thickness modeling, the reflection coefficients of Fresnel's equations (J. D. Jackson, 1999) combined with the multilayer formula widely used for SPR reflectance (K. Kurihara and K. Suzuki, 2002; K. D. Kihm et al., 2012) are used.

The calculation results in Figure 2.1 show that the two schemes fall into almost the identical results of the reflectance, for the wide range of incident angle and both of the polarizations<sup>1</sup>. This means that the light interactions with graphene do not have to be described by the wave optics, but can properly be explained by the Fresnel's equations and infinite series summation of the light from each interface. In this model, graphene is regarded as a film with the "effective thickness" of 0.335 nm and the corresponding "effective RI<sub>G</sub>". For the calculations shown in Figure 2.1, RI<sub>G</sub> in the finite thickness model is taken from a DFT calculation result in (M. Klintenberg et al., 2009) and the corresponding optical conductivity of graphene is obtained by the relation between RI and optical conductivity described in C. A. Balanis, 1989.<sup>2</sup>

---

<sup>1</sup> The p- and s-polarization means the light where the electric fields are oscillating in and perpendicular to the plane of incidence, which is made by the incident ray and the normal vector of the surface starting from the point where the ray hits the surface.

<sup>2</sup> In the reference, the relationship between complex dielectric constant and optical conductivity is given, and the RI can be readily obtained by the relation,  $RI = \sqrt{\text{dielectric constant}}$

### 2.1.2 Effects of birefringence of a sub-nm layer

Another issue in the optical calculations of reflection from the 2-D materials is that the layered materials must inherently have different RI values for different light polarizations, which is called the birefringence. For example, graphene has electrons that can move freely in the 2-D honeycomb sheet<sup>3</sup>, so light with the EM fields parallel to the graphene layer, i.e. propagating normal to the graphene layer, sees it as a metallic object, having relatively large imaginary component of RI. However, if the light travels parallel to the graphene sheet, the electrons in graphene cannot move freely across the graphene layer, so the imaginary part becomes negligible. This phenomenon is clearly realized by the DFT calculation by M. Klintonberg et al., 2009.

Thus, the reflection calculations from graphene layers with isotropic and anisotropic RI values are conducted for the same situation as in the previous section (2.1.1) to evaluate how much the birefringence affects the reflection. The calculation method for the isotropic graphene layer is the same as that in the previous section, Fresnel's equations from multilayer interface with graphene of finite thickness. The reflection from the anisotropic layer can be obtained by changing the reflection coefficients as in (D. L. Greenaway, et al., 1969). One of the coefficients, for p-polarization across the 1<sup>st</sup> medium and graphene, changes from

$$r_{p,12} = \frac{RI^2 \cos \theta - n_1 (RI^2 - n_1^2 \sin^2 \theta)^{1/2}}{RI^2 \cos \theta + n_1 (RI^2 - n_1^2 \sin^2 \theta)^{1/2}} \quad (2.1)$$

to

---

<sup>3</sup> An ideal graphene without any doping at temperature 0 K doesn't have free electrons. However, in practice, the finite doping from ambient water vapor and the thermal excitation by the room temperature make the electrons move in the graphene sheet.

$$r_{p,12} = \frac{RI_x RI_z \cos \theta - n_1 (RI_z^2 - n_1^2 \sin^2 \theta)^{1/2}}{RI_x RI_z \cos \theta + n_1 (RI_z^2 - n_1^2 \sin^2 \theta)^{1/2}} \quad (2.2)$$

where  $RI$ ,  $n_1$ ,  $RI_x$ ,  $RI_z$ , and  $\theta$  are isotropic RI of graphene, RI of 1<sup>st</sup> medium, anisotropic graphene RI for the light propagating normal to the graphene, that for the light parallel to the graphene, and the incident angle at the 1<sup>st</sup> medium, respectively.

The results for the anisotropic graphene layer are shown in Figure 2.2. It turns out that the anisotropy of the atomically thin graphene doesn't change the reflection significantly, which can be attributed to the infinitesimally thin graphene layer compared to the wavelength of light. Thus, the optical measurements with the reflection characterizations are insensitive to the  $RI_z$  component of graphene, and only the  $RI_x$  is relevant. This means that the ordinary optical characterizations cannot detect the  $RI_z$ , while it also says that  $RI_z$  is not important in practical applications because it doesn't affect the optical response of the graphene much.

In conclusion, in the optical characterizations of graphene by the reflection of light, modeling graphene as a sheet of thickness 0.335 nm and an effective, isotropic RI value is appropriate, because the effect of  $z$  component of graphene to the results is negligible.

## 2.2 Surface plasmon resonance (SPR)

### 2.2.1 Principles of SPR

In quantum physics, the wave-particle duality is the basic concept that can explain lots of physical phenomena, and some of these kinds of entities are written as the “quasi-particles”. Photons and phonons are two typical words showing this duality, where they indicate the EM waves and the lattice vibration modes respectively. “Surface plasmons”

and “polaritons” are two types of quasi-particles that can exist on (or around) metals that containing abundant free charge carriers. Plasmon refers to dipole carriers, such as free electrons oscillating in the background ions of a metal. Thus, surface plasmon implies that the charge density wave along the metal’s surface (S. Maier, 2007). When the metal surface is illuminated by photons, these entangled quasi-particle modes are excited, composed of surface plasmons and photons, which are called surface plasmon polaritons (SPPs) (U. Fano, 1956).

Kretschmann’s layout for the excitation of the SPPs (Figure 2.3) enables to observe a significant reduction in reflectance from the level of the total internal reflectance, by the resonant coupling of the SPPs on the Au film. The thickness of the Au film should be optimized according to the wavelength of the excitation, which is 48 nm for  $\lambda=634$  nm in this work. The incident angle for the maximum resonance and the minimum reflection is called the SPR angle,  $\theta_{\text{SPR}}$ . This yields a dip in the reflectance curve, when plotted for the range of incident angles, and both the shape of the dip and the SPR angle show the most sensitive changes to the optical and physical parameters of the contacting medium on the metal film (K. D. Kihm et al., 2012), which is at present the graphene layers.

Fresnel’s reflectance equation for the original three-layered Kretschmann’s layout is revised to the four-layered structure (Figure 2.4-a) where the graphene is inserted as the third layer between gold and medium. The reflection formula for this system is given by (R. M. A. Azzam and N. M. Bashara, 1977):

$$R = \left| \frac{[r_{12} + r_{12} \exp(-i2k_{z2}d_2)] + [r_{12}r_{23} + \exp(-i2k_{z2}d_2)]r_{34} \exp(-i2k_{z3}d_3)}{[1 + r_{12}r_{23} \exp(-i2k_{z2}d_2)] + [r_{23} + r_{12} \exp(-i2k_{z2}d_2)]r_{34} \exp(-i2k_{z3}d_3)} \right|^2 \quad (2.3)$$

$$r_{ij} = \frac{\varepsilon_j k_{zi} - \varepsilon_i k_{zj}}{\varepsilon_j k_{zi} + \varepsilon_i k_{zj}} \quad (2.4)$$

$$k_{zi} = \frac{2\pi}{\lambda} \sqrt{\varepsilon_i - \varepsilon_1 \sin^2 \theta} \quad (2.5)$$

where the subscripts  $i, j = 1, 2, 3$  or  $4$  represent the prism, the gold film of thickness  $d_2$ , the graphene layers of the nominal thickness  $d_3 = L$  (number of atomic layers) $\times 0.335$  nm, with the environmental medium with dielectric constant of  $\varepsilon_4$ ,  $\lambda$  is the wavelength of incident light (in vacuum), and  $\theta$  is the incident angle at prism. It is clear that the reflectance,  $R$ , is a function of the number of graphene layers,  $L$ .

### 2.2.2 SPR microscopy (SPRM)

The SPR system can be used as a microscopic imaging system, which can observe the very small changes of the RI on the Au surface, being sensitive only to the near-field region,  $\sim 200$  nm from the medium/Au interface. This is achieved as seen in Figure 2.4-b by the collimated light with homogeneous illumination over the region of interest, and the electron-multiplied charge-coupled device (EMCCD) camera (Pro EM 512B, Princeton Instruments) combined with an objective lens (5X EO M Plan Apo Long Working Distance Infinity-Corrected, Edmund Optics) and a tube lens (CMM 1.0 $\times$  or CMM 2.0 $\times$ , SPO Inc.) that detect the reflection field. The main frame of the experimental system is comprised of two rotatable arms and a prism assembly placed near the pivot point (Figure 2.4-b): (1) the left arm consists of the incident LED light source of 634 nm wavelength with a FWHM (full width half maximum) of 22 nm, a polarizer and collimating optics, (2) the right arm consists of an camera and microscopic lens assembly, and (3) the top surface of the BK7 prism accommodates an index matching BK7 glass slide that is coated with a 48-nm thick gold layer.

Before the characterizations of graphene layers, a preliminary experiment on an evaporating water droplet is conducted. The four images taken in the middle of the evaporation are shown in Figure 2.5. Since the incident angle is  $\sim 44^\circ$ , which is the SPR angle for the air, the background is very dark due to the minimum reflection by the SPR. In contrast, the droplet is imaged bright from the reflected light because the water has different RI value than air. One can also calculate the contact angle of the water droplet by measuring the interval between fringe patterns by a simple formula (A. Otto and W. Sohler, 1971; G. Hass et al., 1977), and it evolves from  $7^\circ$  to  $2^\circ$  in this work.

### 2.2.3 SPRM images of graphene layers

Graphene layers can be imaged by the SPR reflection when laid on top of the Au film of SPRM due to their finite thicknesses and dielectric constants ( $=RI^2$ ), as presented in the equations (2.3), (2.4), and (2.5). The images of a graphene sample are shown in Figure 2.6-a. The samples are made from the conventional method which uses the CVD on Cu foil and the transfer using PMMA<sup>4</sup> (poly-methyl methacrylate) (S. Bae et al., 2010). The four figures are taken at incident angles around the SPR angles of the Au/air (second from left) or Au/air/graphene (third from left). Note that the in the second and third photos, the background and graphene region are the darkest, respectively. Therefore, the optical contrasts are higher than ordinary optical microscopy (P. Blake et al., 2007), thanks to the dark background.

The reflectance values from SPRM images for various incident angles are plotted in Figure 2.6-b, with the calculation results by the equations (2.3), (2.4), and (2.5) assuming

---

<sup>4</sup> For MLG samples, the PMMA transfer processes were repeated multiple times.

the RI of graphene to be  $2.95+1.49i$  from (M. Klintonberg et al., 2009). The two curves for Au/air and Au/air/graphene cross at the incident angle of  $44^\circ$ , which means the graphene is brighter below  $44^\circ$  and darker above  $44^\circ$  than background in images, as shown in Figure 2.6-a. The shift of the reflectance curve by the existence of the graphene layer is similar to that predicted by the calculations, yet the absolute intensity values are different from expected. This is attributed to the various experimental uncertainties, such as the Au thickness different than the ideal 48 nm, Ti or Cr adhesion layer of  $\sim 5$  nm between the glass and Au film<sup>5</sup>, and the minute amount of background light captured by the sensitive EMCCD camera.

---

<sup>5</sup> The effect of this adhesion layers to the reflectance calculation is reported in K. D. Kihm et al., 2012.

## 2.3 Attenuated total internal reflection (ATR)

### 2.3.1 Principles of ATR

When light travels from a medium with higher RI to another medium with lower RI, it is refracted in such a way that the angle made by the ray and the surface normal vector becomes larger than that in the first medium. At a certain angle called critical angle, the light cannot travel across the interface, and above this critical angle, all the light is reflected back to the first medium. This phenomenon is called the total internal reflection (TIR), which occurs when light travels across the clean interface of glass and medium (air or water in current study), with the incident angle larger than the critical angle.

Even though the TIR does not allow the light traveling into the second medium, there is still the evanescent field at the near-field region just above the surface of the glass, of which the intensity decays fast with the distance from the interface (J. D. Jackson, 1999). This mode of light doesn't carry the energy, so the reflectance is 1 for the TIR.

However, when there is a light-absorbing layer on the glass, the TIR is attenuated, because some portion of the incident light is absorbed by the layer. This is called attenuated total internal reflection (ATR), and the amount of attenuation can be calculated using the Fresnel's equations and multiple reflections modeling, as in the calculation for the SPR<sup>6</sup>. Graphene is a light absorbing material, so it also diminishes the TIR, so the ATR can be used as a probe of the graphene layers.

---

<sup>6</sup> In this case, the 2<sup>nd</sup> layer changes from the Au layer in SPR calculation to the absorbing layer.

### **2.3.2 ATR images of graphene layers**

Graphene can be imaged by the ATR, if only the Au layer in Figure 2.4-a is eliminated. The calculation results for the reflection from the glass/air and glass/graphene/air are shown in Figure 2.7. The reflection of the s-polarized light is absorbed more than the p-polarized light by the existence of graphene. This is easily explained because the electric field of the s-polarized light is parallel to the graphene sheet, so the electrons in graphene feel the electric field more, and the absorption is larger. ATR images of a 2-layer graphene sample are given in Figure 2.8, where the graphene is much more distinctive with the s-polarized illumination as proved by the calculation results in Figure 2.7.

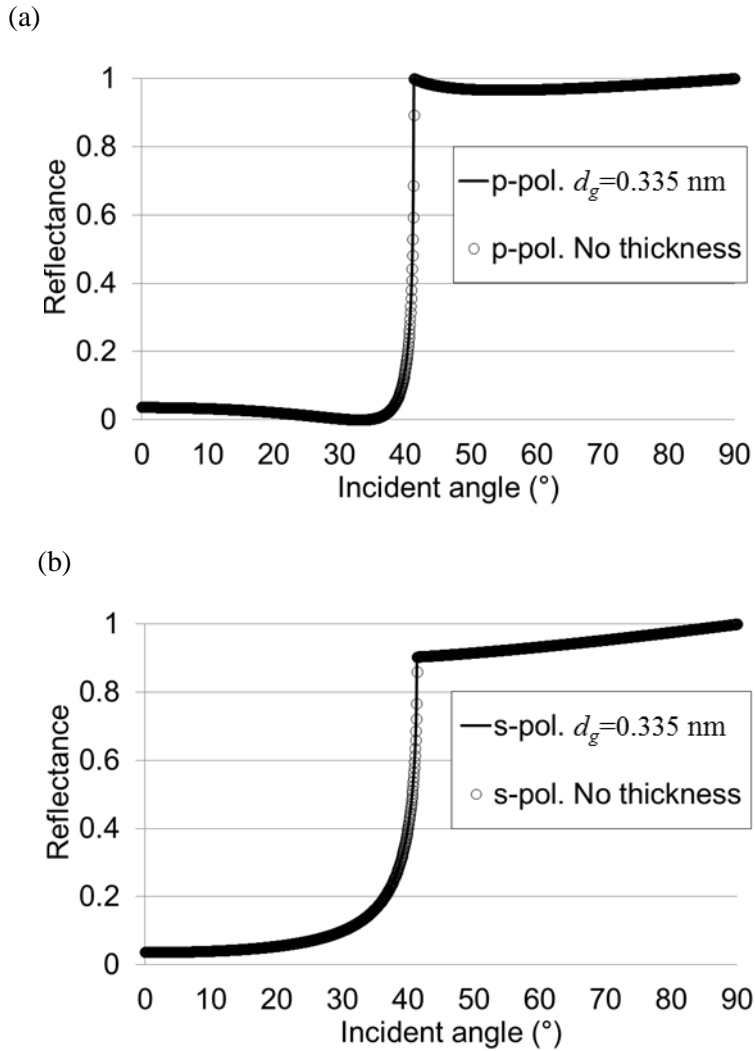


Figure 2.1 Attenuated internal reflection calculation results (Finite thickness vs. no thickness with surface current) for the graphene on a BK7 prism where the light is coming from the lower side of the prism. The solid curves are the for the finite thickness (0.335 nm) modeling of graphene, based on Fresnel's equations for the multilayer calculations, and the open circles are the results when the thickness is ignored and only

the surface current is considered. The p-polarized (a) and s-polarized (b) light do not show any distinguishable difference between the two modeling schemes.

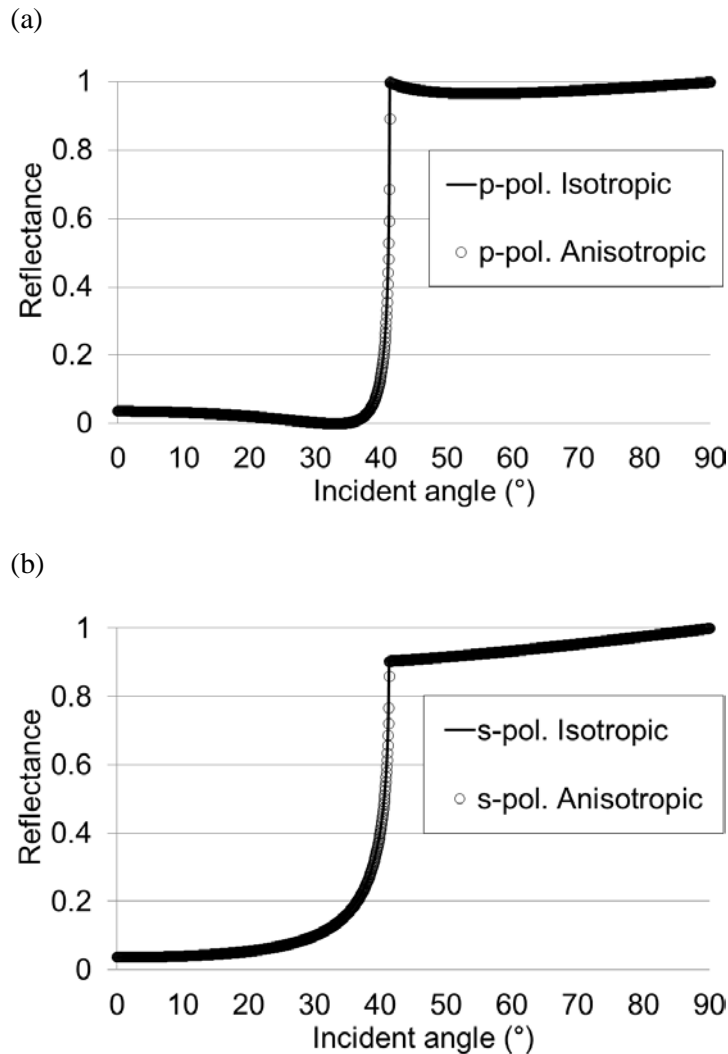


Figure 2.2 Attenuated internal reflection calculation results (Isotropic vs. anisotropic graphene) for the graphene on a BK7 prism where the light is coming from the lower side of the prism. The solid curves are for the isotropic RI of graphene, based on Fresnel's equations for the multilayer calculations, and the open circles are the results when the birefringence is considered. The p-polarized (a) and s-polarized (b) light do not show any distinguishable difference between the two modeling schemes.

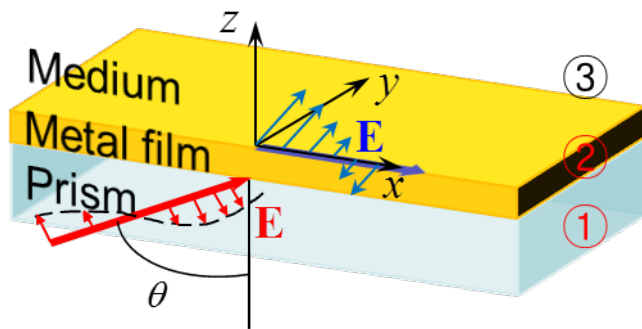
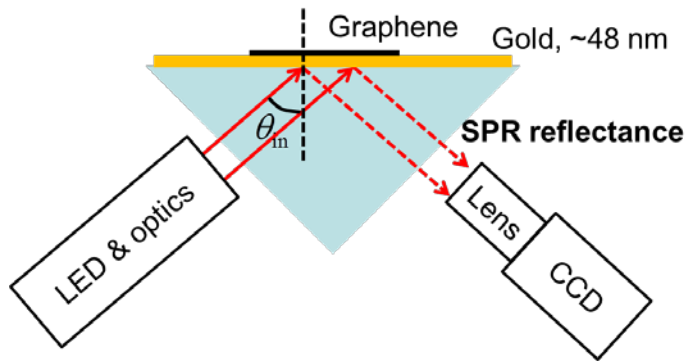


Figure 2.3 (Also in K. D. Kihm et al., 2012) Kretschmann's configuration of a three-layered SPR system consisting of (1) prism, (2) metal film, and (3) medium.

(a)



(b)

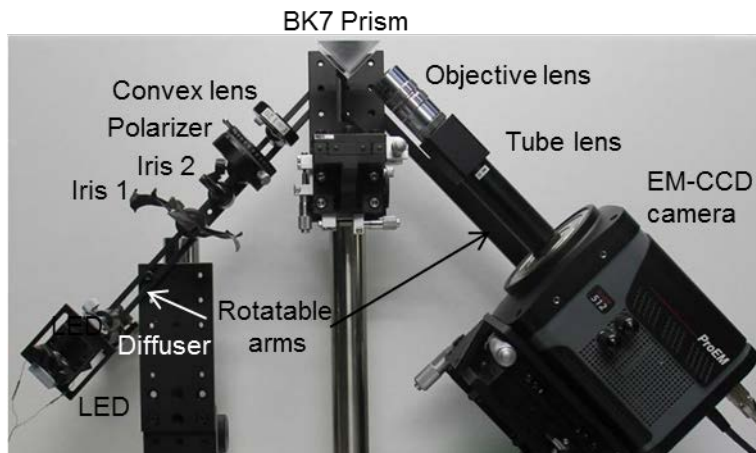


Figure 2.4 The SPRM for graphene characterizations. (a) Schematic of the four-layered system for graphene counting with SPRM, (b) the corresponding experimental setup (also in S. Cheon et al., 2014).

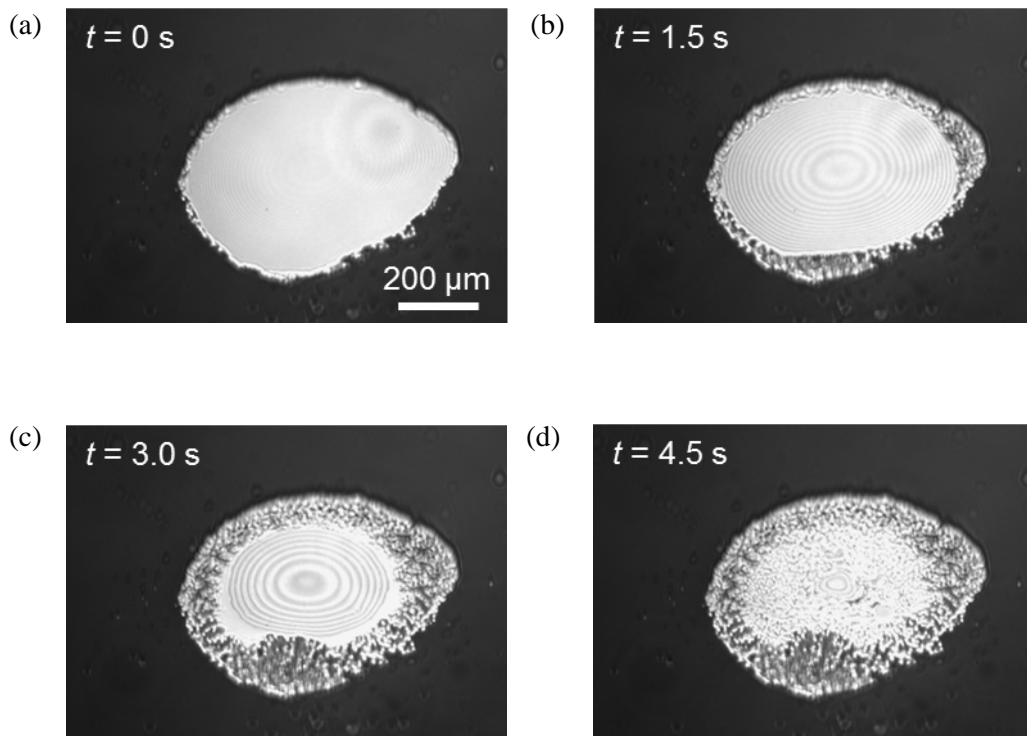
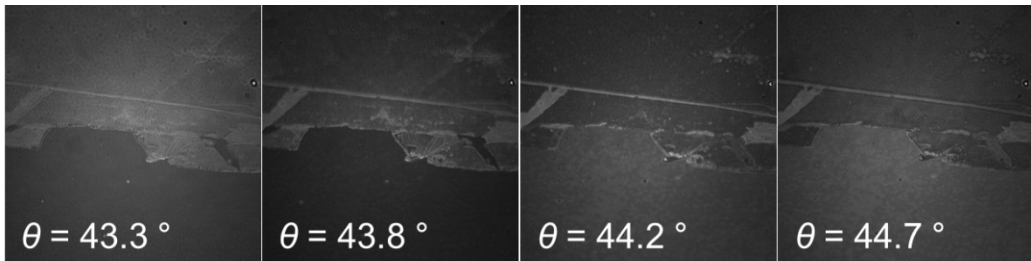


Figure 2.5 The evaporation of a water droplet imaged by the SPRM system developed in current work, which is shown in Figure 2.4-b. The fringe patterns can be used to calculate the contact angle change, which is from  $\sim 7^\circ$  to  $2^\circ$ .

(a)



(b)

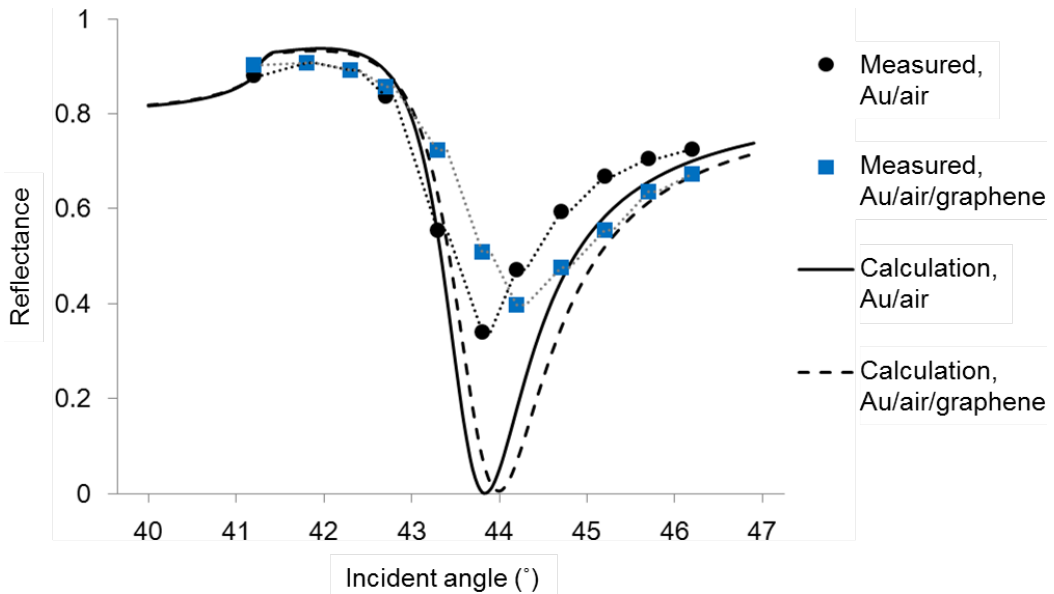


Figure 2.6 The SPRM images of 3-layer graphene and the reflectance vs. incident angle data. (a) Four SPRM images while increasing the incident angle of the light. SPR angle of Au/air corresponds to the incident angle of the second picture, which is depicted by the darkest background. The third image is for the SPR angle of Au/air/graphene configuration, so the graphene is darkest among the four pictures. (b) Reflectance vs.

incident angle curves for the measured and calculated results. Although the absolute values are not identical, the measurements follow the trends of calculation results.

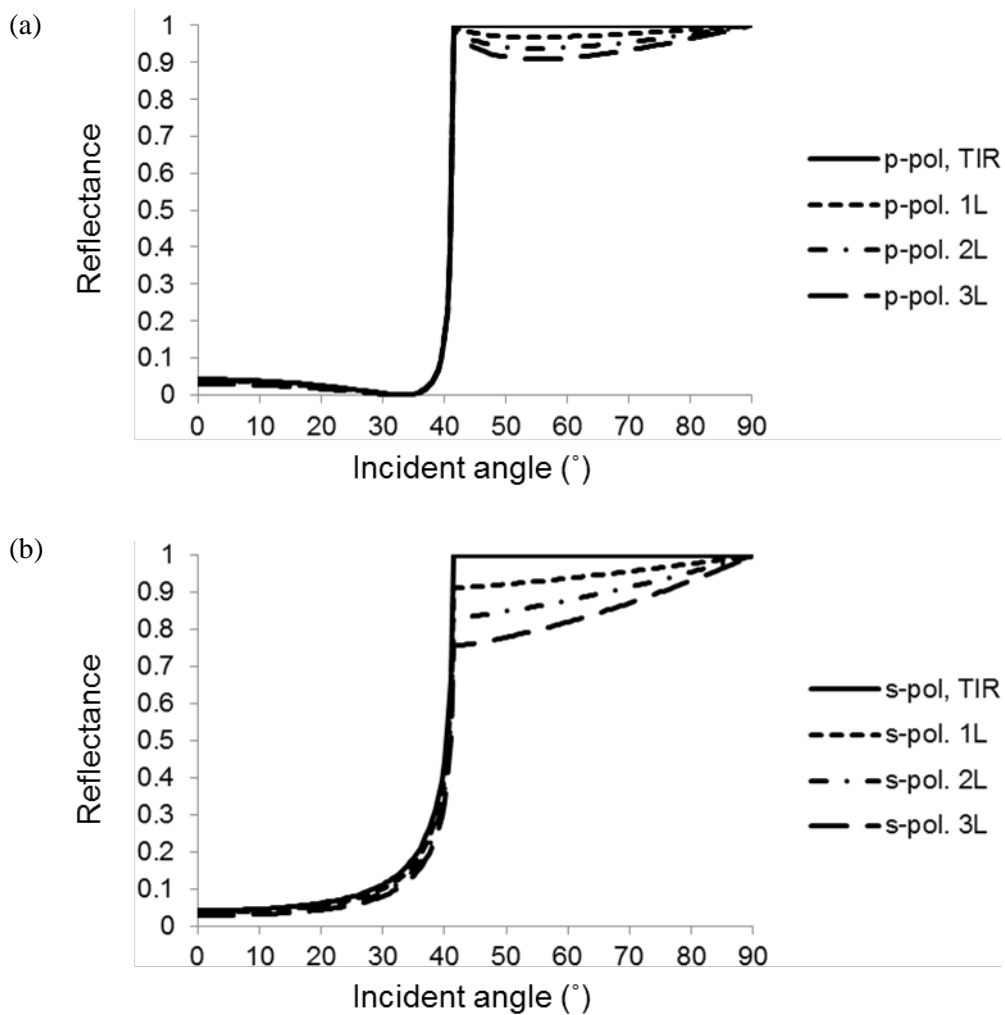


Figure 2.7 Calculation results of the ATR from the 1, 2, and 3-layer graphene for p-polarized (a) and s-polarized (b) light. The s-polarized light is attenuated more by the graphene layers.

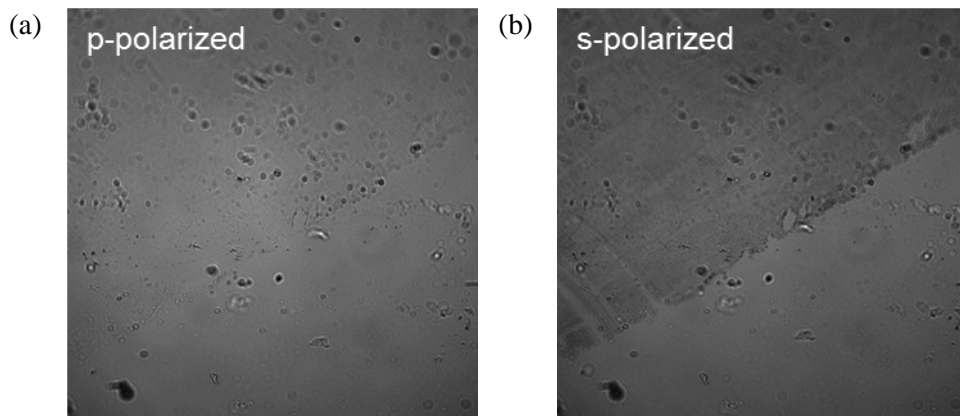


Figure 2.8 ATR images of  $2L$  graphene for (a) p-polarized and (s) polarized light. As predicted in the calculation results in Figure 2.7, the s-polarized light show much larger contrast from the better sensitivity of graphene.

# Chapter 3

## Graphene layer counting by SPR

### 3.1 Previous methods for graphene layer counting

#### 3.1.1 Raman spectroscopy

One graphene-counting method, Raman spectroscopy, has already been attempted and it has been widely used so far. It measures the phonon distributions of the graphene layers by detecting the Raman shift of the incident laser frequency, but the signals are not distinct enough to count the number of layers beyond the third (A. C. Ferrari et al., 2006; D. Graf et al., 2007; L. Calizo et al., 2007; A. Gupta et al., 2006). This technique is highly sensitive to impurities and surface charges in the graphene layers, as well as to the crystallinity of the substrate, which hinders the accurate counting of graphene layers. In addition, a universally acceptable way of interpreting the Raman shifts in order to precisely count the number of graphene layers has yet to arise under controversy. In fact, attempts to use the G band shift (C. Casiraghi et al., 2007), the ratio of G and 2D bands, and the deconvolution of the 2D band for counting graphene layers have all been dismissed for multiple reasons, including the limited spectroscopic resolution ( $\sim 1 \text{ cm}^{-1}$ ), the extrinsic effects associated with charged impurities and defects, and the necessity of 2D band deconvolution by more than 15 peaks for FLG (L. M. Malard et al., 2009).

#### 3.1.2 Atomic force microscopy

Another counting method, atomic force microscopy (AFM), simply measures the total thickness of FLG and then divides it by the known thickness of SLG to determine the number of layers of FLG (K. S. Novoselov et al., 2004). This sounds straightforward, at least in principle, despite its disadvantage of being intrusive with the AFM probe.

However, the reference thickness occupied by SLG in conforming to FLG can have uncertainties up to 50%; i.e., from the nominal 0.335 nm (A. Gupta et al., 2006) to the maximum 0.5 nm (K. S. Novoselov et al., 2004), depending on the fabrication and cleaning processes. Also, the unknown gap thickness between adjacent layers may also contribute to the intrinsic uncertainties of this technique. Furthermore, this method is limited to small-sized graphene layers allowing the scanning of its edges and does not work when the graphene size exceeds the scanning range of the AFM probe.

### **3.1.3 Reflection or transmission contrast**

An optical counting technique has also been attempted by measuring the reflection from the graphene laid on SiO<sub>2</sub>/Si wafers with the SiO<sub>2</sub> layer thickness of 300 nm to maximize the counting sensitivity from the highest contrast (P. Blake et al., 2007). The reflection intensity, however, may not be consistent if the incident light has inhomogeneous intensity profiles and/or an inevitable Gaussian shape when focusing with an objective lens. This technique is limited in scope to qualitatively or approximately measure differences between graphene samples having different number of layers. Another optical attempt used both phase-contrast microscopy (PCM) and differential interference contrast microscopy (DICM) to count the graphene layers (K. D. Kihm et al., 2011). This method was also based on detection of the graphene layer edges, however the technique allowed only for distinguishing SLG from FLG, but failed to precisely count the layer numbers of FLG samples.

## **3.2 Theoretical analyses for graphene on SPRM**

### **3.2.1 Reflection calculations for multi-layer systems**

In the section 2.2.1, the formula to calculate the reflection from the prism/Au/graphene/medium is presented and it is shown in a reference (K. D. Kihm et al.,

2012) that the adhesion metal layer beneath the Au film does not affect the reflection characteristic significantly<sup>7</sup>. By using the equations (2.3), (2.4), and (2.5), the reflectance vs. incident angle curves can be calculated and the plots are in Figure 3.1, for the 1, 3, 5, 10, and 20L graphene layers, where the medium on the graphene being either air (Figure 3.1-a) or water (Figure 3.1-b). The wavelength in the calculation is 650 nm, RI values of each of the layers are taken from the online database<sup>8</sup>, and the complex RI value of graphene is set  $2.96+1.49i$  from a reference (M. Klintonberg et al., 2009).

In practice, the graphene sample may have thin air gaps as a result of the layer-by-layer transfer of SLGs on the gold film. However, the reflectance should not be significantly altered by the air gaps since what matters is the electronic response from the graphene layers. In other words, the reflectance is primarily determined by the effective thickness of the graphene layers, so the actual layer number of graphene, not the “height” of the graphene stack, determines the SPR reflectance.

### **3.2.2 Configuration to enhance the SPRM sensitivity**

By comparing Figure 3.1-a and b, it is evident that the water environment provides a larger SPR angle ( $\sim 72^\circ$ ) than the usual air environment ( $\sim 43.8^\circ$ ). This is because the water has different RI compared to air, and the dispersion relation of the surface plasmons on Au surface changes. This requires a larger matching horizontal component of the resonant wave vector of the incident light, which itself necessitates a larger incident angle, i.e. a larger SPR angle than in the case with the air environment (K. D. Kihm et al., 2012).

---

<sup>7</sup> It changes the amplitude of the reflectance, but the SPR angle and the normalized reflectance vs. incident angle remain almost the same.

<sup>8</sup> <http://refractiveindex.info>, values at  $\lambda=650$  nm.

Note that a larger SPR angle also ensures larger magnitude of SPR angle shifts, which can favorably enhance measurement accuracy by the enhanced sensitivity of the graphene layers. Furthermore, in the experiments, the refraction at the prism facet which is making  $45^\circ$  with horizon magnifies the angle shift. Therefore, the small difference in the incident angle at the prism/Au/graphene/medium interface can be realized by the large difference of the angle of the beam before the first facet of the prism, which is actually measured.

The SPR angles and the dipped shapes of the reflectance curves predict clear distinctions depending on the number of layers, up to the maximum of approximately 20. The narrower dip of the reflectance curve for the case of the Ag metal layer (K. D. Kihm et al., 2012) suggests its potentially superior measurement sensitivity to the SPR angles than that of the Au layer, but the Ag surface is too easily oxidized for practical use in an ordinary laboratory environment. Thus, a 48-nm thick Au film layer is selected for use for the present experiment to count the number of graphene layers.

### 3.3 Experimental results

SLG is synthesized by the CVD process using a copper substrate (S. Bae et al., 2010). Note that the CVD process using a nickel substrate is known to be more prone to multilayer graphene samples of uncontrollable layer numbers (X. S. Li et al., 2009). MLG is then constructed by repeating the PMMA transfer process (S. Bae et al., 2010) of SLG onto a gold surface, which is coated to a 48-nm thickness on top of a BK7 glass slide (RI = 1.515). Three different samples are prepared with 1-, 3-, and 5-graphene layers on the gold surface-coated glass slide (Figure 3.2). The BK7 glass slide and the BK7 prism are joined by the index matching fluid.

Preliminary examination of these three samples is conducted by analyzing their Raman spectra signals (Figure 3.3), which are corrected for the background signal coming from the gold surface. The Raman spectra of the three samples show no prominent *D* peak ( $1340\text{ cm}^{-1}$ ), indicating that the level of defects in our graphene samples is very low (A. C. Ferrari et al., 2006). Despite our repeated attempts, however, it was not possible to confirm a reliable Raman correlation with the number of layers. As aforementioned, the random stacking of CVD MLGs does not allow for consistent Raman correlation with the number of graphene layers, unlike the exfoliated MLGs from highly ordered pyrolytic graphite. The resulting Raman spectra for the MLGs look similar to those of the SLG except for the relatively enhanced intensities (J. Hass et al., 2008; Z. Ni, et al., 2008). The intensity ratio of the *G* peak to the *2D* peak ( $2680\text{ cm}^{-1}$ ) also randomly varies with the layer number, that is,  $G/2D = 0.29, 0.30,$  and  $0.25$  for *1L*, *3L*, and *5L* graphene respectively, without any consistency.

### **3.3.1 SPRM images of 1, 3, and 5-layer graphene**

The SPRM images by using either air or water environment are presented in Figure 3.4. Figure 3.4-a is the picture taken from the graphene edge of the *5L* sample which is showing the clear boundaries of graphene layers. Figures 3.4-b, c, and d are for the separate *1L*, *3L*, and *5L* samples whose photographs are shown in Figures 3.1 and 3.2, in the water environment to enhance the sensitivity of the graphene layer counting as explained in 3.3.2.

### **3.3.2 SPR curves and SPR angles**

From the intensity levels of the graphene and water regions in Figure 3.4-b, c, and d, the reflectance can be extracted for a single incident angle of  $72.1^\circ$ . For the construction

of the reflectance vs. incident angle curves, and finally the SPR angle, a number of images should be taken, while changing the incident angle by small degree at a time. In this study, those images are taken from about 30 incident angles, from  $\sim 69^\circ$  to  $\sim 74.5^\circ$ , where the increment is around  $0.2^\circ$ .

Figure 3.5 shows the resultant SPR curves for the void (no graphene), 1L, 3L, and 5L graphene, normalized for each dataset to have the minimum of 0 and maximum of 1<sup>9</sup>, each with the calculation results (3.2.1). Each symbol represents the measured reflectance intensity, which is spatially averaged over an area of  $1.7 \times 10^3 \mu\text{m}^2$  on the graphene surface, and the solid curves represent calculations. The uncertainty bars denote the ranges of the reflectance in the three different regions cropped in an image.

### 3.3.3 Data analysis and discussions

Table 3.1 shows the dependence of the SPR angle predictions on the number of graphene layers for three different choices of dielectric constants of graphene. Our measured SPR angles turn out to best agree with the calculations using the dielectric constant predicted by the density functional theory (DFT) (M. Klintonberg et al., 2009). The measured dielectric constant using picometry (X. Wang et al., 2008) provides almost identical results to the case using the DFT, within the angle detection uncertainty

---

<sup>9</sup> This is based on the analysis that the layer number of graphene changes the SPR curve almost horizontally, so the absolute values can be normalized. In practice, the realization of the absolute values of reflectance is extremely difficult, since all the properties and thicknesses of the involved layers (adhesion layer of Ti, Au film, graphene, polymer residues, adsorbed water molecules, etc.) should be known in absolute perfection, with the perfect alignment and polarization of light.

of  $\pm 0.1^\circ$  of the digital protractor (Model Pro3600 of SMARTTOOL). In contrast, the SPR angles using the spectroscopically determined dielectric constant (Z. H. Ni et al., 2007) noticeably deviates from the measured data; this is because of the wrong assumption made in the article that the dielectric constant is independent of the incident wavelength.

In conclusion, the number of CVD graphene layers is optically determined based on the SPR angle shifts. This method is far more consistent and repeatable than any of the previous attempts, including Raman spectroscopy, the relative reflectance or transmittance variations, microscopic imaging techniques, and AFM. Furthermore, the reflectance calculations using Fresnel's equations provide theoretical support to the SPR method by showing excellent agreement with the measured SPR angles.

$\varepsilon_G$	$L=0$	$L=1$	$L=3$	$L=5$
	Measured SPR Angles			
	$71.9 \pm 0.1^\circ$	$72.3 \pm 0.1^\circ$	$73.0 \pm 0.1^\circ$	$73.9 \pm 0.4^\circ$
	Calculated SPR Angles			
$6.19+8.64i$		$72.2^\circ$	$73.1^\circ$	$73.9^\circ$
$7.04+8.40i$	$71.9^\circ$	$72.3^\circ$	$73.1^\circ$	$74.0^\circ$
$2.79+4.40i$		$72.1^\circ$	$72.7^\circ$	$73.3^\circ$

Table 3.1 (Also in S. Cheon et al., 2012) Measured SPR angles of graphene samples and calculated values with three different dielectric constants from M. Klintonberg et al., 2009, X. Wang et al, 2008, and Z. H. Ni et al., 2009 from the top of the left column.

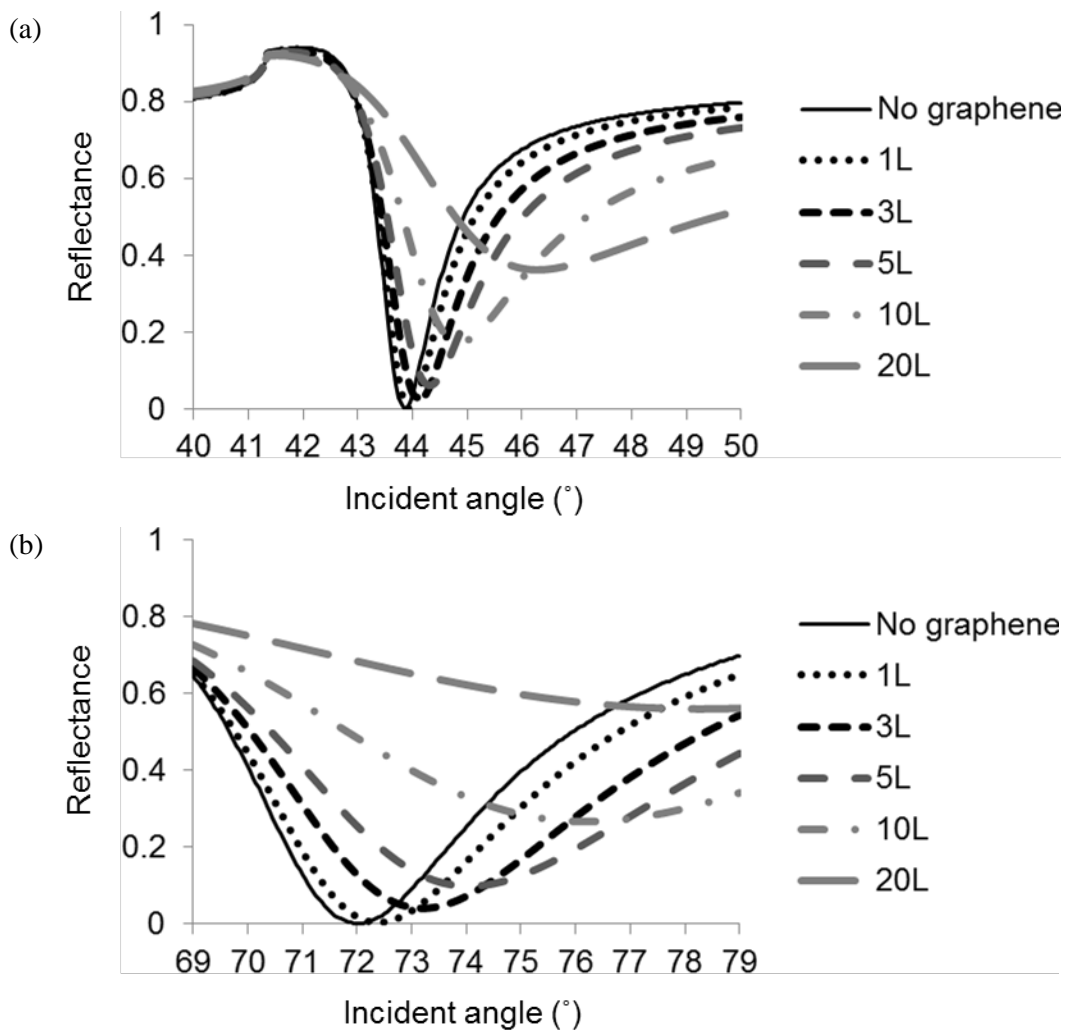


Figure 3.1 Calculation results for the SPR reflectance from graphene layers on SPRM for air (a) and water (b) on top of graphene. The SPR angle increase as the medium changes from air to water, and the SPR angle shift by the graphene layers also increase for the water medium.

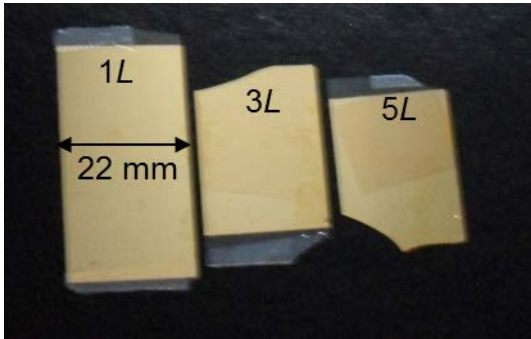


Figure 3.2 Graphene samples prepared on the SPRM substrates, i.e. 48-nm Au-coated slide glass. The graphene layers are synthesized by the conventional method: CVD on Cu foil and transfer by PMMA support (S. Bae et al., 2010).

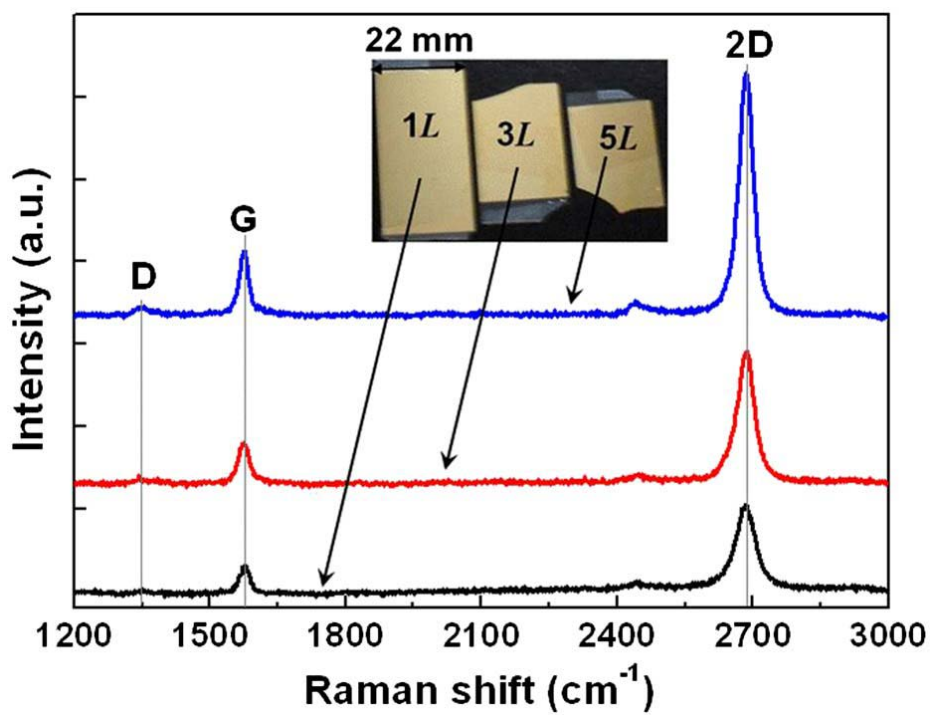


Figure 3.3 Raman spectra of 1, 3, and 5-layer graphene layers on gold film. The locations of the  $G$  ( $1590 \text{ cm}^{-1}$ ) and  $2D$  ( $2680 \text{ cm}^{-1}$ ) peaks of the SLG are marked with the two vertical lines.

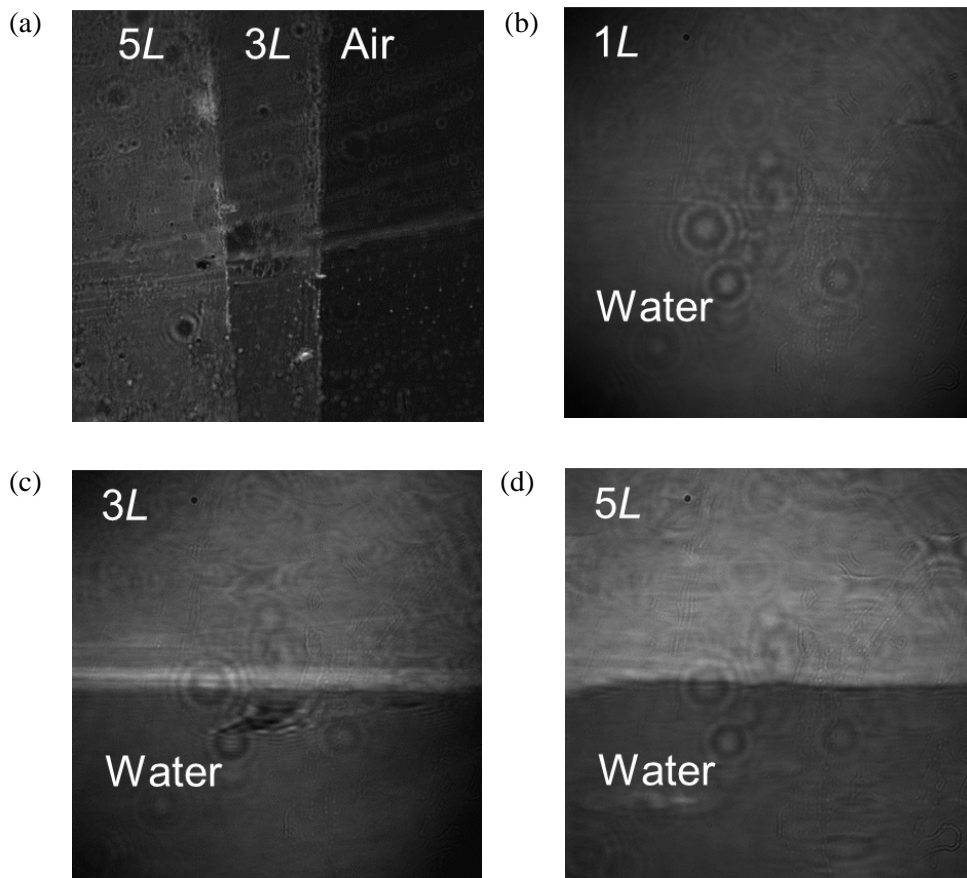


Figure 3.4 SPRM images of graphene samples. (a) 3L and 5L graphene layers for the air environment ( $\theta = \theta_{\text{SPR}} = 43.9^\circ$ ), (b)-(d) The SPRM images of samples in Figures 3.1 and 3.2.  $\theta = \theta_{\text{SPR}} = 72.1^\circ$ , the SPR angle for the water environment.

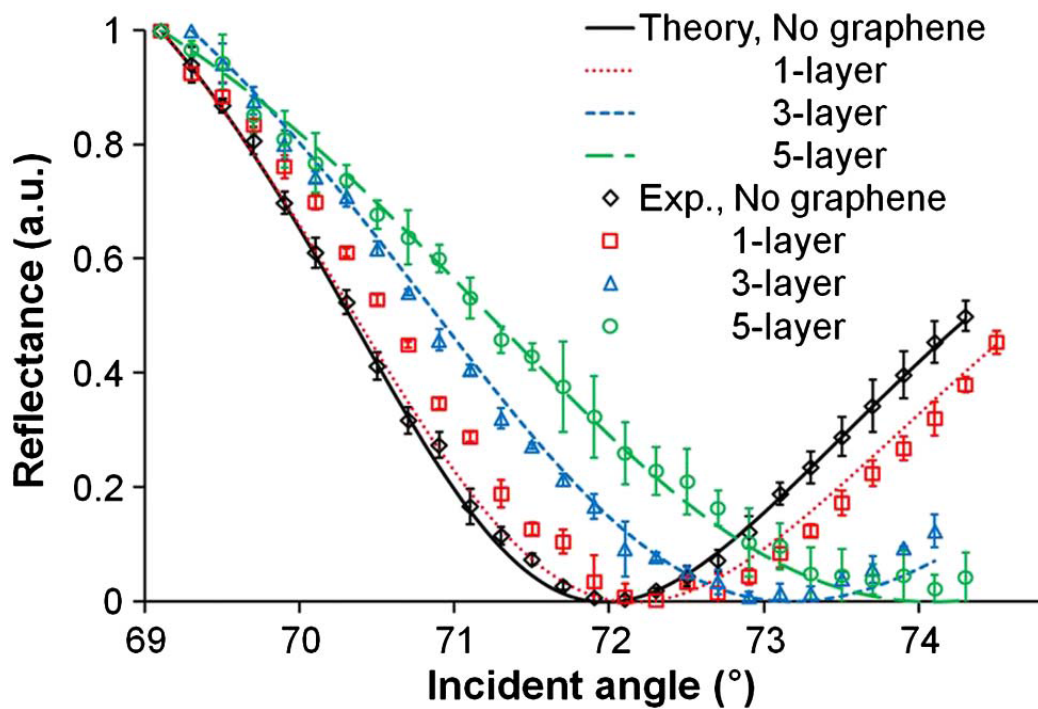


Figure 3.5 (Also in S. Cheon et al., 2012) Measured and calculated (equations (2.3), (2.4) and (2.5)) SPR reflectance variations with the incident angle for 1L, 3L, and 5L graphene on a 48 nm gold film (Figure 3.2).

## Chapter 4

### Complex RI of pristine CVD graphene

#### 4.1 Previous methods for graphene's RI measurements

As briefly mentioned in Chapter 1, there have been several efforts to measure the complex RI of graphene. Like many other materials, the graphene's complex RI value changes dramatically at specific wavelengths of light, that are far-infrared and ultraviolet (UV) regions from the theoretical prediction (M. Klintenberg et al., 2009). Thus, it is ideal to measure the RI of graphene at each and every wavelength in the range of interest, by the non-spectroscopic method. By the subsequent sections, the "spectroscopic" measurement refers to the method to determine the complex RI of graphene as a function of wavelength, using the dispersion modeling<sup>10</sup> of graphene.

##### 4.1.1 Non-spectroscopic methods

As a non-spectroscopic method, which does not require a dispersion modeling, picometrology (X. Wang et al., 2008) uses both the amplitude and phase change as two observables when light traverses the graphene edge, but the scheme bears several error sources creating uncertainties that are not quantitatively resolved. As another non-spectroscopic method, the polarization dependence of optical absorptions under the TIR condition was measured to determine the complex RI by fitting (Q. Ye, 2013); however, the uniqueness of the fitted real and imaginary parts of RI is somewhat questionable

---

<sup>10</sup> Dependency of a function to the wavelength, or equivalently, the energy of incident light.

because of the single constraint of the polarization dependence. For the case of a graphene flake oxide sample, fitting of the SPR curves (T. Xue et al., 2013) was attempted to determine the complex RI, but again further validation will be needed for the uniqueness of the fitted results because of too many fitting parameters for the single observable.

#### **4.1.2 Spectroscopic methods**

Notable efforts have been made by fitting experimental data from a single measurement technique to a dispersion model for RI of graphene, which is the spectroscopic method. The earlier use of reflection spectroscopy (Z. H. Ni et al., 2007) imposed an overly simplified assumption of both real and imaginary parts of the complex RI being constant over the visible range, whereas its later use (M. Bruna and S. Borini, 2009,) modeled the imaginary part of the complex RI using a constant optical conductivity based on the earlier report (R. R. Nair et al., 2008), yet retained an assumption of the real part of RI as a constant. Spectroscopic ellipsometry (V. G. Kravets et al., 2010; A. Matkovic et al., 2012; U. Wurstbauer et al., 2010; F. J. Nelson et al., 2010; J. W. Weber et al. 2010) uses a more elaborate model for the dispersion relation of the graphene RI, but the excessive number of fitting parameters may not ensure the uniqueness of the fitted RI values.

## **4.2 Tandem use of SPR and ATR for complex RI measurements**

### **4.2.1 Fundamental limitations of using a single measurement technique**

As listed in the sections 4.1.1 and 4.1.2, a lot of experimental methods have been applied to measure the RI of graphene, but the resultant values show significant scattering as listed in Table 4.1. Some of this scattering may be attributed to the graphene sample variations and different sample preparation processes, as well as to the possible

measurement uncertainties and bias associated with the different measurement techniques.

However, the more fundamental origins of the large data scattering of complex RI are considered to be two-fold: (1) the graphene RI is complex-valued, having two unknowns of both real and imaginary parts at a given wavelength, and (2) the ultra-thin graphene layers (less than 1 nm) cannot be sensitively characterized by observations based on optical far-field phenomena. To uniquely determine both the real and imaginary parts of graphene RI, therefore, two independent sets of measurement observables will be necessary, using two discrete measurement techniques for the same graphene sample. Furthermore, probing near-field characterization will enhance the measurement sensitivity (K. D. Kihm, 2011), since the surface-enhanced electromagnetic field exists enclosing the thin graphene layer.

#### **4.2.2 New method: simultaneously using both SPR and ATR**

As discussed in the previous section, two independent sets of measurement observables will be necessary for a single graphene's complex RI measurement. Furthermore, the SPR and the ATR, two near-field characterization techniques, will enhance the measurement sensitivity and guarantee the sensitive detection of the graphene layers, which will be described in Section 4.3.3.

In this work, I present the successful implementation of a reliable and robust way to determine the complex RI of graphene using two independent and non-spectroscopic measurement techniques: (1) detection of the SPR angle ( $\theta_{\text{SPR}}$ ) where the p-polarized light shows the maximum absorption by the SPPs in the thin Au layer so the reflectance becomes minimum, and (2) detection of the reflectance ratio of  $R_p/R_s$  at the critical angle when the incident light is attenuated by the graphene sample without an Au interlayer. The meaning of the two observables,  $\theta_{\text{SPR}}$  and  $R_p/R_s^*$  is depicted in Figure 4.1. These

two observables allow for the unique determination of the real and imaginary parts of the complex RI of graphene, as the way presented in Figure 4.2, and it is proven that the two observables are independent of each other, esp. for the measurements of pristine graphene (Section 4.3.3).

## 4.3 Results and analyses

The main layout of the experimental apparatus is the same as described in Section 2.2.2, but the substrate for the graphene samples is now coated “partially” by the Au layer of 48 nm, as in Figures 4.1-a and 4.1-b. The gold coated surface is used to measure  $\theta_{\text{SPR}}$  and the uncoated BK7 glass surface is used to determine the  $R_p/R_s^*$  (Figures 4.1-c and 4.1-d). Note that the water environment is provided for the graphene sample to enhance the angular measurement sensitivity by increasing the magnitude of the SPR angle ranges, in comparison to an air environment (Section 3.2.2).

### 4.3.1 3-D contour plots of two observables vs. complex RI of graphene

The demonstration of the method in Figure 4.2 can become clearer and accurate if the 3-D contour plots are introduced as in Figure 4.3. These plots are for the two observables (vertical axes) as functions of the complex RI values (horizontal plane), that should have the gradients proportional to the sensitivity of each observable to graphene’s RI. The plots are constructed by the numerous calculations for the reflection from the 4-layer structure for  $\theta_{\text{SPR}}$  and from the 3-layer structure for  $R_p/R_s^*$ , as already presented in Section 2.2.1 and the supplementary information of S. Cheon et al., 2014.

In addition to the graphical presentation, the 3-D contour plots can be used in determination and demonstration of important features of the measurement method: the uncertainties of the graphene RI measurements, comparison of the sensitivities of  $\theta_{\text{SPR}}$  for different graphene layer numbers, and orthogonality between the two observables, all

of which are explained in Section 4.3.3 in detail.

### 4.3.2 ATR reflectance of a single layer graphene

$R_p/R_s$ , the relevant observable from ATR for the graphene RI measurements (Figure 4.1-d), is measured for a SLG sample, and the result is given in Figure 4.4. When an absorbing layer such as graphene disjoins the water-prism (BK7 glass) interface, which is subjected to total internal reflection, the evanescent wave is partially attenuated and the resulting reflectance reduces from unity. Furthermore, the amount of reduction in reflectance is different for the p-polarized and the s-polarized incident light and the ratio of  $R_p/R_s$  is dependent upon the incident ray angle. The  $R_p/R_s$  at the critical angle is selected as a second independent observable to provide an additional constraint for the unique determination of  $(n_G, k_G)$ , and it is denoted as  $R_p/R_s^*$ . As expected, the measured value of maximum  $R_p/R_s^* = 1.124$  satisfies multiple pairs of  $(n_G, k_G)$  as shown in Figures 4.2-b and 4.3-b. Thus, the unique determination of complex RI is not possible by this constraint alone.

Even the data fitting of the full profile of the ATR reflectance curve cannot determine the complex RI of graphene uniquely, as elucidated in Figure 4.4 by the almost identical curves drawn by the calculations for the three different RI values of graphene. Even if one of the three curves is the “best fit” to the experimental data, it is not legitimate to determine the graphene RI value as that single value, since the experimental uncertainty overwhelms the differences in the data fitting process. Note that one of the previous papers (Ye et al., 2013) used this method and reported a graphene RI value with the imaginary part a little higher than the other references.

This also applies to the measurements and fitting of the SPR data as in Figure 4.5. It shows that all three curves generated with three different complex RI,  $(2.80+1.85i)$ ,  $(2.63+1.28i)$  or  $(2.58+0.70i)$  fit closely to the measured and  $\theta_{\text{SPR}}=72.97^\circ$ . Again, the  $n_G$ -

$k_G$  projection of the corresponding contour of measured  $\theta_{\text{SPR}}=72.97^\circ$  (Figures 4.2-a and 4.3-a) provides only a partial constraint that any of these pairs of  $(n_G, k_G)$  located on the projection band can be accepted for the fitting solution.

### 4.3.3 Results, data analysis, and discussions

Now, overlapping Figures 4.3-a and 4.3-b creates the intersection region that simultaneously satisfies both constraints of  $\theta_{\text{SPR}}$  and  $R_p/R_s^*$ , and therefore, the complex graphene RI is determined to be  $\text{RI}_G=2.63+1.28i$ , for the case of the  $3L$  graphene. Note that the area of the intersection region determines the final measurement uncertainties for  $(n_G, k_G)$ .

The resulting  $\text{RI}_G$  data are shown in Figure 4.6 as  $n_G+ik_G = 2.58+1.30i$ ,  $2.63+1.28i$ , and  $2.73+1.23i$  for  $1L$ ,  $3L$ , and  $5L$  graphene, respectively. The average of these three gives  $\text{RI}_G = 2.65+1.27i$  and the variations for different layer numbers ( $L$ ) remain within  $\pm 3\%$  from the average. The smaller uncertainty range for the higher  $L$  is attributed mainly to the higher RI sensitivity of  $\theta_{\text{SPR}}$  with increasing  $L$ , and this will be further elaborated in the next paragraphs. Calculations are also conducted to predict  $\text{RI}_G$  using the density function theory (DFT) and the result ( $\text{RI}_G = 2.71+1.41i$ ) is marked with the star symbol in Figure 4.6. In comparison with the published DFT results of  $2.96+1.49i$  for graphene ([12] in Figure 4.6) and  $2.88 + 1.50i$  for graphite ([12]† in Figure 4.6), the discrepancies are attributed to the minor differences of the calculation details such as the cutoff energy and the atomic potential modeling, while the dielectric functions agree well for the photon energy up to 20 eV.

Also presented in Figure 4.6 are published graphene RI data obtained from one of the single measurement techniques imposed with additional conditions and/or assumptions as described in the sections 4.1.1 and 4.1.2. These data are scattered for the

real part,  $2.0 < n_G < 3.2$  ( $\pm 23\%$  scattering), as well as for the imaginary part,  $0.78 < k_G < 1.6$  ( $\pm 34\%$  scattering). The two results from reflection spectroscopy ([2], [3] in Figure 4.6) show large deviations in their real parts of  $RI_G$  in particular. The former used a constant graphene RI model ([2] in Figure 4.6) that was later proven to be inappropriate ([4], [5], [7]-[9], [12] in Figure 4.6). The latter ([3] in Figure 4.6) used an incomplete dispersion model under the assumption of the universal optical conductance and assumed a constant of the real part of the graphene RI as  $n_G = 3$  for the best fit. Later, this was found to be inaccurate from the more up-to-date DFT analysis as well as from some experimental findings ([4], [5], [7], [10] in Figure 4.6). The deviation of the ellipsometry result ([6] in Figure 4.6) from those using a similar ellipsometry technique ([4], [5], [7], [8] in Figure 4.6) may be attributed to the simplified Drude model for graphene used for the data inversion, whereas the latter papers used the Cauchy model ([4] in Figure 4.6), Fano resonance model ([5] in Figure 4.6), point-to-point fitting/Lorentz oscillator model ([7] in Figure 4.6), and B-spline method ([8] in Figure 4.6), respectively.

Also, the discrepancies of some experimental results may be due to their uses of different samples other than pristine graphene layers, such as reduced graphene oxide (rGO) flakes ([11\*] in Figure 4.6) or highly oriented pyrolytic graphite (HOPG) ([15†] in Figure 4.6). Graphene oxide flakes are subjected to form segmented layers with impurities that can lead to reduction of electron mobility, and equivalently, reduced imaginary part of RI ( $k_G$ ). In contrast, the agility of electrons in the highest-grade HOPG can result in high optical conductivity and a noticeably large  $k_G$ .

The obtained RI values of graphene may contain the extrinsic effects from the contact of graphene with Au film, but it turns out that it is not the case. Contacts between graphene and a variety of metals were discussed by theoretically investigating the Fermi level shift in the contacted graphene from the freestanding one, and calculating the

electronic structure and electrostatic potential (Q. Ran et al., 2009). Their findings include that for the Au-graphene contact, there lies a potential barrier between them, which will cause extra contact resistance, resulting in only weak physical contact. Thus, we believe that graphene maintains weak physical contact with the gold substrate and that the opto-electric properties of graphene, including its complex RI, are not altered by the contacting Au substrate. Furthermore, we have found that a number of research groups have used different substrates contacting graphene, assuming no significant changes in graphene's RI properties for the case of amorphous quartz substrate (V. G. Kravets et al., 2010), GaAs substrate (U. Wurstbauer et al., 2010), poly-dimethylsiloxane (PDMS) (Q. Ye et al., 2013), and also for Au substrate (T. Xue et al., 2013).

The interactions between the single graphene layers could not affect the RI results for the  $3L$  and  $5L$  samples, judging from the previous reports. For AA-stacking of multilayer graphene, i.e., atom-to-atom arrangement of graphene layers, no measurable distinctions in RI were observed with the number of graphene layers (C. W. Chiu et al., 2013). For twisted bilayer graphene including AB-stacking (Y. Wang et al., 2010; J. Campos-Delgado et al., 2013), in contrast, the reflection contrast of multilayers was found to slightly vary with the existence of the 2nd graphene layer; however, more consistent and quantitative conclusions are still under examination. Note that these findings were relevant for mechanically exfoliated graphene layers from highly ordered pyrolytic graphite (HOPG), whereas the present study examined CVD-synthesized graphene layers that were created by the crystallized growth of many randomly oriented grains of which size ranges from sub-micron to few microns. Therefore, each layer of CVD-synthesized graphene is considered to be randomly oriented, and the multilayered graphene obtained by repeated transfer of each layer does not provide any consistent stacking orientations.

The increased total thickness of graphene with increasing  $L$  creates steeper contour surfaces above the  $n_G$ - $k_G$  plane (Figure 4.7), which in turn contributes to lowering the measurement uncertainties. The smaller error bars of the measured complex RI data with increasing  $L$ , as shown in Figure 4.6, are attributed to this enhanced sensitivity with increased total thickness of the graphene samples.

The multi-layered graphene samples are prepared by physical stacking of multiple CVD-synthesized layers, one at a time, through multi-step processing such as spin coating, baking, and etching of PMMA and use of chemicals (X. Li et al., 2009), so extra care must be taken to minimize left-over impurities and contaminants. In addition, the Raman signal can provide quite reliable information on imperfections, disorders, and grain boundaries on graphene, but the PMMA residues are not detectable by Raman signal since they are Raman inactive (W. Xu et al., 2012).

It is worthwhile noting that I can rule out the possibility of the PMMA residues might have deteriorated the measured RI values of graphene by our SPR results themselves. If there were the PMMA residues that can affect the results, the SPR measurements should have readily overestimated the  $n_G$  since the SPR is known as the most sensitive detection tool for the real component of RI (I. M. White and X. Fan, 2008). However, the value of  $n_G$  in our result is not larger than the previous results, so it seems that the PMMA residue is negligible, if it exists.

Independence of the two observables,  $\theta_{\text{SPR}}$  for minimum SPR reflectance and the  $R_p/R_s^*$  for attenuated total internal reflection, can be assessed by their mutual orthogonality on the  $n_G$ - $k_G$  plane (Figure 4.8), which is defined as a sine function of the intersection angle of the two projected contour bands. Thus, the orthogonality of near unity of the present cases of  $1L$ ,  $3L$ , or  $5L$  support fairly unique determinations of the graphene RI within acceptable experimental uncertainties. Also, the fitting uncertainties

for both SPR angles and total reflectance ratios associated with FWHM of 22 nm are shown to be less than 0.3% deviations from those with zero FWHM (Figure 4.9), based on the reflection calculations presented in Section 3.2.1.

The DFT calculations for complex graphene RI used the Vienna Ab-initio Simulation Package (VASP) to determine the dielectric constants for both the in-plane ( $xx$ ) and cross-plane ( $zz$ ) directions (Figure 4.10). Then, the complex RI value of graphene can be readily obtained by taking a square root of a complex dielectric constant at a specific energy (equivalently, wavelength<sup>-1</sup>). The charge density distributions were first calculated for use in the electronic band structure and dielectric function calculations. In calculating the charge distributions, graphene is set to have a constant interatomic distance of 1.42 Å and the tetrahedron method with Blöchl corrections was used for partial occupancy with broadening of 0.1 eV. The projector-augmented wave (PAW) method was adopted with ultra-soft pseudo-potentials and energy cutoff of 400 eV. The K-point grid was generated by automatic generation of C-centered  $36 \times 36 \times 12$  mesh and the electronic band structures were calculated with Gaussian smearing along the high symmetry points of the irreducible Brillouin zone of graphene, C-M-K-C, with 20 segments in each line. The present result shown by the star symbol in Figure 4.6 comes from consideration of the dielectric constant at 1.96 eV, which corresponds to the center wavelength of 634 nm of the LED light that was used for the experiment.

Table 4.1 (Also in S. Cheon et al., 2014) Measured and calculated complex RI values of various graphene and graphite samples reported in previous articles. Note that the superscript numbers in the “Reference” column coincide with those in Figure 4.6.

Reference	Method	Descriptions	$(n_G, k_G)$	Note	Sample
Present work	SPR and ATR measurements	Measurements of $\theta_{\text{SPR}}$ and $R_p/R_s$ and simultaneous matching with calculation results	$(2.58 \pm 0.38, 1.3 \pm 0.25)$	Uncertainties from statistical analyses for three SPR data	CVD, 1L
			$(2.63 \pm 0.20, 1.28 \pm 0.10)$		CVD, 3L
			$(2.63 \pm 0.20, 1.28 \pm 0.10)$		CVD, 5L
Ni et al. (2007) <sup>2</sup>	DFT	First principles calculation by full potential linear muffin-tin orbital (FP-LMTO) within local density approximation (LDA) and generalized gradient approximation (GGA)	$(2.71, 1.41)$	Oscillatory behavior similar to that in Ref. [10]	Graphene (2 carbon atoms in a unit cell)
	Reflection spectroscopy	Reflected light from a graphene sample by a spectrometer (illumination: white).	$(2.0, 1.2)$	Assumed that $n_G$ and $k_G$ are $\lambda$ -independent.	Exfoliation, 1L

Bruna & Borini (2009) <sup>3</sup>	Reflection spectroscopy	Same as above, but the experimental data are from (R. R. Nair et al., 2008)	(3.0, 1.15)	Modeling: $k_G = 5.446 \mu\text{m}^{-1} \frac{\lambda}{n_G}$ and fitted only for $n_G$ .	Exfoliation, 1L~2L
Kravets et al. (2010) <sup>4</sup> , Matkovic et al. (2012) <sup>5</sup> , Wurstbauer et al. (2010) <sup>6</sup>	Spectroscopic ellipsometry	Polarization state change of light beam of tunable wavelength, when reflected at the graphene with oblique incidence	(2.8, 1.45) (2.7, 1.35) (3.0, 1.35) (2.3, 0.8)	Needs a dispersion modeling with 4 or more fitting parameters.	Exfoliation, 1L
Jellison et al. (2007) <sup>15</sup>	Spectroscopic ellipsometry	Same as above.	(2.56, 2.03)	Measurements with several wavelengths	HOPG (highly oriented pyrolytic graphite), ZYA (highest) grade after tape cleavage
Ye et al. (2013) <sup>8</sup>	Polarization-dependent ATR	Attenuated total internal reflection of monochromatic, p- and s-polarized light at air/graphene/prism with changing incident angle	(2.6, 1.6)	Determination of unique $n_G$ and $k_G$ will be challenging.	CVD, 1L~2L
Xue et al. (2013) <sup>9</sup>	SPR	Reflectance of monochromatic and p-	(2.75, 0.41)	Used graphene oxide	Reduced samples graphene oxide

		polarized light from water/graphene/Au/Cr/glass with changing incident angle		with 6 fitting laid on an parameters to be Au/Cr/glass determined. substrate
Wang et al. (2008) <sup>7</sup>	Picometrology	Amplitude and phase change of reflected light when a focused monochromatic light traverses a graphene boundary.	(2.95, 1.32) (2.98, 1.44)	Beam profile other than Gaussian and slight defocusing should be noted. Exfoliation, 1L
Klintonberg et al. (2009) <sup>12</sup>	Density functional theory (DFT)	Same as present work (DFT)	(2.96, 1.49)	Oscillatory behavior of the Graphene dielectric functions for the visible wavelengths (2 carbon atoms in a unit cell)
Klintonberg et al. (2009) <sup>12†</sup>	DFT	Same as above.	(2.88, 1.50)	Graphite

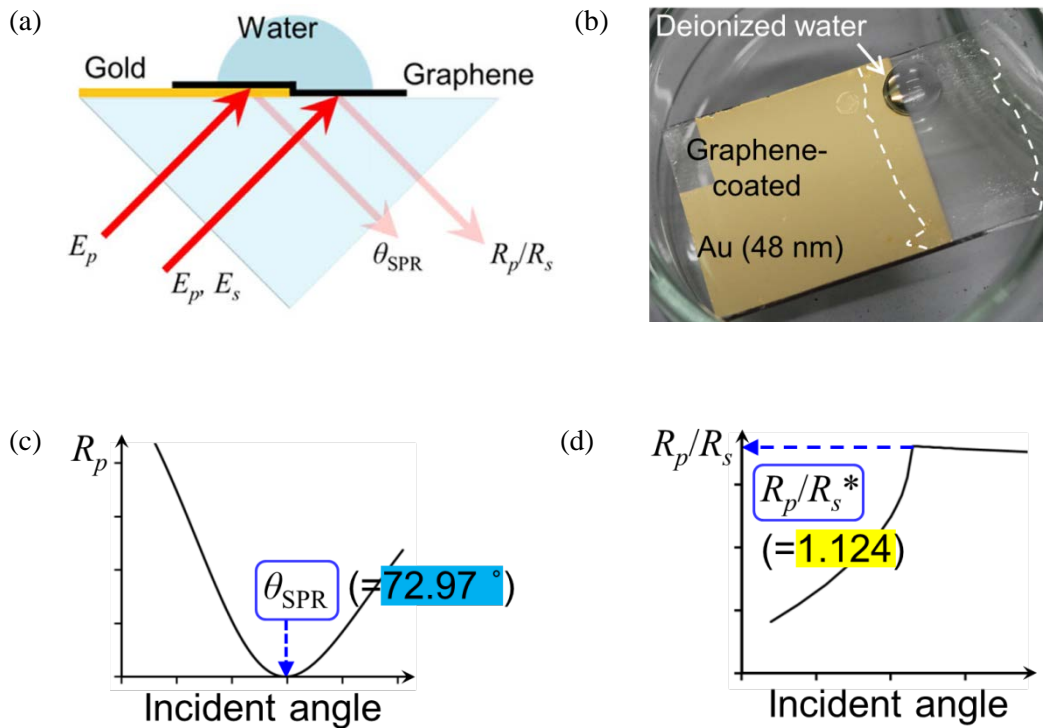


Figure 4.1 (Also in S. Cheon et al., 2014) Experimental layout, a graphene sample's photo, and two relevant observables for the complex RI measurements of graphene. (a) Schematic of the two tandem measurements for  $\theta_{SPR}$  and  $R_p/R_s$  under a deionized water environment (in lieu of air) for enhanced measurement sensitivities and (b) a graphene sample laid on a BK7 glass substrate that is partially coated with 48-nm thick Au film. (d)  $\theta_{SPR}=72.97^\circ$  is measured from the maximum resonant absorption of SPPs, or equivalently as the minimum reflectance of the p-polarized incident ray (634 nm wavelength, 3L graphene), (e) the maximum is  $R_p/R_s = 1.124$  measured at the critical angle for total internal reflection (634 nm wavelength, 1L graphene).

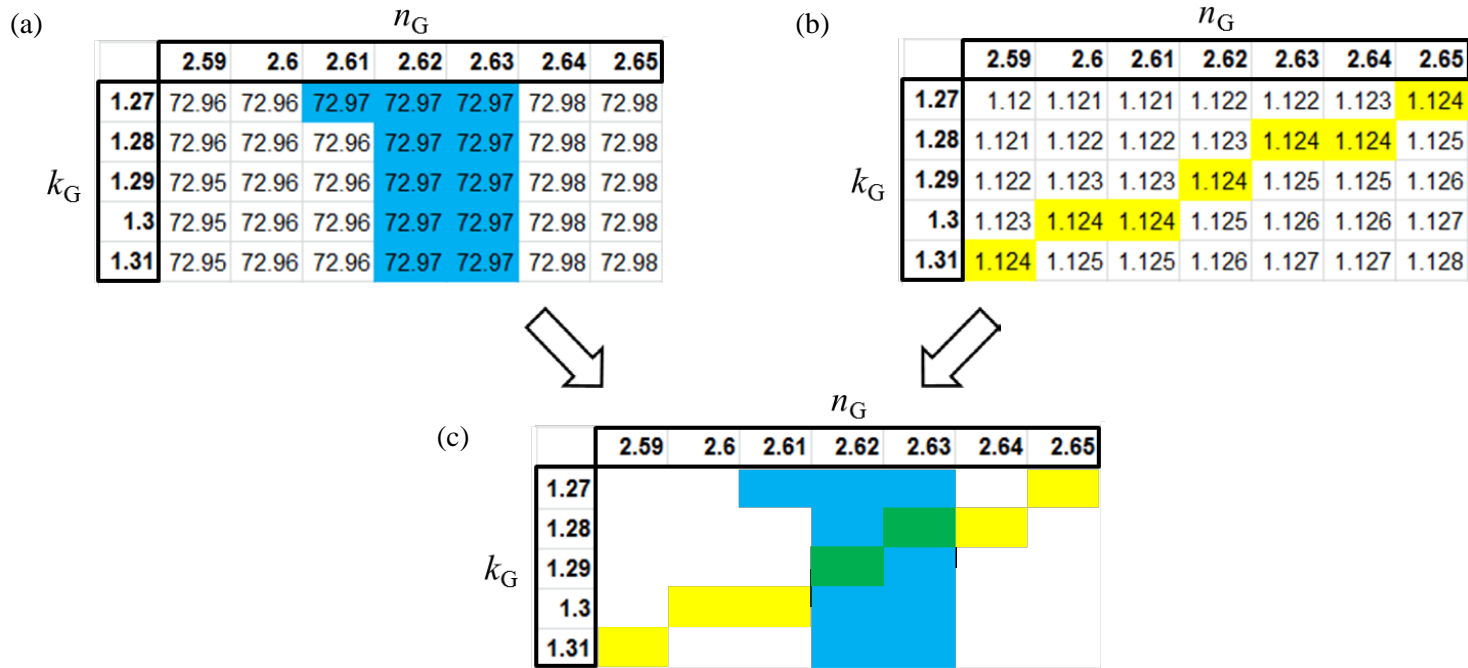


Figure 4.2 (Also in S. Cheon et al., 2014) Method for the determination of the complex RI of graphene by the two observables. (a) All possible fitting solutions of  $(n_G, k_G)$  that satisfy the first constraint of  $\theta_{\text{SPR}}=72.97^\circ$ , (b) all possible fitting solutions of  $(n_G, k_G)$  that satisfy the second constraint of maximum  $R_p/R_s=1.124$ , and (c) determination of the unique complex RI of graphene,  $\text{RI}_G = (n_G, k_G) = 2.63+1.28i$  from the intersection of (a) and (b), two black cells, which simultaneously satisfies the two constraints.

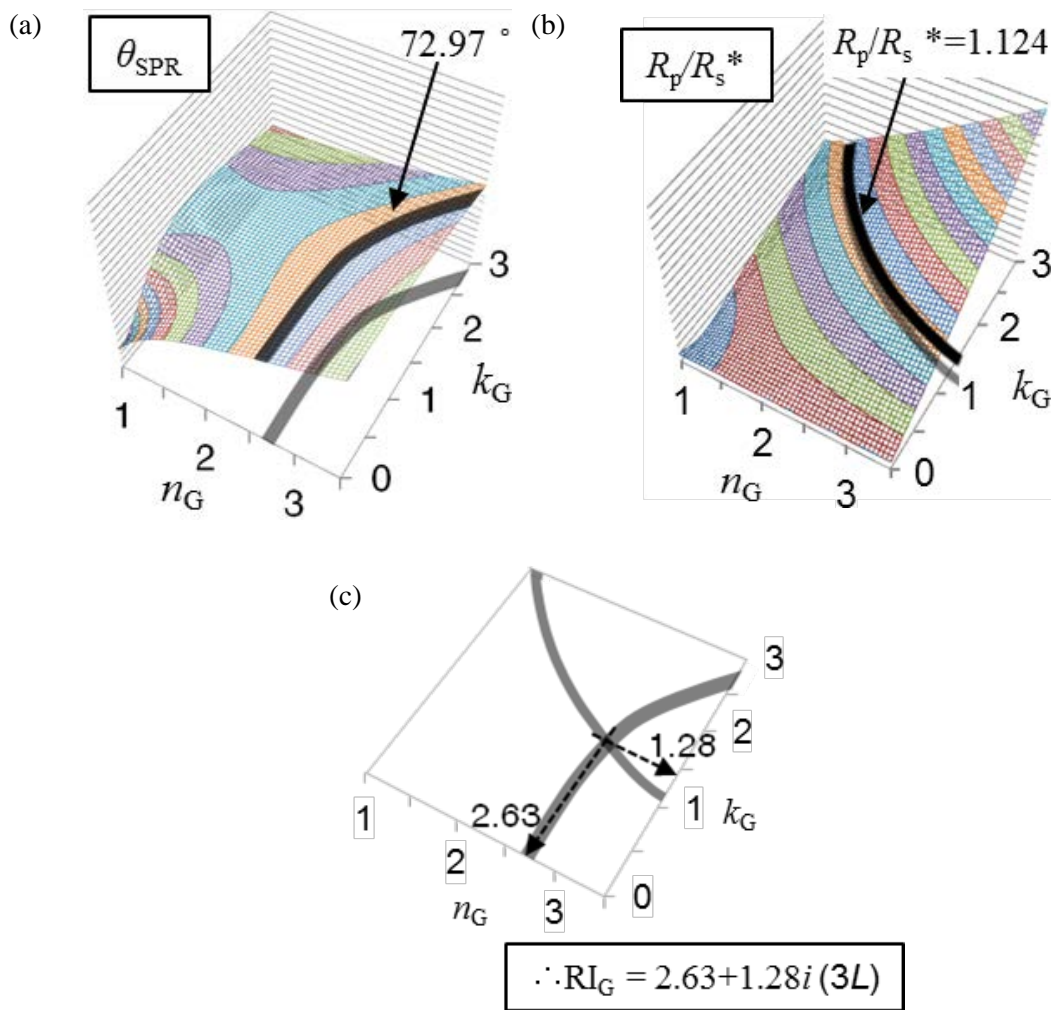


Figure 4.3 Graphical presentation of the new graphene RI measurement method by the 3-D contour plots. The concept is exactly the same as that of Figure 4.2.

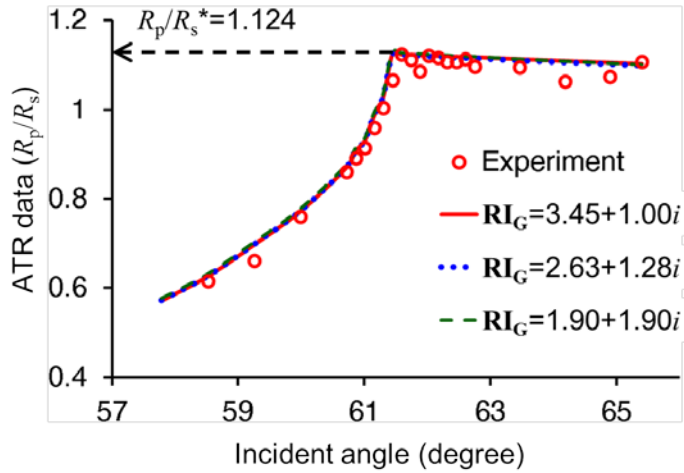


Figure 4.4 (Also in S. Cheon et al., 2014) The measured ATR  $R_p/R_s$  as changing the incident angle with the fitting curves calculated with three different RI values of graphene. The value at the critical angle of TIR is named as  $R_p/R_s^*$  and used to measure the complex RI of graphene. Note that the three arbitrarily selected pairs of  $(n_G, k_G)$  among the solution candidates predict an identical  $R_p/R_s$  curve from the and all of them fit to the experimental  $R_p/R_s$  data, which demonstrates the difficulty in uniquely determining the complex RI of graphene using the  $R_p/R_s$  data alone.

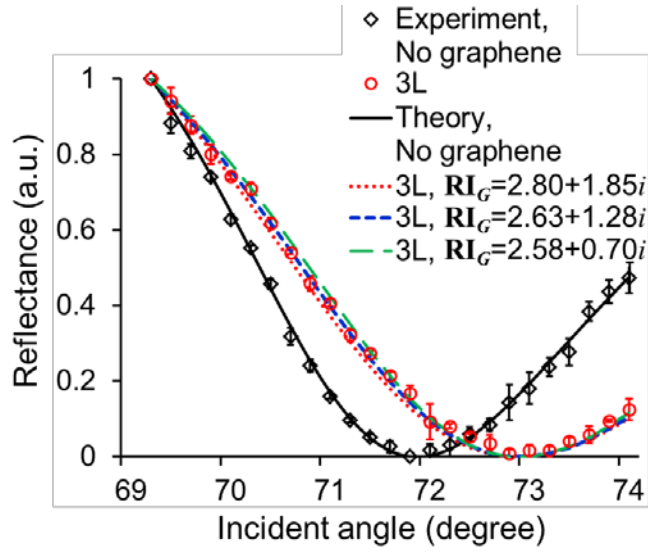
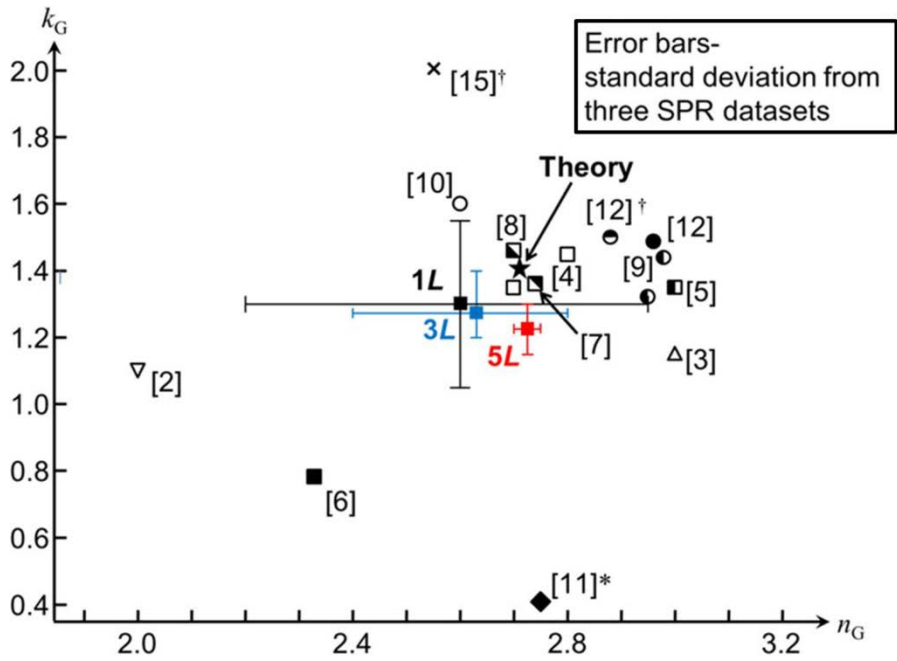


Figure 4.5 (Also in S. Cheon et al., 2014) Uncertainties associated with the single constraint of  $\theta_{\text{SPR}}$  data. Three arbitrarily selected pairs of  $(n_G, k_G)$  among the solution candidates in  $n_G$ - $k_G$  plane in the Figure 4.3-a predict an identical surface plasmon reflectance curve, thereby an identical  $\theta_{\text{SPR}}$ , and all of them fit to the experimental  $\theta_{\text{SPR}}$  data, which demonstrates the difficulty in uniquely determining the complex RI of graphene using  $\theta_{\text{SPR}}$  data alone.



	$L=1$	3	5
SPR angle (degree)	$72.23 \pm 0.06$	$72.97 \pm 0.12$	$73.87 \pm 0.07$
ATR ratio ( $R_p/R_s$ )	$1.124 \pm 0.010$	-	-
$n_G$	$2.58 \pm 0.38$	$2.63 \pm 0.20$	$2.73 \pm 0.03$
$k_G$	$1.3 \pm 0.25$	$1.28 \pm 0.10$	$1.23 \pm 0.08$

Figure 4.6 (Also in S. Cheon et al., 2014) Measured and predicted  $RI_G$  in comparison with other published results<sup>11</sup>. The three measured  $RI_G$  data respectively for  $1L$ ,  $3L$ , and  $5L$  graphene samples show deviations of a mere  $\pm 3\%$  from the averaged  $RI_G = 2.65 + 1.27i$ . The extent of the error bars decreases with increasing  $L$ , primarily because of the enhanced measurement sensitivities of  $\theta_{SPR}$  with thicker graphene samples while the measurement uncertainty for  $R_p/R_s$  remains unchanged. The predicted result of  $RI_G = 2.71 + 1.41i$  (★) using DFT agrees fairly well with all of the measured  $RI_G$  data.  $RI_G$  data from previous efforts include the reflection spectroscopy [2, 3], the spectroscopic ellipsometry for graphene [4–6] and for HOPG [15]†, more recent ellipsometry that alleviate the need of dispersion modeling [7, 8], the picometrology [9], absorption under internal reflection [10], surface plasmon reflectance for reduced graphene oxide (rGO) [11]\*, DFT calculations for graphene [12] and for graphite [12]†. More detailed descriptions on these published data are shown in Table 4.1, and further elaboration on their uncertainties is presented in the main text. (†: Results for graphite samples; \*: Results for reduced graphene oxide sample; All other data: Results for CVD-synthesized or exfoliated graphene samples).

---

<sup>11</sup> [2] Z. H. Ni et al., 2007; [3] M. Bruna and S. Borini, 2009; [4] V. G. Kravets et al., 2010; [5] A. Matkovic et al., 2012; [6] U. Wurstbauer et al., 2010; [7] F. J. Nelson et al., 2010; [8] J. W. Weber et al., 2010; [9] X. Wang et al., 2008; [10] Q. Ye et al., 2013; [11] T. Xue et al., 2013 [12] M. Klintonberg et al., 2009; [15] G. E. Jellison Jr. et al., 2007.

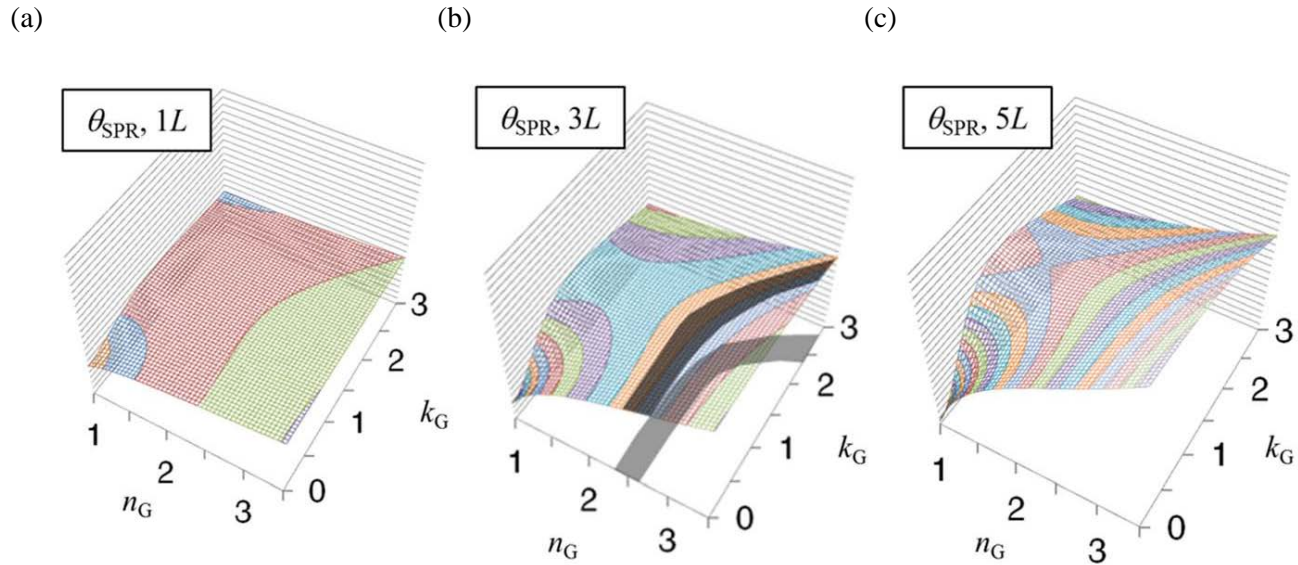


Figure 4.7 (Also in S. Cheon et al., 2014) Measurement sensitivity of  $\theta_{\text{SPR}}$  vs. the uncertainties of  $(n_G, k_G)$ . The predicted  $\theta_{\text{SPR}}$  contours with consistent  $0.2^\circ$  increments are shown for  $1L$ ,  $3L$ , and  $5L$  graphene, and the slope of the contours above the  $(n_G, k_G)$  plane increases with increasing  $L$ . This implies that, given a fixed measurement sensitivity of  $60.1^\circ$  for  $\theta_{\text{SPR}}$ , the corresponding uncertainties in determining  $(n_G, k_G)$  are reduced with increasing  $L$ .

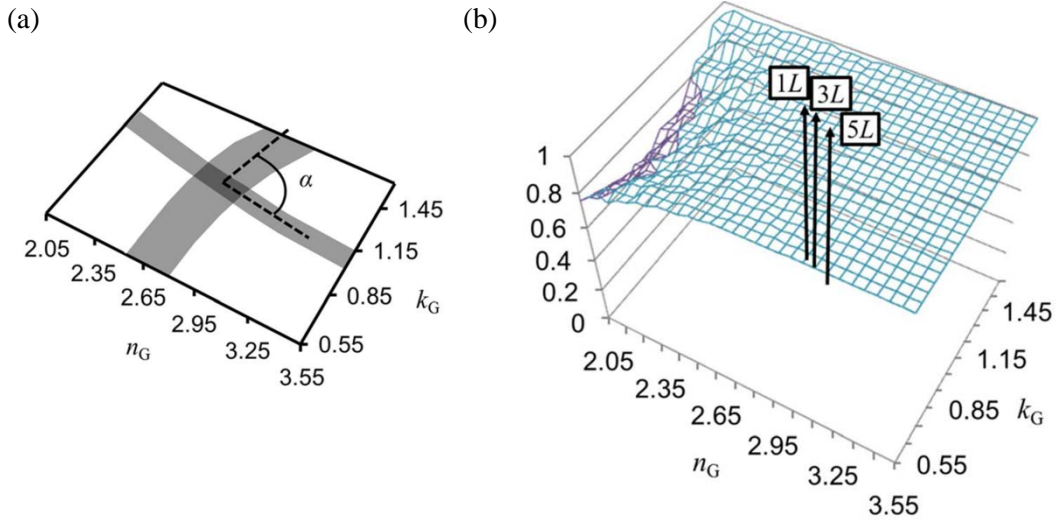


Figure 4.8 (Also in S. Cheon et al., 2014) Orthogonality of the two independent observables,  $\theta_{\text{SPR}}$  and  $R_p/R_s^*$ . (a) The orthogonality of the two sets of solution pairs ( $n_G$ ,  $k_G$ ) from the two constraints,  $\theta_{\text{SPR}}$  and  $R_p/R_s^*$ , is defined as the sine function of their intersection angle  $\alpha$  on the projected plane, and (b) the maximum orthogonality of unity for  $\alpha=90^\circ$  provides the strong independence of the two constraints ensuring the unique determination of the complex RI of graphene. All of the three measured RI values for the 1L, 3L, and 5L fall on the desirable maximum orthogonality of unity.

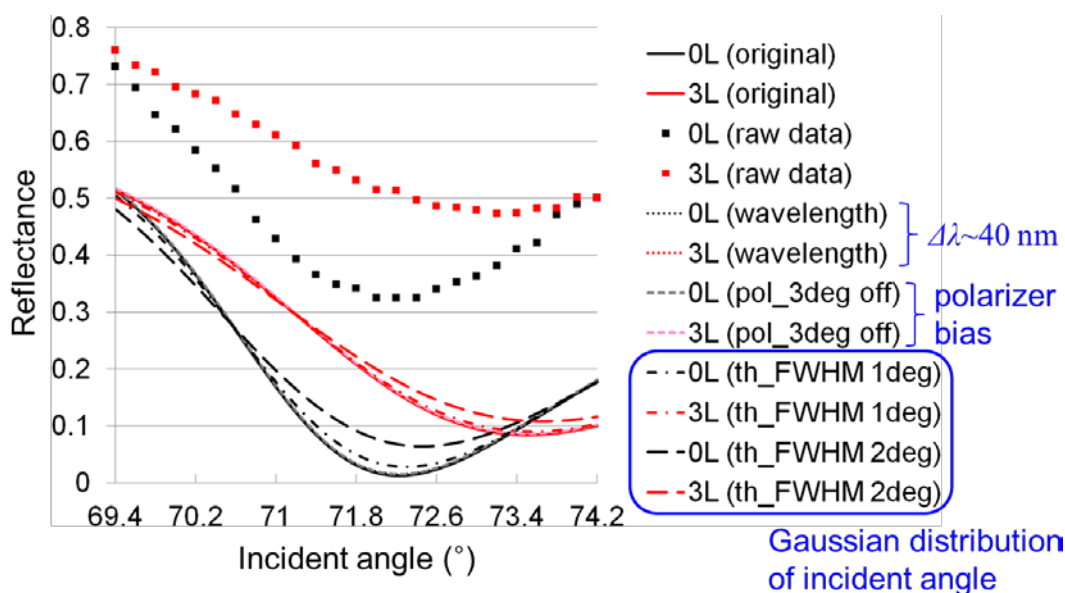


Figure 4.9 Dependencies of the SPR reflectance curves onto different systematic uncertainties, wavelength dispersion of 40 nm, polarizer's offset of 3°, and the Gaussian distribution of the incident angle, calculated based on the formula in Section 3.2.1. Note that the change due to the wavelength dispersion is so small that the dotted curves cannot be seen. The other two variables broaden the SPR curves, especially the distribution of the incident angle by the imperfect collimation of the incident light. The closed squares are for the (not normalized) raw data of the SPR measurements, which are elevated compared with the calculation results due to the uncontrollable experimental variables.

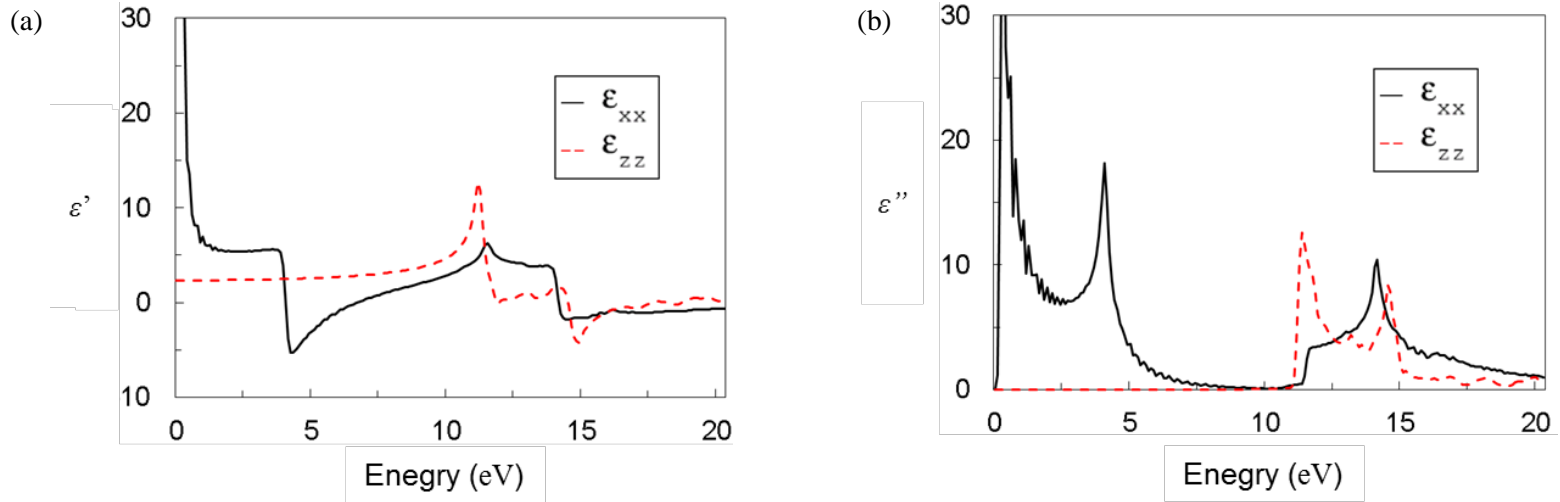


Figure 4.10 (Also in S. Cheon et al., 2014) Ab-initio calculation results for the complex dielectric function of graphene. The real (a) and imaginary (b) parts of the complex dielectric function of pristine graphene are calculated using DFT. The dielectric function  $\epsilon_{xx}$  is for the electric field oscillating parallel to the graphene layer and  $\epsilon_{zz}$  is for the electric field perpendicular to the graphene layer. Note that our proposed scheme, like all other available experimental methods, is able to conduct measurements only for the  $xx$ -components of the complex RI where the electric field oscillates in parallel with the graphene layer and is unable to detect the  $zz$  components. For the incident wave of 634 nm corresponding to 1.96 eV, the real and imaginary parts of the relevant dielectric function are given by  $\epsilon_{xx}=5.36+7.64i$  and the resulting complex RI of graphene is given by  $\sqrt{\epsilon_{xx}} = n_G+ik_G=2.71+1.41i$ .

## **Chapter 5. Complex RI of N-doped CVD graphene**

### **5.1 Background of N-doped graphene (NdG) study**

In Chapter 1, the overview was given that the nitrogen doping on graphene will change the electrical properties of graphene significantly, inducing the optical properties change due to the Fermi level shift and the electronic band structure modification. In the following sections, the previous studies on the NdG fabrication, theoretical and experimental reports on the RI of NdG are introduced.

#### **5.1.1 Synthesis and transfer of NdG**

Among the various methods to obtain the NdG, CVD (D. Wei et al., 2009; Z. Jin et al., 2011) is by far the most reliable method for the large-area samples with controllable properties. D. Wei et al. used a 25 nm thick of Cu film on a Si substrate and Z. Jin et al. used a Cu foil of 25  $\mu\text{m}$  thickness and 99.9999% purity as the catalyst. The substrate was placed in a quartz tube in a heater with a flow of hydrogen, argon,  $\text{CH}_4$  and  $\text{NH}_3$  (or pyridine), and then the temperature was raised up to 1000  $^\circ\text{C}$ . The detailed parameters for processes were different, but they synthesized NdG, whether multi-layer (D. Wei et al., 2009) or single-layer (Z. Jin et al., 2011). The characterization tools used were scanning electron microscopy (SEM), transmission electron microscopy (TEM), X-ray photoelectron spectroscopy (XPS), X-ray energy dispersive spectrometer (EDS) and Raman spectroscopy.

It is shown in (Z. Jin et al., 2011) that the same transfer process as applied for the pristine graphene (S. Bae et al., 2010) can be used for the transfer of NdG, without a major modification.

### **5.1.2 Density functional theory (DFT) for complex RI of NdG**

The calculations based on the electron density functionals, DFT, can offer the variety of properties of materials, including the graphene layers with atomic doping as reported in two references (P. Nath et al., 2014; P. Rani et al., 2014). They calculated the atomic structure, electronic band structure, and finally the optical properties of doped graphene layers, similar to the calculation for the pristine graphene in (M. Klintonberg et al., 2009) and section 4.3.3 in this thesis.

The results for the two papers are shown in Figures 5.1, 5.2, and 5.3, where the two groups reported quite different results for the change of the optical properties by nitrogen doping from the pristine graphene. Figure 5.1 and Figure 5.2 (P. Nath et al., 2014) show the calculated reflectivity functions and electron energy loss spectra (EELS) of the NdGs, implicitly corresponding to  $n_{\text{NdG}}$  and  $k_{\text{NdG}}$ , respectively. P. Rani et al. reported the imaginary part of the dielectric functions only (Figure 5.3), which is the function roughly proportional to the EELS function and the  $k_{\text{NdG}}$ . Comparing the results from the two groups, Figures 5.2 and 5.3, it is clear that the two calculation methods yielded the different optical properties of NdG, since the EELS function and the imaginary part of the dielectric function should be almost proportional to each other. This can be attributed to the detailed calculation scheme, including the cutoff energy, the atomic potential modeling, and the grid systems for the momentum space.

This discrepancy leads to the necessity of the more accurate calculations for the NdG's optical properties, which is done in this study (5.3.1). In the previous and current

studies, the theoretical results show that the difference of the complex RI of NdG and that of pristine graphene may be prominent at narrow and specific spectral ranges, so the experimental measurements should be done in multiple wavelengths in order to fully discover the optical characteristics of NdG.

### 5.1.3 Limitations of SPR for RI measurements of NdG

The complex RI measurement method presented in Chapter 4 can be applied to any materials at the incident wavelength of 634 nm, because the sensitivities of the SPR (Figure 4.3-a) and ATR (Figure 4.3-b), and the orthogonality between them (Figure 4.8-b) are high enough for the wide range of  $(n, k)$ . However, the method is optimized for the single wavelength (634 nm) only, so the validation is necessary to check whether it can be used to measure the NdG's RI at the wide range of spectrum, since the spectroscopic inspection will be essential as argued in the previous section.

As shown in Figure 5.4-a, the original setup used for the pristine graphene samples, 48 nm thick Au, turns out not to bear the distinctive SPR dips when the incident wavelength is 550 nm or 450 nm. Thus, the modified experimental setup is considered, where the thickness of the Au layer is reduced down to 20 nm. The thinner Au layer seems to show the SPR dips for all the three wavelengths, but they are not as sharp as the one for the 48 nm thick Au film.

The feasibility study results are given in Figures 5.5, 5.6, 5.7, and 5.8, on the sensitivity of the SPR angle and the orthogonality of  $\theta_{\text{SPR}}$  and  $R_p/R_s^*$ , for the two wavelengths of incidence. The RI value of the NdG layer will be at somewhere in the horizontal plane of complex RI,  $(n_G, k_G)$ , so the ideal situation is that the gradients in Figures 5.5 and 5.7 are large enough, as in Figure 4.7-b and the orthogonality is near unity for all the  $(n_G, k_G)$  range.

Unfortunately, the calculation results inform that both the original setup (48 nm Au), and the modified one (20 nm Au) are not able to accurately measure the complex RI of the graphitic thin layer samples at the wavelength of 450 nm, due to the poor RI sensitivity of  $\theta_{\text{SPR}}$  or the small orthogonality between the two observables,  $\theta_{\text{SPR}}$  and  $R_p/R_s^*$ . This means that for the shorter wavelengths, the combination of the two observables is not as sensitive to the complex RI as the 634 nm wavelength used in the pristine graphene RI measurements.

Therefore, it is proven that the original method of the tandem use of the SPR and ATR measurements are no more useful for the multi-wavelength measurements of the NdG samples. From the next sections, the spectroscopic ellipsometry will be used to measure the complex RI of NdG in the wide range of the wavelength of the incident light.

## 5.2 Spectroscopic ellipsometry (SE) for accurate NdG measurements

There already exist reports on the graphene's RI measurements with spectroscopic ellipsometry (SE) (V. G. Kravets et al., 2010; A. Matkovic et al., 2012; U. Wurstbauer et al., 2010; F. J. Nelson et al., 2010; J. W. Weber et al. 2010). They used different kinds of sample preparation, measurements, and data analyses methods, and the results are different from one another (Figure 4.6, [4-8]). Thus, the determination of the proper substrate, sample preparation and data analysis method is critical to obtain the RI change in graphene induced by the atomic doping of the nitrogen.

### 5.2.1 Choice of a substrate

The first choice for the substrate is the PDMS (poly-dimethyl-siloxane), which is transparent as well as hydrophobic. The purpose of choosing this material is to enhance the signal to noise ratio by the transparency (V. G. Kravets et al., 2010), while minimizing the adsorption of the water layer on the graphene, which will complicate the data fitting process and increase the uncertainty of the final results.

However, it turns out that the transparency becomes a source of large data noise in the normal operation of ellipsometry measurements (Figure 5.9). This is because the measurements cannot correctly acquire the data  $\Delta$  (R. M. A. Azzam and N. M. Bashara, 1977) around  $0^\circ$ , i.e.  $-0.1^\circ$  is read as  $179.9^\circ$  and this introduces large noise in data. In addition, though the PDMS substrates are made on the flat wafers of roughness of about 1 nm, the roughness can increase while curing and detaching the PDMS substrates from the wafers. This small roughness should not be a major problem in many experiments, but the ellipsometry is very sensitive technique to the surface roughness, so it can be another error source for the RI measurements of graphene.

Therefore, the silicon wafer without any intentional oxide layer is used as the substrate for graphene RI measurements by SE. The merit of using this as the substrate is two-fold: it has the small roughness for reduction of noise, and it doesn't need a complicated multi-layer modeling for the substrate. Indeed, the SE results for silicon substrates matches well with the reference RI function of silicon, with small corrections due to the thin native oxide and PMMA residues as described in the following section.

### 5.2.2 Methods to extract complex RI from raw SE data

In order to obtain the RI of graphene without large error, SE data from the substrate are obtained first, followed by the observation of the difference of the data when there is a graphene layer. For this, the SE data from all substrates are first investigated, where the beam for the SE measurements illuminating 5 points just outside of the graphene boundary. From this step, the effects from the sample to sample variations of the substrates for different graphene samples are excluded, including the thickness of the native oxide layer and the minute amount of PMMA residues that may exist.

The data fitting for the substrates are done with the “effective substrate” modeling, instead of the multilayer modeling with native SiO<sub>2</sub>, the PMMA residue, and water if exists. This simplified modeling is based on the analysis by the ellipsometry software provided by Ellipso Technology® that the total thickness of native SiO<sub>2</sub> and PMMA residue layers is thinner than 2.8 nm. In addition, in a previous work, (A. Matkovic et al., 2012) it has been observed that the stacking order of thin dielectric layers around graphene in the model has negligible effect on the SE data.

In our model for substrates, the effects from thin native oxide and the PMMA residues are realized by the pseudo RI of the optically thick effective substrate, which is naturally different from the RI of pure silicon. The pseudo RI is determined by fitting the raw data of SE ( $\alpha$ ,  $\beta$ ) with the calculated ( $\alpha$ ,  $\beta$ ) signals from the effective substrate, where the calculation is conducted by the open source program RefFIT (<http://optics.unige.ch/alexey/refit.html>). The best fit results (Figure 5.10) has the data fitting errors  $\chi^2$  smaller than 300, where the weights for  $\alpha$  and  $\beta$  are set to be 2.4 and 1 respectively, for the similar errors for the two fittings.

On the effective substrate in the data fitting model, the graphene layer of thickness 0.335 nm is introduced for fitting of the SE data from the graphene regions, where graphene follows the Fano-shaped Lorentz oscillator model (A. Matkovic et al., 2012). This model can describe graphene's optical properties well, with asymmetric line shape due to scattering within a continuum of states (the background process) and a discrete state (the resonant process).

## 5.3 Results and analyses

### 5.3.1 Optical properties of NdG and pristine graphene: DFT study

The optical properties, i.e. the RI of NdG are calculated by using DFT (Figure 5.11), where the change in RI is most prominent for the wavelengths between 333 nm (blue) and 500 nm (green) light. The detailed calculation steps, assumptions, grid systems, and atomic potentials, are all the same with those described in 4.3.3, except the substitution of one carbon atom in 24 or 54 carbon atoms in a unit cell, for 4.17 and 1.852 at.% of N respectively. The atomic structures are relaxed before all the other electronic calculations. The validity of this calculation is backed up by the work for pristine graphene in 4.3.3 and comparison of it with a previous work (Klintenberg et al., 2009).

### 5.3.2 Preliminary experiments with pristine CVD graphene

SE data from pristine CVD graphene is acquired to check if the measurements and data analyses methods are valid by comparing with previous reports. The fitting methods are expressed in the previous section, and the measurements are performed for 9 different

regions that are covered with graphene<sup>12</sup> and the averaged  $\alpha$  and  $\beta$  from the 9 measurements has been used. The standard deviations of  $\alpha$  and  $\beta$  are 0.019% and 0.09% of the average values respectively.

The RI values of pristine graphene samples obtained by the SE data fitting are given in Figure 5.12. Note that the 6 curves presented have the same data fitting errors  $\chi^2$  after iterations from different initial parameters in Fano model. The criterion for stopping the fitting is that the change of  $\chi^2$  by the last 10 iterations should be smaller than 0.0001. Thus, the 6 different solutions are for the local minima of the  $\chi^2$ , and the global minimum value of  $\chi^2$  is smaller than these local minima by only  $\sim 0.001$ , with the  $(n, k)$  on the center of the 6 curves shown in Figure 5.12.

While the real part ( $n$ ) of RI matches well with the previous results, the imaginary part ( $k$ ) is smaller than them. This is attributed to the PMMA residues that are lowering the mobility of the charge carriers in graphene, as identified by the peak deconvolution of XPS data from the sample (Figure 5.13). The normal sp<sup>2</sup> bonding of graphene honeycomb lattice is characterized by the leftmost peak around 284.5eV, while the other peaks are from PMMA or other residues (A. Pirkle et al., 2011). It seems that further cleaning of the residues can improve the quality of the sample and give the RI values similar to the values reported earlier.

### 5.3.3 Data analysis and discussions

N-doped CVD graphene is synthesized by flowing ammonia gas in the middle of the graphene synthesis process, and the XPS result convicts the existence of the nitrogen atoms in the graphene layer, as in Figure 5.14 where the atomic concentration of N is

---

<sup>12</sup> Confirmed by Raman spectroscopy and XPS analysis

~2.4%. The similar peak intensity of one of the C peaks at 285.5 eV indicates that the NdG sample also has the similar amount of PMMA residues compared with the pristine graphene sample.

One of the peaks in the XPS data, located at around 287.7 eV, is the evidence of the C-N bonding (Y. -C. Lin et al., 2010). Compared to the XPS data from pristine graphene, the intensity of this peak is more than 2 times higher, which can make sure that the N atoms are covalently bonded with carbon atoms constituting the graphene layer.

Unlike the data fitting for the pristine graphene's SE measurements, the fitting for NdG shows steeper convergence toward the minimum of the fitting error,  $\chi^2$  (Figure 5.15). The  $\chi^2$  starts from 241.677 for the highest RI curves in Figure 5.15, and it decrease to 241.67, 241.668, and 241.648 as the RI becomes smaller. Although not presented, even smaller RI curves result in larger  $\chi^2$ , so the lowest RI curves in Figure 5.15 are the best fit to the current measurements for NdG.

Although not reproducing the prediction by DFT (in section 5.1.2 and Figure 5.11), the Nitrogen doping to graphene seems to lower both the real and the imaginary parts of RI values from those of pristine graphene (compare Figures 5.12 and 5.15). This can be attributed to the lowered carrier mobility by the increased number of defects and/or dislocations in NdG by introducing the Nitrogen atoms, as well as the effects from N atoms themselves. Note that the amount of the PMMA residues is similar for both the samples by inspecting the XPS signals, so the reduction of  $n$  and  $k$  cannot be explained solely with the polymer residues. Further research with refined synthesis, transfer, and measurements methods will be able to reveal the inherent effects by nitrogen doping on graphene in the future.

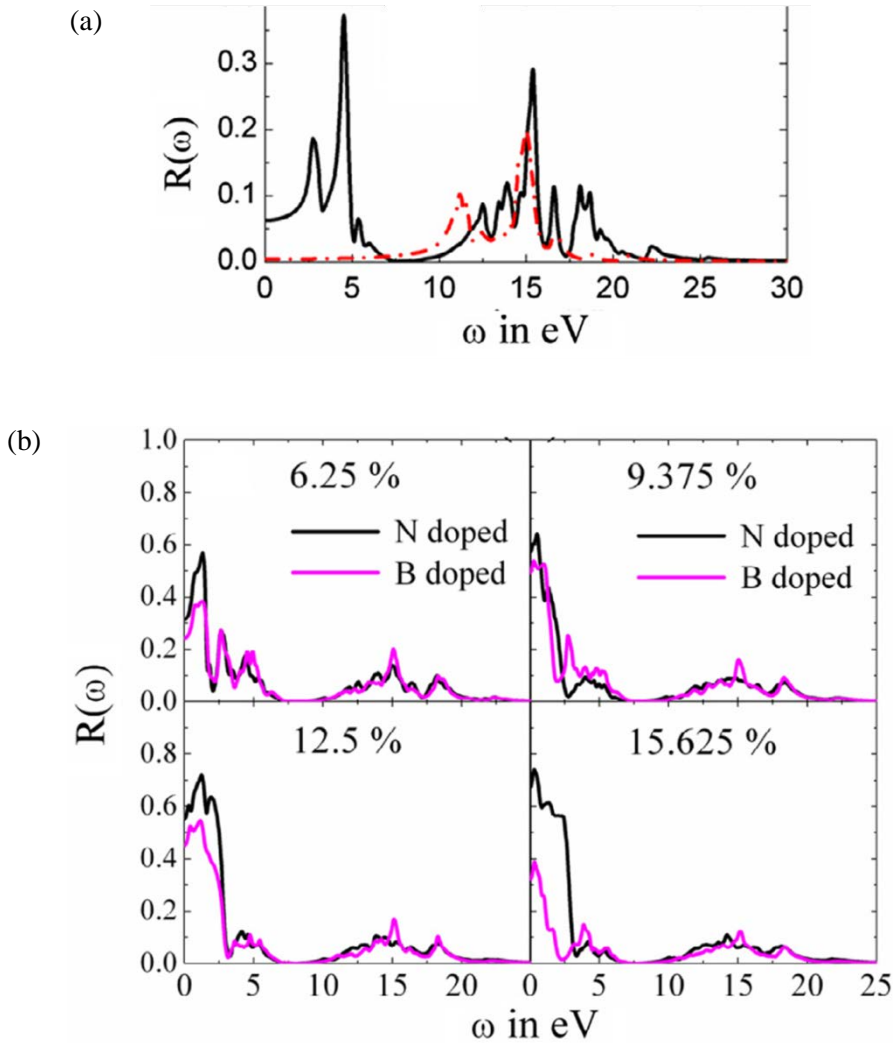


Figure 5.1 (P. Nath et al., 2014) Calculated reflectivity functions of pristine and doped graphene layers. (a) Reflectivity functions of pristine graphene for both parallel ( $\epsilon_{xx}$ ) and perpendicular ( $\epsilon_{zz}$ ) polarizations, (b) reflectivity functions of doped graphene with 4 different doping concentrations, for the parallel polarization. All data are the DFT calculation results.

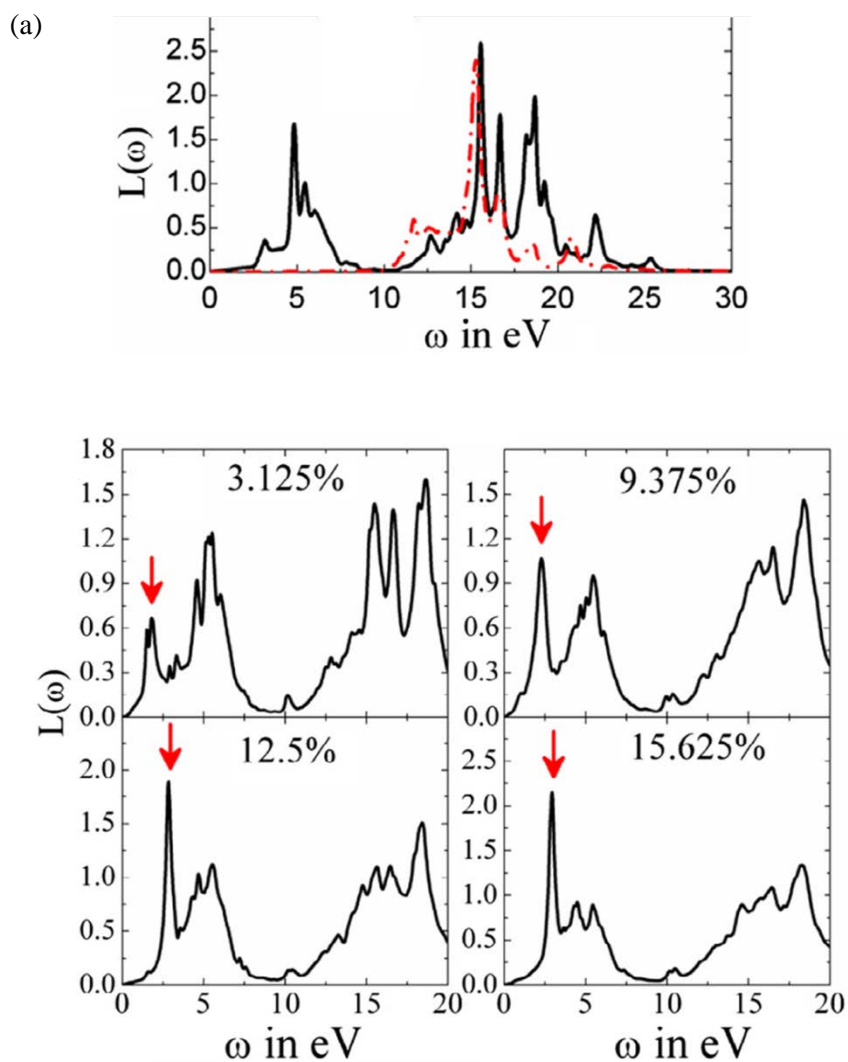


Figure 5.2 (P. Nath et al., 2014) Calculated EELS functions of pristine graphene (a) for the both polarizations, parallel ( $\epsilon_{xx}$ ) and perpendicular ( $\epsilon_{zz}$ ), and those of NdG (b) for the parallel polarization. New EELS peaks are identified by downward arrows. All data are the DFT calculation results.

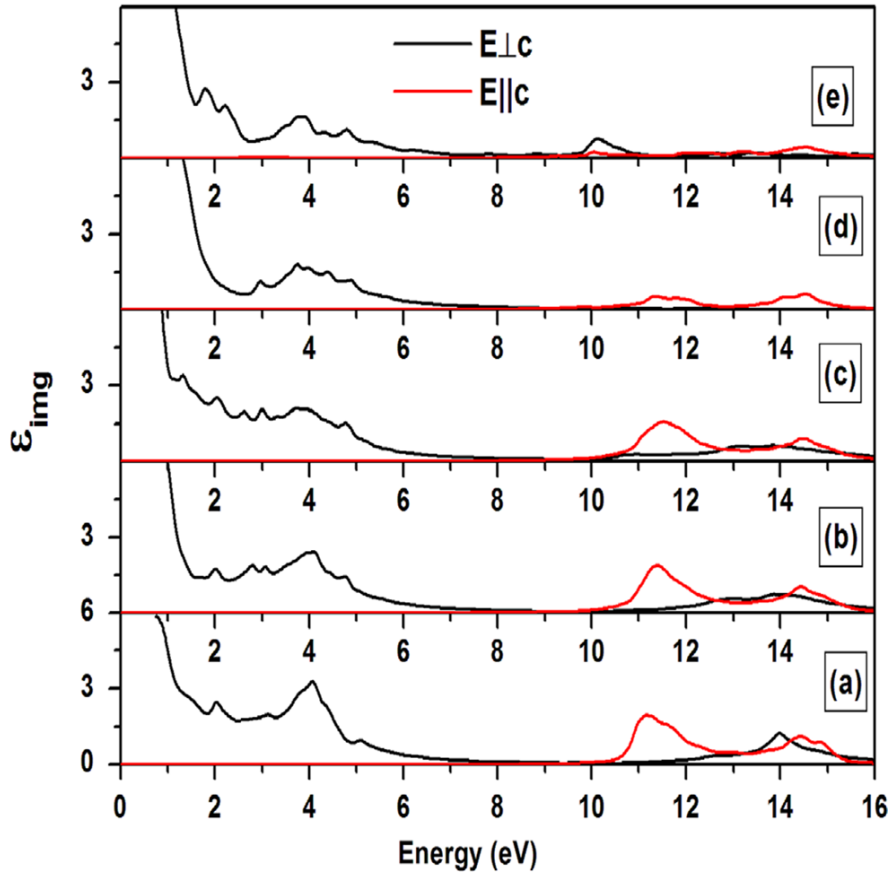


Figure 5.3 (P. Rani et al., 2014) The imaginary part of dielectric function for pure graphene (a) as compared with graphene sheet doped with different concentrations of nitrogen (b) in increasing order, 3.125% (b), 6.25% (c), 9.375% (d) and 18.75% (e) respectively for parallel ( $\epsilon_{xx}$ ) and perpendicular ( $\epsilon_{zz}$ ) polarizations.

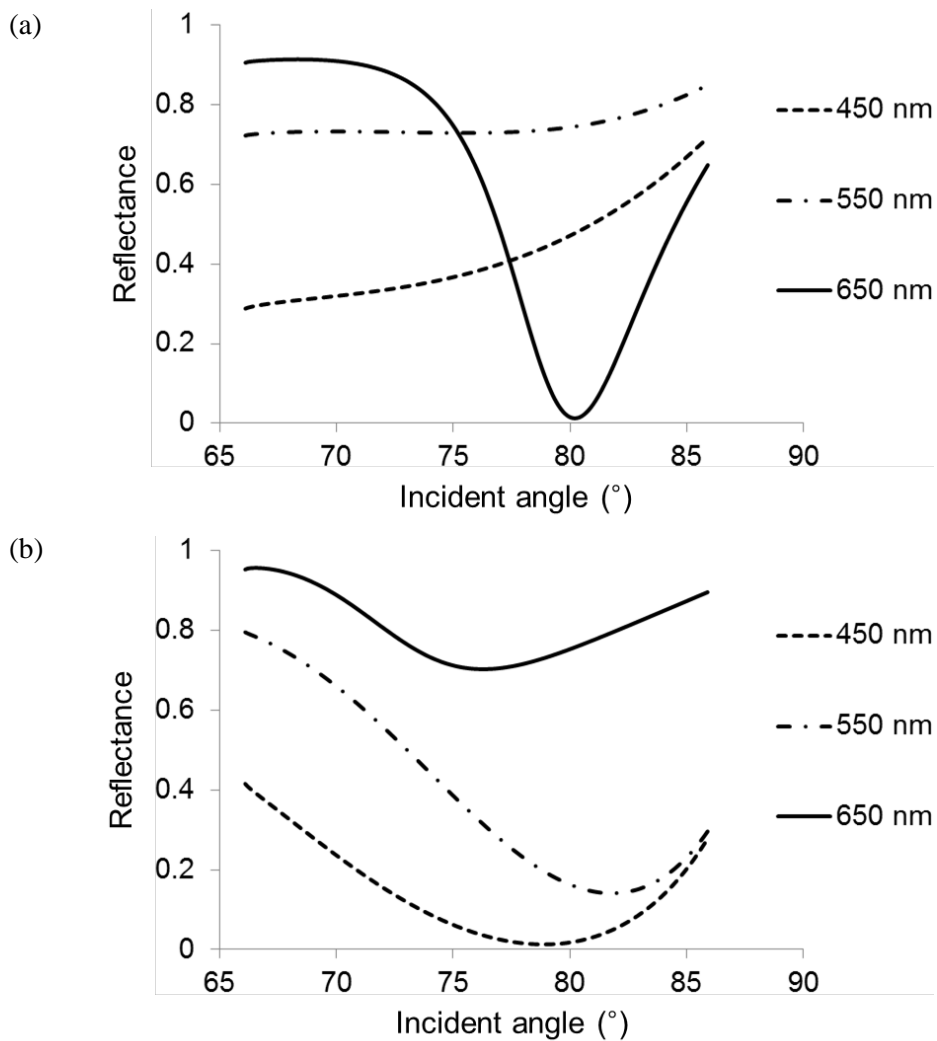


Figure 5.4 Calculated SPR reflectance curves for three different incident wavelengths, with the quartz prism and the water medium. (a) Reflectance from the 48 nm thick Au film and (b) from the 20 nm thick Au film. The results clearly show that the original setup in Chapter 4, i.e. 48 nm Au in (a), cannot be used for the multi-wavelength measurements. Although the three curves for 20 nm Au (b) have the minimum values, so the  $\theta_{\text{SPR}}$ , the dips are much broader than the case in Chapter 4.

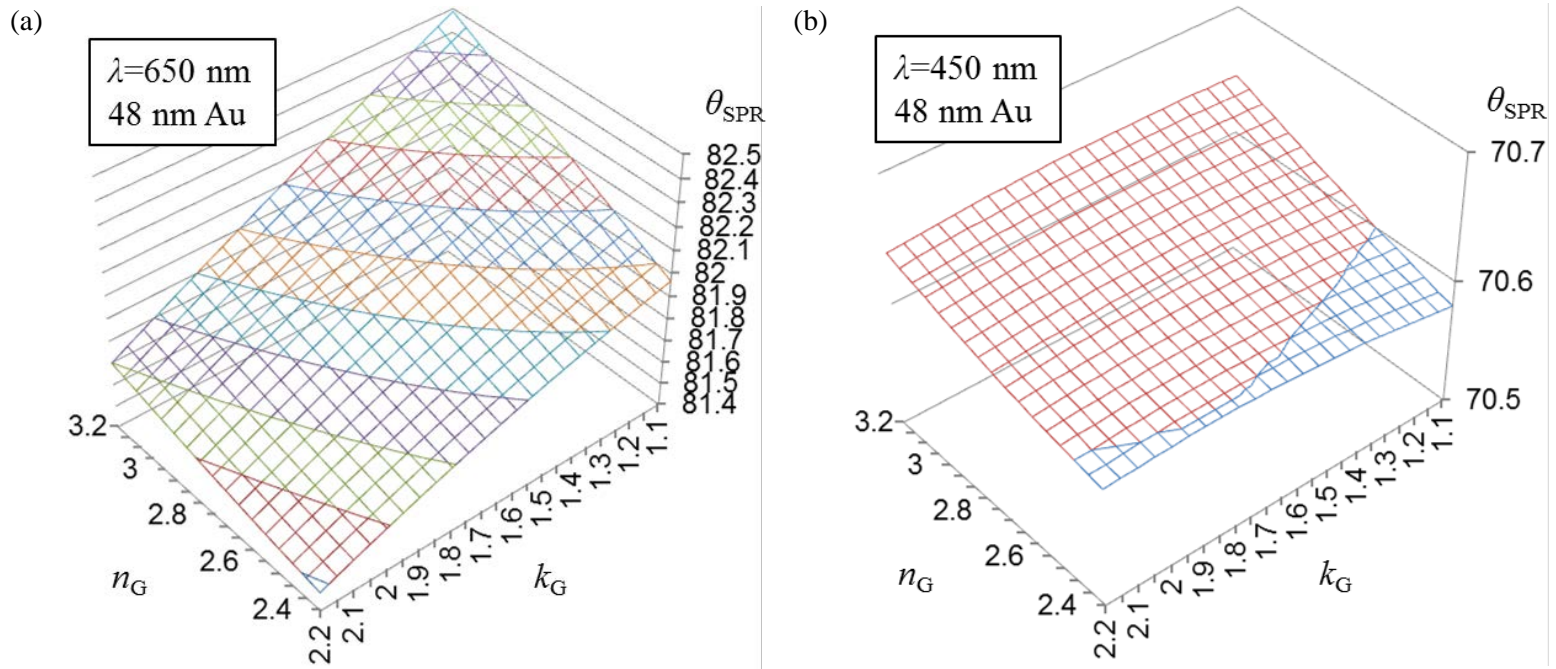


Figure 5.5 SPR angles ( $\theta_{\text{SPR}}$ ) calculated as functions of the ( $n_G$ ,  $k_G$ ) of the 3L graphene layers for the 48 nm Au film on 2 nm Ti layer for the adhesion to the quartz substrate, and the medium is water. Compared to (a) incident wavelength of 650 nm, (b) the 450 nm wavelength case shows significantly lower gradient of  $\theta_{\text{SPR}}$ , which means that for the  $\lambda=450$  nm light, the  $\theta_{\text{SPR}}$  has much lower RI sensitivity.

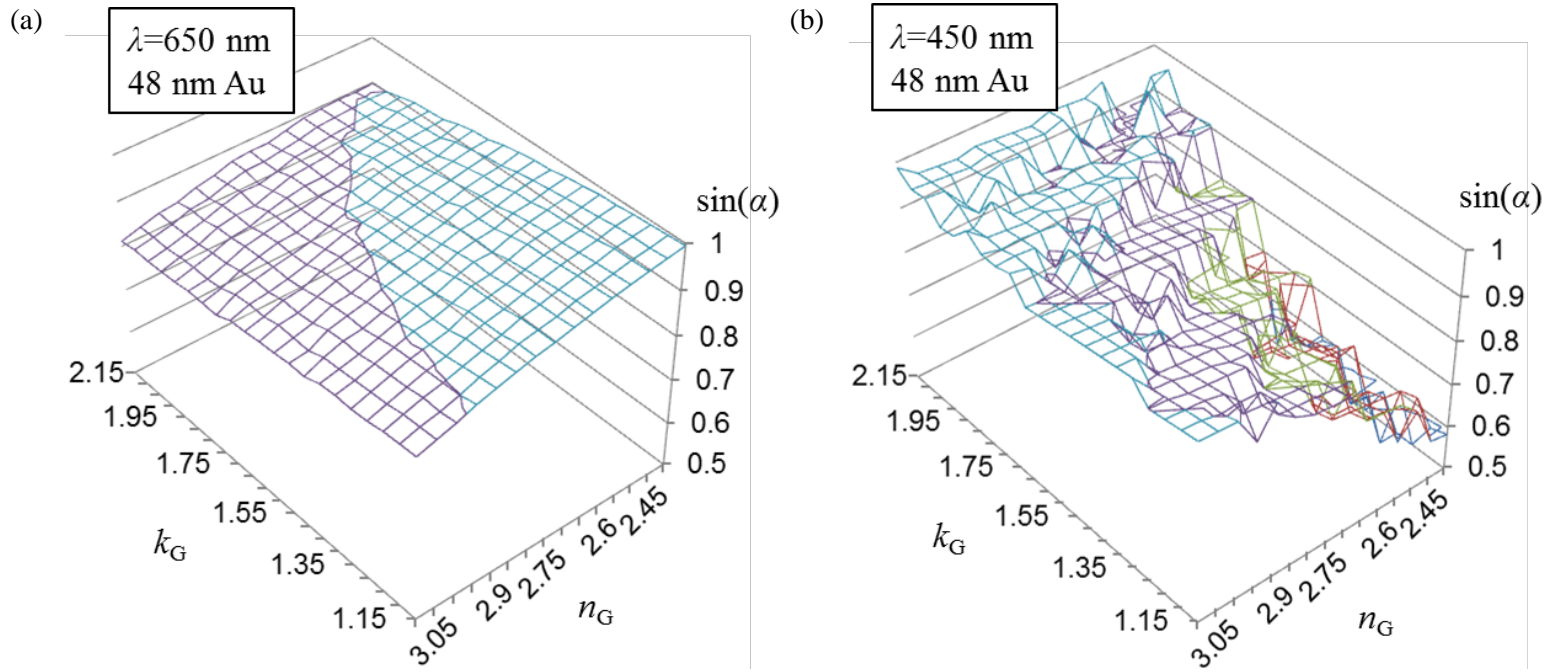


Figure 5.6 Orthogonality between the two observables,  $\theta_{\text{SPR}}$  and  $R_p/R_s^*$  by using the method in Section 4.3.3, for wavelengths of 650 nm (a) and 450 nm (b), for the 48 nm Au film. The  $\theta_{\text{SPR}}$  data are in Figure 5.5 and the  $R_p/R_s^*$  data is in Figure 4.3-a. Since the two observables should be orthogonal to each other ideally, i.e.  $\sin(\alpha)=1$ , the tandem use of the SPR and ATR for the  $\lambda=450$  nm incident light will result in considerably larger uncertainties than those of the pristine graphene measurements in Figure 4.6.

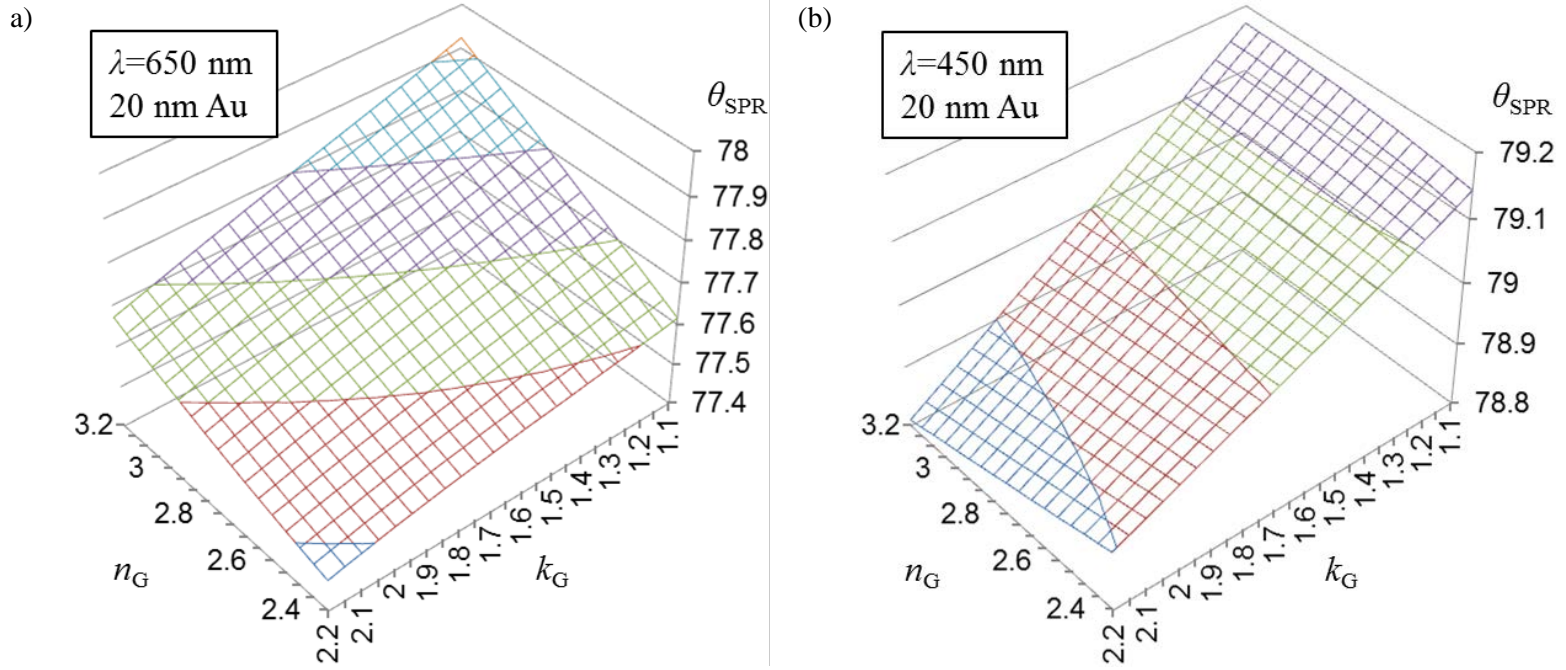


Figure 5.7 SPR angles ( $\theta_{\text{SPR}}$ ) calculated as functions of the ( $n_G$ ,  $k_G$ ) of the 3L graphene layers for the 20 nm Au film on 2 nm Ti layer for the adhesion to the quartz substrate, and the medium is water. Unlike the Au film of thickness 48 nm, the gradients of  $\theta_{\text{SPR}}$  for both of the wavelengths are similar to each other.

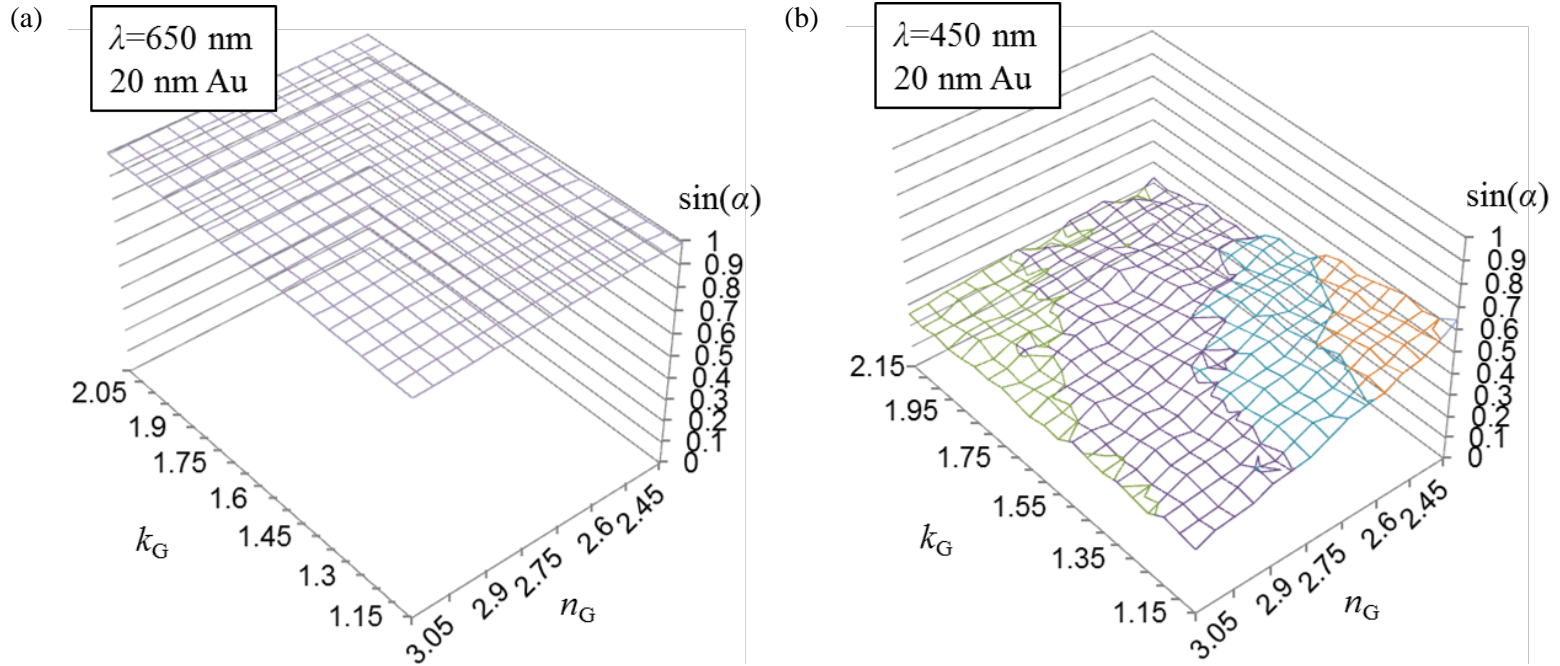


Figure 5.8 Orthogonality between the two observables,  $\theta_{\text{SPR}}$  and  $R_p/R_s^*$  by using the method in Section 4.3.3, for wavelengths of 650 nm (a) and 450 nm (b), for the 20 nm Au film. The  $\theta_{\text{SPR}}$  data are in Figure 5.7 and the  $R_p/R_s^*$  data is in Figure 4.3-a. Unfortunately, the orthogonality for the 450 nm wavelength is smaller than 0.5 for most of the  $(n_G, k_G)$  values, meaning that the tandem use of the SPR and ATR will give considerably larger uncertainties than the values of pristine graphene reported in section 4.3.3 and Figure 4.6.

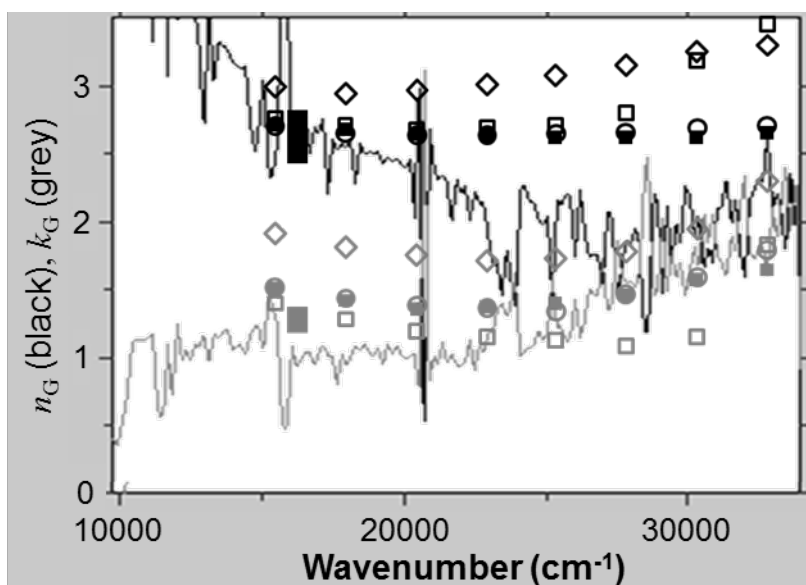


Figure 5.9 RI of pristine graphene on a PDMS substrate measured by spectroscopic ellipsometry in present work (lines) and previous articles (symbols). The large noise of the current work is due to the transparency and the small roughness (order of 1 nm) of the PDMS substrate. Open diamonds: A. Matković et al., 2012, open circles: V. G. Kravets et al., open squares: 2010, J. W. Weber et al., 2010, and closed squares: Nelson et al., 2010.

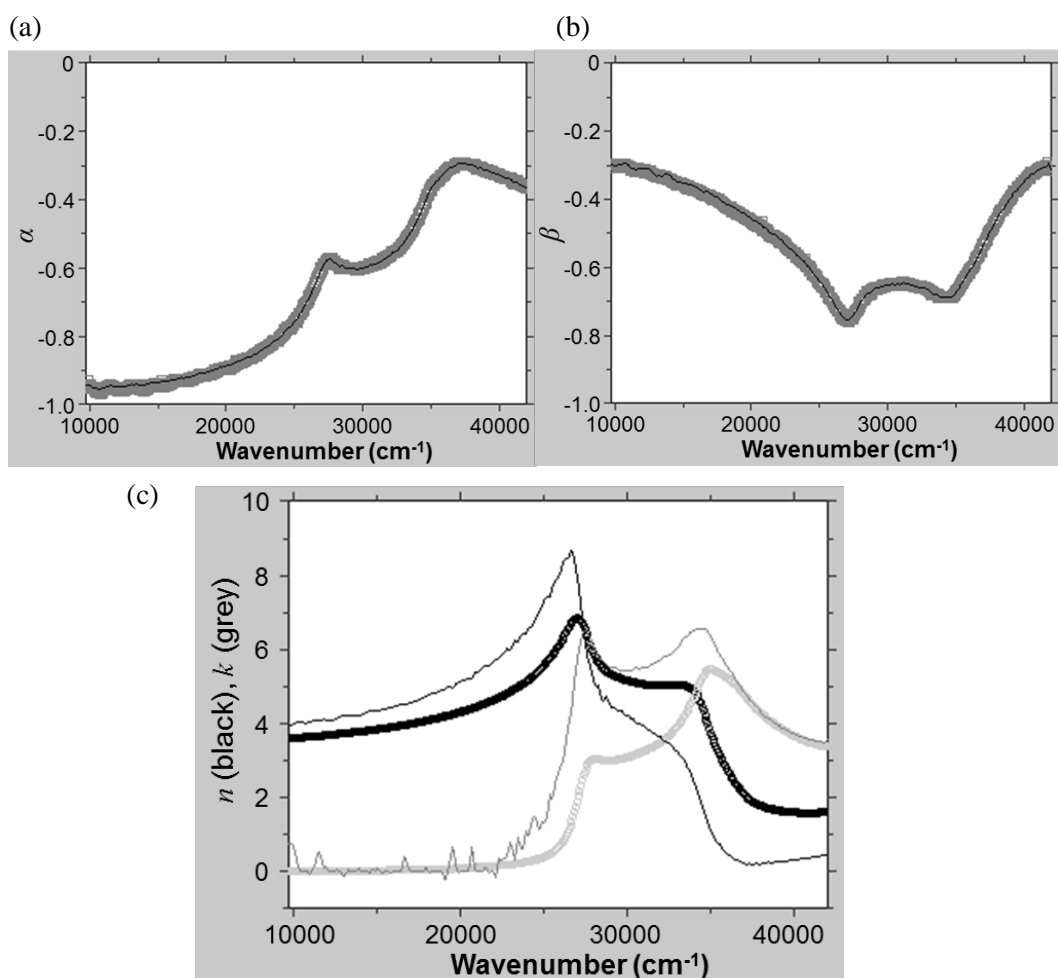


Figure 5.10 SE data fitting from a silicon substrate. The raw data  $\alpha$  and  $\beta$  are in (a) and (b) respectively, where the grey curves are for measured data and thin black lines are showing the best fits. The effects of native  $\text{SiO}_2$ , PMMA residues, etc. are included in the “effective substrate” with complex pseudo RI in (c) as thin curves, which are corresponding to the best fits shown in (a) and (b). The thick curves in (c) are the RI values of pure silicon.

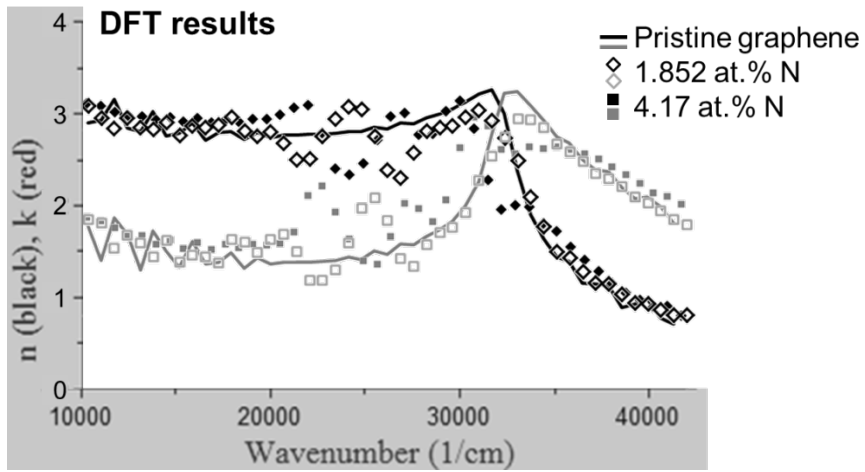


Figure 5.11 DFT calculation results for pristine and graphitic N-doped graphene for two atomic concentrations. The RI change by the doping is the largest in wavenumber region between 20000 and 30000  $\text{cm}^{-1}$ , or equivalently between 500 nm and 333 nm of the wavelength of light.

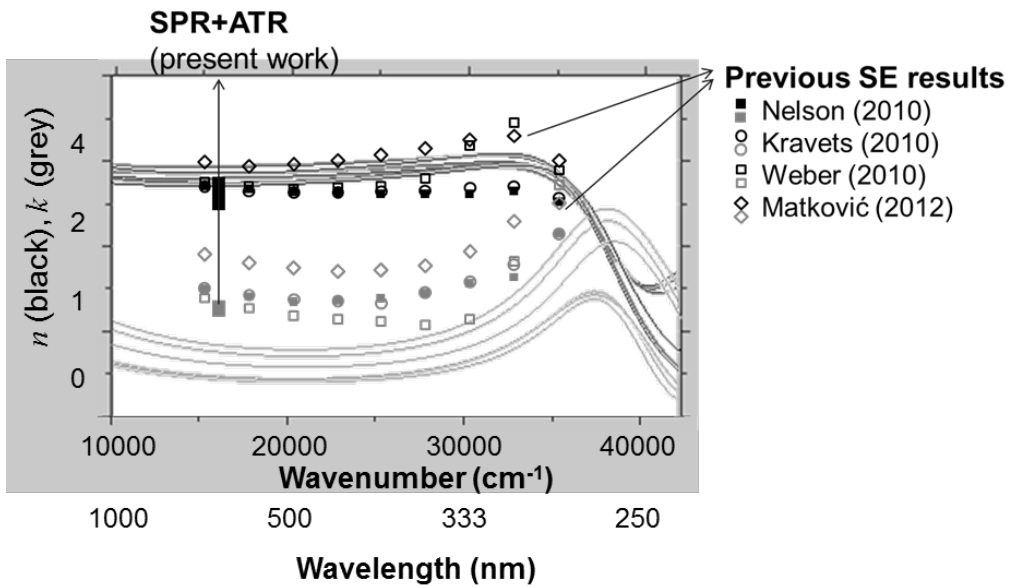


Figure 5.12 The 6 RI functions of pristine graphene by SE (curves) having the same data fitting errors. Compare with the previous results and the results shown in Chapter 4, the SE measurements predict smaller value of the imaginary part of RI, which can be attributed to the quality of the CVD graphene sample. The minimum data fitting error can be achieved at the center of the six curves (not presented here), but the difference of errors is less than  $10^{-5}$ .

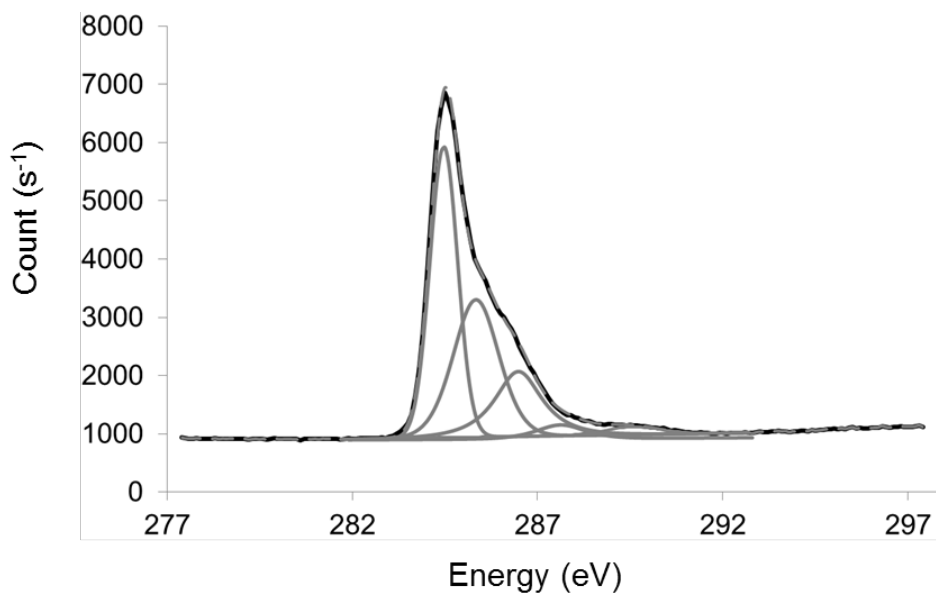


Figure 5.13 XPS data (black) from pristine graphene sample, composed of 5 peaks (grey curves) that are summed up to grey dashed curve. The  $sp^2$  bonding of graphene honeycomb lattice is characterized by the leftmost peak, while the other peaks are from PMMA or other residues (A. Pirkle et al., 2011).

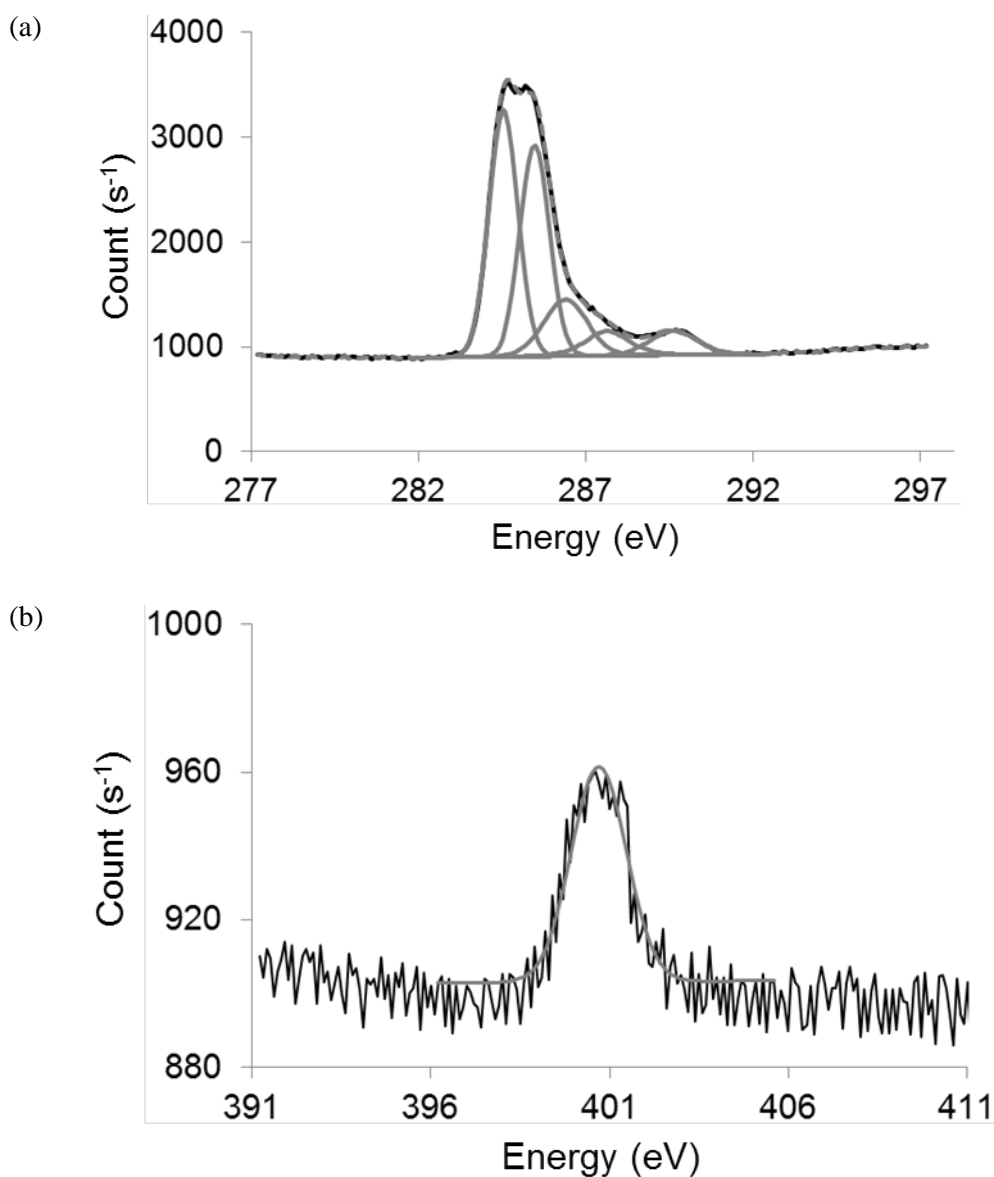


Figure 5.14 (a) C peaks from the XPS data (black) from N-doped graphene sample, composed of 5 peaks (grey curves) that are summed up to grey dashed curve. (b) N 1s peak from the same XPS data. The atomic concentration of N is 2.4%, compared with the leftmost grey peak in (a) accounting for the sp<sup>2</sup> bonding in graphene.

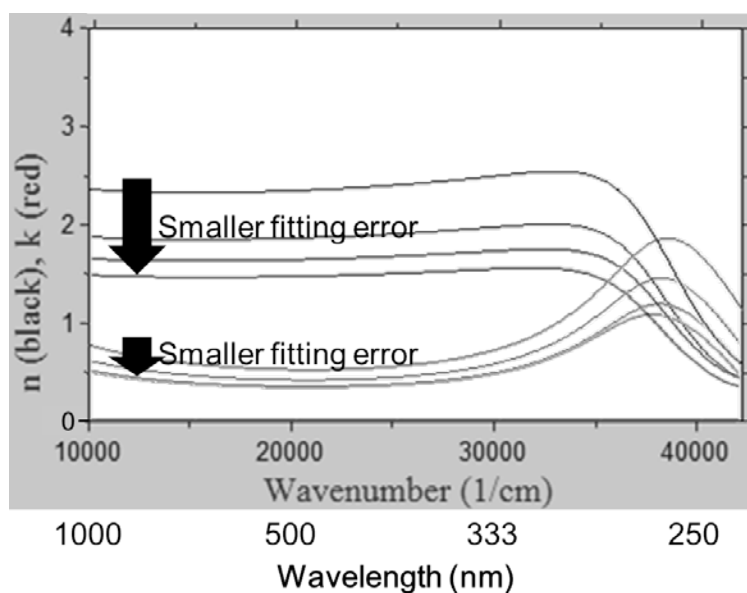


Figure 5.15 SE data fitting results for the N-doped graphene sample. Unlike the case of the pristine graphene, the fitting error gradually decreases as both the  $n$  (upper 4 curves) and  $k$  (lower 4 curves) become smaller until the global minimum of the fitting error (lowest  $n$  and  $k$  in the figure), i.e. the best fit to the SE measurements for NdG.

## Chapter 6. Summary and Conclusion

Graphene, which is too thin to identify, measure, and characterize with conventional optical tools has been studied by using two near-field optical methods (SPR and ATR) and one far-field technique measuring the amplitude and phase change of the light (SE). In this thesis, new optical characterization methods for imaging, layer counting, and refractive index (RI) measurements of graphene have been developed and presented the successful performance. None of the methods used in current work resorts to the scanning probe tips, which can be intrusive, slow, and hard to position and control the samples.

1. To reliably count the CVD graphene layers, the SPR reflectance from the graphene layer on a 48-nm thick gold layer is observed. The SPR reflectance has reliably discriminated the 1-, 3-, and 5-layer CVD graphene layers, enabling the robust counting of the graphene layer number. Not only the reflectance curve shapes of the SPR,  $R(\theta)$ , but the measured SPR angles, i.e. the incident angles for the minimum reflection, match the calculation results from the Fresnel's equations. This is in contrast to the recent studies for the identification and counting of the graphene layers based on Raman spectroscopy, AFM, or reflection spectroscopy, all having limitations in accuracy, reliability, and capability of the graphene layer counting. These limitations are more severe when counting graphene made by CVD, because of their large area, irregular profile, randomly oriented grains, and organic residues that may exist from transfer processes.

2. The novel method to measure the complex RI of graphene has been developed by using the two near-field phenomena simultaneously, the SPR and the ATR reflectance.

Unlike previous works on the graphene RI measurements, the current method has solved the problem fundamentally by using “2 results from 2 observables”, not “2 results from 1 observable with fitting”. Furthermore, the two observables have shown high sensitivities for graphene RI measurements, as presented quantitatively by the theoretical analyses. The measured 1-, 3-, and 5-layer graphene RI values at 634 nm wavelength lie in the middle of the previously reported data while the variations are within  $\pm 3\%$ , and match well with the density functional theory (DFT) calculation result by current work. The accurate optical properties measurements of graphene are necessary in various research and application fields such as the thermal conductivity measurements of graphene by opto-thermal Raman spectroscopy, prediction of the absorption and reflection from the transparent graphene electrodes and color shifts in flexible displays, etc.

3. Finally, the complex RI measurements for the N-doped graphene layers have been conducted by SE. Because the DFT calculation predicts that the N-doping on graphene will result in the significant change of RI at specific wavelengths, spectroscopic measurements are desirable for the comparison with the pristine graphene's RI. Unfortunately, the tandem use of SPR and ATR has been proven to be not applicable to this problem, so the SE has been used. The results have presented that the N-doping can lower both the real and imaginary parts of graphene's RI significantly, which can be attributed to the increased defect levels and consequently the lowered carrier mobility. Further research with refined synthesis, transfer, and measurements methods will be able to unveil the inherent effects by nitrogen doping on graphene in the future.

## References

R. M. A. Azzam and N. M. Bashara, 1977, *Ellipsometry and polarized light*, Amsterdam, New York.

S. Bae, H. Kim, Y. Lee, X. F. Xu, J. S. Park, Y. Zheng, J. Balakrishnan, T. Lei, H. R. Kim, Y. I. Song, Y. J. Kim, K. S. Kim, B. Ozyilmaz, H. J. Ahn, B. H. Hong, and S. Iijima, 2010, *Nature Nanotechnology* 5, pp. 574-578.

C. A. Balanis, 1989, *Advanced Engineering Electromagnetics*, John Wiley & Sons, pp. 71-84.

P. Blake, E. W. Hill, A. H. C. Neto, K. S. Novoselov, D. Jiang, R. Yang, T. J. Booth, and A. K. Geim, 2007, Making graphene visible, *Applied Physics Letters* 91(6), 063124.

M. Bruna and S. Borini, 2009, Optical constants of graphene layers in the visible range, *Applied Physics Letters* 94, pp. 031901-031903.

I. Calizo, W. Bao, F. Miao, C. N. Lau, A. A. Balandin, 2007, The effect of substrates on the Raman spectrum of graphene: Graphene- on-sapphire and graphene-on-glass, *Applied Physics Letters* 91, 201904.

J. Campos-Delgado, G. Algara-Siller, C. N. Santos, U. Kaiser, and J. -P. Raskin, 2013, Twisted bi-layer graphene: microscopic rainbows. *Small* 9, pp. 3247–3251.

C. Casiraghi, S. Pisana, K. S. Novoselov, A. K. Geim, A. C. Ferrari, 2007, Raman fingerprint of charged impurities in graphene, *Applied Physics Letters* 91, 233108.

S. Cheon, K. D. Kihm, H. g. Kim, G. Lim, J. S. Park, and J. S. Lee, 2014, How to reliably determine the complex refractive index (RI) of graphene by using two independent measurement constraints, *Scientific Reports* 4, 6364.

S. Cheon, K. D. Kihm, J. S. Park, J. S. Lee, B. J. Lee, H. Kim, and B. H. Hong, 2012, How to optically count graphene layers, *Optics Letters* 37(18), pp. 3765-3767.

C. Chiritescu, D. G. Cahill, N. Nguyen, D. Johnson, A. Bodapati, P. Keblinski, and P. Zschack, 2007, Ultralow thermal conductivity in disordered, layered WSe<sub>2</sub> crystals, *Science* 19, pp. 351-353.

C. W. Chiu, S. C. Chen, Y. C. Huang, F. L. Shyu, and M. F. Lin, 2013, Critical optical properties of AA-stacked multilayer graphenes, *Applied Physics Letters* 103, 041907.

U. Fano, 1956, Atomic theory of electromagnetic interactions in dense materials. *Physical Review* 103(5), 1202.

A. C. Ferrari, J. C. Meyer, V. Scardaci, C. Casiraghi, M. Lazzeri, F. Mauri, S. Piscanec, D. Jiang, K. S. Novoselov, S. Roth, and A. K. Geim, 2006, Raman spectrum of graphene and graphene layers, *Physical Review Letters* 97, 187401.

P. E. Gaskell, H. S. Skulason, C. Rodenchuk, and T. Szkopek, 2009, Counting graphene layers on glass via optical reflection microscopy, *Applied Physics Letters* 94, 143101.

P. Gava, M. Lazzeri, A. M. Saitta, and F. Mauri, 2009. Ab initio study of gap opening and screening effects in gated bilayer graphene, *Physical Review B* 79, 165431.

A. K. Geim, 2009, Graphene: status and prospects, *Science* 324, pp. 1530-1534.

A. K. Geim and K. S. Novoselov, 2007, The rise of graphene, *Nature Materials* 6, pp. 183-191.

D. Graf, F. Molitor, K. Ensslin, C. Stampfer, A. Jungen, C. Hierold, L. Wirtz, 2007, Spatially resolved Raman spectroscopy of single- and few-layer graphene, *Nano Letters* 7(2), pp. 238-242.

D. L. Greenaway, G. Harbeke, F. Bassani, and E. Tosatti, 1969, Anisotropy of the optical constants and the band structure of graphite, *Physical Review* 178, pp. 1340-1348.

A. Gupta, G. Chen, P. Joshi, S. Tadigadapa, and P. C. Eklund, 2006, Raman scattering from high-frequency phonons in supported n-graphene layer films, *Nano Letters* 6(12), pp. 2667-2673.

M. Y. Han, J. C. Brant, P. Kim, 2010, Electron transport in disordered graphene nanoribbons, *Physical Review Letters* 104, 056801.

G. Hass, M. H. Francombe, and R. W. Hoffman, 1977, *Physics of Thin Films* 9, Academic Press, Inc., pp. 168-171, 241-242.

J. D. Jackson, *Classical Electrodynamics*, 3rd edition, 1999, John Wiley & Sons, Inc.

Z. Jin, J. Yao, C. Kittrell, and J. M. Tour, 2011, Large-scale growth and characterizations of nitrogen-doped monolayer graphene sheets, *ACS Nano* 5(5), pp. 4112-4117.

K. D. Kihm, 2011, *Near-Field Characterization of Micro/Nano-Scaled Fluid Flows*, Springer Science & Business Media.

K. D. Kihm, S. Cheon, J. S. Park, H. J. Kim, J. S. Lee, I. T. Kim, and H. J. Yi, 2012, Surface plasmon resonance (SPR) reflectance imaging: Far-field recognition of near-field phenomena, *Optics and Lasers in Engineering* 50, pp. 64-73.

K. D. Kihm, J. S. Park, S. Cheon, and J. S. Lee, 2011, Microscopic images of graphene layers of different thicknesses, *Journal of Heat Transfer* 133(8), 080902.

K. S. Kim, Y. Zhao, H. Jang, S. Y. Lee, J. M. Kim, K. S. Kim, J.-H. Ahn, P. Kim, J.-Y. Choi, and B. H. Hong, 2009, Large-scale pattern growth of graphene films for stretchable transparent electrodes, *Nature* 457, pp. 706-710.

M. Klintonberg, S. Lebègue, C. Ortiz, B. Sanyal, J. Fransson, and O. Eriksson, 2009, Evolving properties of two-dimensional materials: from graphene to graphite, *Journal of Physics: Condensed Matter* 21, 335502.

V. G. Kravets, A. N. Grigorenko, R. R. Nair, P. Blake, S. Anissimova, K. S. Novoselov, and A. K. Geim, 2010, Spectroscopic ellipsometry of graphene and an exciton-shifted van Hove peak in absorption, *Physical Review B* 81, 155413.

K. Kurihara and K. Suzuki, 2002, Theoretical understanding of an absorption-based surface plasmon resonance sensor based on Kretschmann's theory, *Analytical Chemistry* 74(3) pp. 696-701.

C. Lee, X. Wei, J. W. Kysar, and J. Hone, Measurement of the elastic properties and intrinsic strength of monolayer graphene, *Science* 321, pp. 385-388.

X. Li, W. Cai, J. An, S. Kim, J. Nah, D. Yang, R. Piner, A. Velamakanni, I. Jung, E. Tutuc, S. K. Banerjee, L. Colombo, and R. S. Ruoff, 2009, Large-area synthesis of high-quality and uniform graphene films on copper foils, *Science* 324(5932), pp. 1312-1314.

X. S. Li, W. W. Cai, L. Colombo, and R. S. Ruoff, 2009, Evolution of graphene grown on Ni and Cu by carbon isotope labeling, *Nano Letters* 9(12), pp. 4268-4272.

Y.-M. Lin, K. A. Jenkins, A. Valdes-Garcia, J. P. Small, D. B. Farmer, and P. Avouris, 2008, Operation of graphene transistors at gigahertz frequencies, *Nano Letters* 9, pp. 422-426.

Y. -C. Lin, C. -Y. Lin, and P. -W. Chiu, 2010, Controllable graphene N-doping with ammonia plasma, *Applied Physics Letters* 96, 133110.

H. Liu, A. T. Neal, Z. Zhu, Z. Luo, X. Xu, D. Tománek, and P. D. Ye, 2014, Phosphorene: an unexplored 2D semiconductor with a high hole mobility, *ACS Nano* 8(4), pp. 4033-4041.

S. Maier, 2007, *Plasmonics: fundamentals and applications*, Springer Verlag.

L. M. Malard, M. H. D. Guimaraes, D. L. Mafra, M. S. C. Mazzoni, A. Jorio, 2009, Group-theory analysis of electrons and phonons in N-layer graphene systems, *Physical Review B* 79(12), 125426.

L. M. Malard, M. A. Pimenta, G. Dresselhaus, and M. S. Dresselhaus, 2009, Raman spectroscopy in graphene, *Physics Reports* 473(5-6), pp. 51-87.

A. Matković, A. Beltaos, M. Milicević, U. Ralević, B. Vasić, D. Jovanović, and R. Gajić, 2012, Spectroscopic imaging ellipsometry and Fano resonance modeling of graphene, *Journal of Applied Physics* 112, 123523.

R. R. Nair, P. Blake, A. N. Grigorenko, K. S. Novoselov, T. J. Booth, T. Stauber, N. M. R. Peres, A. K. Geim, 2008, Fine structure constant defines visual transparency of graphene, *Science* 320, p. 1308.

P. Nath, S. Chowdhury, D. Sanyal, and D. Jana, 2014, Ab-initio calculation of electronic and optical properties of nitrogen and boron doped graphene nanosheet, *Carbon* 73, pp. 275-282.

F. J. Nelson, V. K. Kamineni, T. Zhang, E. S. Comfort, J. U. Lee and A. C. Diebold,

2010, Optical properties of large-area polycrystalline chemical vapor deposited graphene by spectroscopic ellipsometry, *Applied Physics Letters* 97, 253110.

Z. H. Ni, H. M. Wang, J. Kasim, H. M. Fan, T. Yu, Y. H. Wu, Y. P. Feng, and Z. X. Shen, 2007, Graphene thickness determination using reflection and contrast spectroscopy, *Nano Letters* 7, pp. 2758-2763.

K. S. Novoselov, A. K. Geim, S. V. Morozov, D. Jiang, Y. Zhang, S. V. Dubonos, I. V. Grigorieva, and A. A. Firsov, 2004, Electric field effect in atomically thin carbon films, *Science* 306(5696), pp. 666-669.

A. Otto and W. Sohler, 1971, Modification of the total reflection modes in a dielectric film by one metal boundary, *Optics Communications* 3, pp. 254-258.

E. D. Palik, *Handbook of Optical Constants of Solids*, 1998, Elsevier, New York.

J. S. Park, K. D. Kihm, H. g. Kim, G. Lim, S. Cheon, and J. S. Lee, 2014, Wetting and evaporative aggregation of nanofluid droplets on CVD-synthesized hydrophobic graphene surfaces, *Langmuir* 30(28), pp. 8268-8275.

A. Pirkle, J. Chan, A. Venugopal, D. Hinojos, C. W. Magnuson, S. McDonnell, L. Colombo, E. M. Vogel, R. S. Ruoff and R. M. Wallace, 2011, The effect of chemical residues on the physical and electrical properties of chemical vapor deposited graphene transferred to SiO<sub>2</sub>, *Applied Physics Letters* 99, 122108.

B. Radisavljevic, A. Radenovic, J. Brivio, V. Giacometti, and A. Kis, 2011, Single-layer MoS<sub>2</sub> transistors, *Nature Nanotechnology* 6, pp. 147-150.

Q. Ran, M. Gao, X. Guan, Y. Wang, and Z. Yu, 2009, First-principles investigation on bonding formation and electronic structure of metal-graphene contacts, *Applied Physics Letters* 94, 103511.

P. Rani, G. S. Dubey, and V. K. Jindal, 2014, DFT study of optical properties of pure and doped graphene, *Physica E* 62, pp. 28-35.

Y. -W. Son, M. L. Cohen, and S. G. Louie, 2006, Half-metallic graphene nanoribbons, *Nature* 444, pp. 347-349.

Y. Sui, and J. Appenzeller, 2009, Screening and interlayer coupling in multilayer graphene field-effect transistors, *Nano Letters* 9, pp. 2973-2977.

X. Wang, Y. P. Chen, and D. D. Nolte, 2008, Strong anomalous optical dispersion of graphene: complex refractive index measured by picometrology, *Optics Express* 16(26), pp. 22105-22112.

J. W. Weber, V. E. Calado, and M. C. M. Van de Sanden, 2010, Optical constants of graphene measured by spectroscopic ellipsometry, *Applied Physics Letters* 97, 091904.

D. Wei, Y. Liu, Y. Wang, H. Zhang, L. Huang, and G. Yu, 2009, Synthesis of N-doped graphene by chemical vapor deposition and its electrical properties, *Nano Letters* 9(5), pp.

1752-1758.

I. M. White and X. Fan, 2008, On the performance quantification of resonant refractive index sensors, *Optics Express* 16, pp. 1020–1028.

U. Wurstbauer, C. Röling, U. Wurstbauer, W. Wegscheider, M. Vaupel, P. H. Thiesen, and Dieter Weiss, 2010, Imaging ellipsometry of graphene, *Applied Physics Letters* 97, 231901.

W. Xu, X. Ling, J. Xiao, M. S. Dresselhaus, J. Kong, H. Xu, Z. Liu, and J. Zhang, 2012, Surface enhanced Raman spectroscopy on a flat graphene surface, *Proceedings of the National Academy of Sciences of the United States of America* 109(24), pp. 9281-9286.

T. Xue, X. Cui, J. Chen, C. Liu, Q. Wang, H. Wang, and W. Zheng, 2013, A switch of the oxidation state of graphene oxide on a surface plasmon resonance chip, *ACS Applied Materials and Interfaces* 5(6), pp. 2096-2103.

Q. Ye, J. Wang, Z. Liu, Z. –C. Deng, X. –T. Kong, F. Xing, X. –D. Chen, W. –Y. Zhou, C. –P. Zhang, and J. –G. Tian, 2013, Polarization-dependent optical absorption of graphene under total internal reflection. *Applied Physics Letters* 102, 021912.

L. Zhao, R. He, K. T. Rim, T. Schiros, K. S. Kim, H. Zhou, C. Gutierrez, S. P. Chockalingam, C. J. Arguello, L. Palova, D. Nordlund, M. S. Hybertsen, D. R. Reichman, T. F. Heinz, P. Kim, A. Pinczuk, G. W. Flynn, and A. N. Pasupathy, 2011, Visualizing individual nitrogen dopants in monolayer graphene, *Science* 333(6045), pp. 999-1003.

# 근접장 광학 기법을 통한 CVD 그래핀의 굴절률 분석

서울대학교 대학원

기계항공공학부

WCU 멀티스케일 기계설계 전공

천 소 산

## 요 약

탄소원자 단일층인 그래핀은 전기적, 광학적, 열적, 기계적인 특성이 매우 뛰어난 물질로 최근 다양한 분야에서 활발히 연구가 진행 중이다. 나노미터 미만에서 수 나노미터의 두께를 가진 그래핀의 신뢰성 있는 가시화 및 측정은 기초연구뿐만 아니라 실용적인 측면에서도 상당히 중요한 연구 주제이다. 본 연구에서는 그래핀을 가시화하고, 그 층수를 판별하고, 복소 굴절률을 측정하는 새로운 광학적인 방법을 개발하였다. 이를 위해 세 가지 근접장 광학 현상 또는 방법인 표면 플라즈몬 공명(SPR), 감쇠전반사(ATR), 타원편광 분광법(SE)가 사용되었고, 세 경우 모두 주사 탐침이 사용되지 않는 방법이다.

높은 신뢰성으로 CVD (화학기상증착) 그래핀의 층수를 세기 위해서 48 nm 두께의 금박 위에 그래핀을 올리고 SPR 반사광을 측정하였다. SPR 방법은

가장 민감하게 굴절률 변화를 감지할 수 있는 방법으로, 본 연구에서도 1장, 3장, 5장 그래핀을 성공적으로 구별해내었다. 입사각에 따른 반사도, 즉  $R(\theta)$ 뿐만 아니라 반사가 최소인 입사각에 해당하는 SPR 각도 또한 Fresnel의 반사 공식으로부터 계산된 이론과 잘 맞게 측정되었다. 그래핀이 원자 한 층으로 이루어져 매우 얇지만, SPR 측정 환경을 그래핀 판별에 최적화하여 근접장 감도가 매우 좋기 때문에 이렇게 층수를 판별해 낼 수 있었다. 이는 그래핀의 층수를 판별하기 위해 진행된 선행연구인 라만 분광법, 원자 힘 현미경(AFM), 반사 분광법 등이 모두 정확도, 신뢰성, 측정 범위 등에 뚜렷한 한계가 있는 것과 대조적이다. 이러한 단점들은 특히 CVD 그래핀의 층수를 셀 때에 더욱 부각되는데, 이는 CVD 그래핀의 넓이가 넓고, 물리적인 두께가 불규칙적이며, 격자(grain) 도메인이 임의적으로 정렬되어 있으며, 전사 도중에 불순물이 남기 때문이다.

그래핀의 복소 굴절률을 측정하기 위해 SPR과 ATR의 반사광을 동시에 이용하는 방법이 새롭게 개발되었다. 기존의 그래핀 굴절률 측정법들이 “하나의 계측과 피팅”으로 2개의 결과를 얻는 것과는 다르게, 이 방법은 “2개의 독립적 계측”으로 2개의 결과를 얻으므로 보다 근본적인 정확도 확보가 가능하다. 더욱이, 이 두 계측은 모두 그래핀과 근접장과의 상호작용에 기반을 두고 있기 때문에 더욱 굴절률 감도가 높으며, 이는 감도와 측정의 불확도에 대한 이론적 분석으로 알아볼 수 있었다. 1층, 3층, 5층 CVD 그래핀의 634 nm 파장에 대한 굴절률은 기존 선행 연구들에서 보고되었던 값들의 중간 지점에 위치하고 있으며, 그 산포는  $\pm 3\%$  이내이고, 본 연구에서 수행된 밀도범함수(DFT) 계산 결과와도 근접하였다. 그래핀의

광학적 물성의 정확한 측정은 opto-thermal 라만 분광법을 통한 그래핀 열전도도 측정, 유연한 디스플레이나 투명 전극 등의 설계에서의 광학적인 설계 등에 크게 도움이 될 것이다.

마지막으로, 타원편광 분광법을 통해 질소 도핑된 그래핀의 복소 굴절률 측정하였다. 본 연구에서 수행된 DFT 계산 결과 및 기존의 선행 연구 결과에 따르면 질소 도핑은 그래핀의 광학적 물성을 특정한 파장에 대해서만 변화시킬 수 있으므로 다양한 파장에서의 측정, 또는 궁극적으로 전 파장에 대한 측정을 통해서 순수 그래핀과 비교를 하는 것이 바람직하다. 본 연구에서 개발된 SPR과 ATR을 동시에 이용하는 방법은 단일 파장 측정에 최적화되어 있기 때문에 타원편광 분광법이 사용되었다. 측정 결과 질소 도핑된 그래핀은 순수 그래핀에 비해 굴절률의 실수부와 허수부가 줄어들었으며, 이는 도핑 과정에서 그래핀 층에 결점(defects)이 늘어나서 전하의 이동도가 줄어든 결과로 볼 수 있다. 향후 그래핀 합성, 전사 및 측정 기법을 더욱 개선하면 질소 도핑만의 효과를 관찰할 수 있을 것이다.

**주요어:** 그래핀, 층수 판별, 복소 굴절률(RI), 근접장 광학, 표면 플라즈몬 공명(SPR), 감쇠전반사(ATR)

**학번:** 2009-20727